Electrical Characterization of Polymeric Insulation by Electrically Stimulated Acoustic Wave Measurements

by

Joseph Barry, Bernstein

B.S., Electrical Engineering, Union College, Schenectady NY (1984)
S.M., Electrical Engineering, Massachusetts Institute of Technology (1986)
E.E., Electrical Engineering, Massachusetts Institute of Technology (1987)

Submitted in Partial Fulfillment

of the Requirements for the Degree of

Doctor of Philosophy

in

Electrical Engineering and Computer Science
at the
Massachusetts Institute of Technology
May, 1990
© Massachusetts Institute of Technology, 1990

Signature of Author _____
Department of Electrical Engineering and Computer Science
May, 1990

Certified by _____
Doctor Chatham M. Cooke
Thesis Co-Supervisor

Certified by _____
Professor Stephen D. Senturia
Thesis Co-Supervisor

Accepted by _____
Professor Arthur C. Smith
Chairman, Departmental Committee on Graduate Students

Electrical Characterization of Polymeric Insulation by Electrically Stimulated Acoustic Wave Measurements

by

Joseph Barry Bernstein

Submitted to the

Department of Electrical Engineering and Computer Science

on May 18, 1990 in partial fulfillment of the requirements

for the Degree of

Doctor of Philosophy.

Abstract

Widespread use of polymeric insulation has motivated interest in understanding the physics associated with the electrical aging process. Under DC bias, materials such as polyethylene (PE) and poly(methylmethacrylate) (PMMA) have been known to accumulate space charge. As charge builds up within the bulk, the electric field becomes modified with regions of higher and lower field. Detection of the accumulated resident space charge profiles resulting from electrical stress gives insight into breakdown and loss mechanisms of the material.

This thesis presents the Electrically Stimulated Acoustic Wave (ESAW) method of determining space charge profiles in polymeric insulation. The method is a non-destructive means of observing one-dimensional space charge accumulation, in-situ, during electrical excitation. ESAW was used to observe the effects of DC electric field in samples of PE and PMMA.

Polarization was observed at all temperatures measured between 20 and 90° C with fields applied from 1 to $4\frac{KV}{mm}$ in PMMA. Heterocharge extends deep into the bulk of $\frac{1}{2}$ cm thick samples. Negative charge injection appears to increase with temperature above 40° C. At a temperature as high as 90° C, cathode injection overwhelms the positive heterocharge producing a net negative charge within the sample, and continues until the surface field is substantially reduced, demonstrating a space charge limited condition.

PE exhibits cathode injection at every temperature measured between 20 and 60° C. At higher temperatures, the conduction appears to become space charge limited once the injected charge increases sufficiently. Evidence of bulk polarization in PE only appears at a temperature as low as 20° C

A virtual cathode condition was imposed on PMMA samples by shallow implantation with an electron beam. The charge was then imaged across the unirradiated side with a DC voltage. The voltage needed to cancel the surface image charge was determined using ESAW. This set of experiments allowed the testing of bulk properties of the plastic without influence from the electrodes. Using the virtual cathode data, in combination with experiments of other researchers, approximations have been made for the density of states, electron mobility, equilibrium trapped charge concentration, and the effective activation energy.

The conduction in PMMA is consistent with a *polaron* transport theory within the material and agrees with conductivity results from previous works of other authors. Contributions of this work include: the development of a method for detecting distributed space charge in polymeric insulation with a better resolution than any other available technique, the construction of a density of states model for PMMA, and a unique way to distinguish space-charge-limited from injection-limited currents in insulators.

Thesis Co-Supervisor: Dr. Chatham M. Cooke
Title: Lecturer in Electrical Engineering and Computer Science

Thesis Co-Supervisor: Professor Stephen D. Senturia
Title: Professor of Electrical Engineering and Computer Science

In Memory of
Professor David Adler
Mentor, Advisor, Friend

Acknowledgments

Completing a thesis document after all of the experimental work has been performed and compiled can be a never ending task. There is no formula or rigid course of action for taking a project, developing it, and reporting about it in a way that makes scientific sense. Were it not for the guidance and assistance of several people, to whom I owe a great deal of thanks, I can not imagine how I would have ever made it to the point of presenting this document.

I consider myself fortunate for having found Professor David Adler who was willing to guide me and share his world of amorphous Silicon and his truly phenomenal understanding of the non-crystalline world. I had the honor of working under his guidance for the final two years of his life, years which I shall never forget, since he left me with a drive to continue studying disordered materials. The significance of his writings has become more apparent to me as I tried to build a model to help explain results of this thesis. The more of his works I read, the more proud I felt to have been one of his students. It is for this reason that I dedicate this thesis to the memory of David Adler, who not only inspired me to complete my degree, but gave me a direction for future pursuits.

I also want to express my deepest gratitude to Chatham Cooke for accepting me on this project with essentially blind faith. He trusted me from our very first meeting, the way he does with so many people, to understand the problems and develop a means for their resolution. I admire this quality most in him, that he sees the best in people and respects their opinions. He respects every person for what he or she is and for the contributions of that person, no matter how small. Chat considers every insight to be inspired and helps to bring forth the creative powers to develop ideas into useful tools.

Equally important to my development in graduate school is Professor Stephen Senturia, who encouraged me to have faith that I would find a new project after Professor Adler passed away. He has always supported my ideas and gave me confidence to be creative on my own, while helping

me take care not be sloppy in my work. I became privileged the moment he agreed to co-supervise my thesis. I have not found anyone who knows Steve, or his work, who does not share my opinion of his outstanding ability to bring out the best in people and give them confidence to achieve their goals.

The other two committee members, David Epstein and James Melcher, have also been invaluable resources for helping me develop ideas and compose this document. I am thankful for their patience and encouragement. Professor Epstein helped me with his immediate understanding of the measurement technique and provided the insight needed to develop the apparatus which made this project possible. Professor Melcher has honored me with so much of his time to help me understand the fundamental principles in a coherent way so that they can be explained in this document.

I can not describe how honored I feel to have had the opportunity to spend this much of my life at this institution under the guidance of such outstanding individuals. I am thankful to the Holy one, blessed be he, who has provided me with opportunities over the past few years to work closely with these and other great people while providing close friends and associates, as well as ample recreational facilities with enough time to enjoy them. Specifically, I want to acknowledge the MIT Folk Dance Club for providing a means of expressing my passion for life through dance and for the opportunity of meeting Karen Rabin who now shares my life through marriage. I can not exclude the MIT Nautical Association for providing unforgettable hours of sailing on the Charles during those days when it was too nice outside to sit and work at my desk. I also wish to express my appreciation to Gee Rittenhouse and Lee Tavrow, my two loyal office mates, who really made it easy and fun to be at school. I will never forget the support and enlightenment they provided for me, along with many others I was blessed to be working with.

<div align="right">Joseph B. Bernstein</div>

Contents

List of Figures

10

11

12

13

14

Chapter 1

Introduction

Polymeric insulators are made of covalently bonded molecules with tightly constrained valence electrons. These materials are mostly amorphous and can not be easily described through the formalisms of crystalline physics [1]. Insulating materials conduct electricity so weakly that stored charge may persist within the bulk for days or even years. Since polymeric insulation is extensively used, understanding how and why they store charge is imperative to produce improved materials.

The electrical behavior of covalently bonded amorphous molecular solids are generally not well characterized because of the large number of parameters needed to describe the density of electronic states and the limited number of tests one can perform to observe them [2]. Imposing external stimuli such as light and electrical fields at different temperatures may generate detectable current densities across the material. The external current can give some indication of the microscopic processes involved when fit to certain models for their behavior. The dynamics of space charge build up within the bulk of an insulator can not be measured uniquely from purely external measurements. Without knowing the space charge distribution and

15

the current through an insulator, it can not be fully characterized for a given set of stimuli.

The most common geometry for measuring the conductivity of an insulator is a *pancake* structure. Circular metal electrodes are deposited on either side of a thin sample of insulation to create an essentially uniform electric field between the plates for an applied quasistatic voltage, keeping the dynamics one dimensional.

In the presence of space charge accumulation within the insulator, the electric field will not be uniform across the sample. The integral of the field between the electrodes is constrained by an applied constant DC excitation, so space charge within an insulator will impose regions of higher and lower field as compared to a uniform E-field in a space-charge-free sample with uniform dielectric permittivity.

A failure caused by an excessive localized E-field due to space charge accumulation can be irreversible and hazardous in certain high voltage situations; yet, there is no consistent way to predict how charges arrange themselves within an insulator before a breakdown occurs [3]. Determining the space charge distribution within an insulator while it is being stressed would allow one to observe the aging process before a breakdown occurs. This could help evaluate ways of preparing insulation which does not ultimately accumulate charge while still functioning as an insulator.

The goal of this project has been the quantitative electrical characterization of polymeric insulation by a non-destructive, in-situ, measurement of bulk charge distributions. The technique employed in this work is relatively new and is called the Electrically Stimulated Acoustic Wave (ESAW) method [15]. This method uses an ultrasonic detection system to measure

the one-dimensional charge distribution residing in a polymeric insulator. Details of the detection scheme are described in chapter 2.

Knowing the bulk space charge profile throughout the electrical excitation process can provide a better understanding of the physics involved with the microscopic charge transport. This work is primarily concerned with the electronic structure of poly(methylmethacrylate) (PMMA) and polyethylene (PE) as determined from poling samples with a constant voltage between room temperature and the glass transition temperature. The combination of ESAW poling data with tests including implanted electron charge, and the works of other authors, will provide an approximate model for the electronic structure.

In order to manufacture more durable insulators, an understanding of the charge dynamics under operating conditions is required. By observing the changes in localized charge concentrations caused by known external conditions, one may be able to model the conduction and breakdown mechanisms more appropriately [3]. The added insight of ESAW measurements will allow one to make better predictions of the charge accumulation processes affecting the material.

The following section will describe several in-situ experimental methods that have been shown to determine space charge profiles in polymers [7]. A comparison will be made between the different techniques by describing a figure of merit relating the sensitivity to charge measurement and the resolution capability for detecting spatial variations. An overview of the remainder of the document will follow that discussion.

1.1   Profiling Space Charge *(Background)*

Two destructive techniques involve invasive probing, one by physically altering the surface with electron beams [8], the other by diffusing chemical solvents [9] to liberate trapped charges. The probing depth is determined from the knowledge of the penetration depth, while excess current results from liberating charges within the sample. Detection of the current with penetration depth provides a profile of the resident space charge. These methods can not be repeated on the same sample, limiting their usefulness for measuring charge dynamics.

A class of thermal transient tests are also used to profile space charge distributions. These experiments may be performed repeatedly on the same sample; although, the trapped charge is liberated after an experiment has been performed. This class of probing techniques also can not be used to measure dynamics of space charge motion. These experiments include the Heat Pulse technique [10], and the modification called the Laser Intensity Modulation Method [5]. Both methods are presumed to distinguish polarization from fixed charge; however, their continuous dynamics can not be monitored.

Several non-destructive profiling techniques are useful for transient analysis because they may be be performed repeatedly on the same sample during a charging process. Space charge that accumulates at many repeated experiments performed over regular time intervals can be compared to one another, adding the time dimension by which one may monitor charge dynamics. The time dimension is critical for identifying the behavior of microscopic charge motion for the purpose of modeling conduction mechanisms.

Every profiling technique offers its own contribution to understanding

18

the behavior of charge motion in insulating materials. Some techniques are preferable to others depending on the thickness and composition of the samples being tested. Every probing method is limited by its ability to resolve charge layers within two limits: the sensitivity to charge density and the ability to resolve spatial variations. Both quantities should be minimized for any technique allowing the factor, R, defined here as the product of the smallest detectable charge density and the narrowest spatial resolution, to be a figure of merit appropriate to resolving a charge profile. The units of R are charge per unit area, so normalizing to $\frac{nC}{cm^2}$ allows one to compare measurement techniques to each other. This definition suggests that a smaller R represents a more sensitive technique with narrower resolution.

The figure of merit hides the applicability to sample thickness. For example, the pressure step technique is only applicable for samples thinner than a few microns, whereas the Kerr-effect technique requires a sample that is at least several centimeters long and no thinner than a few millimeters. Both of these methods will be presented, along with the other repeatable methods. Some of the fundamental limitations of each technique will also be discussed [7] in order to justify the ESAW method as an appropriate method for observing the space charge profiles in the tested polyethylene (PE) and PMMA samples.

1.1.1 Contact Electrification

One basic technique used to measure the net charge moment of an electret is to place a sample with one removable electrode in a vacuum and measure the variation of induced surface charge with electrode separation. This is schematically illustrated in Fig. 1.1 with the electrode separated from the sample by distance d_1. The fixed parameters d_2, ϵ_1 and ϵ_2, determine the

19
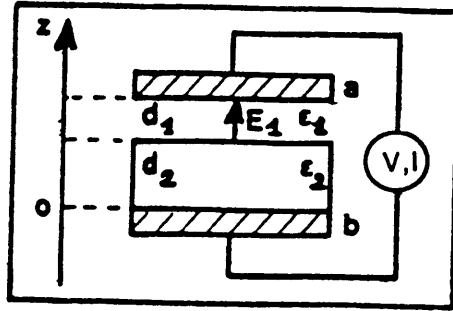
Figure 1.1: Static configuration of a charged insulator between two electrodes [7]

charge, σ_a, on the movable electrode with the electric field E_1 by

$$\sigma_a = -\epsilon_1 E_1$$

and varies with electrode displacement. When the electrode is very far away from the charged insulator ($d_1 \rightarrow \infty$), the electric field, and the surface charge on the upper electrode approaches zero. The induced current through the meter equals the change in charge with time as the electrode distance d_1 is changed.

This technique, and variations of it, allows one to measure the net charge and first moment by assuming that all the charge is concentrated in a single sheet [11]. No details of the space charge distribution can be obtained by this method; however, it is adequate for determining the induced sheet charge at or near the surface of a thin film [12].

The most important application of this method has been to determine the triboelectricity [4] caused by contacting a metal to a polymer. By contacting metals of different work functions to a polymer and detecting the net induced charge, many details of the density of electronic states distribution have been found [50]. By performing this same experiment on samples of different thicknesses, a penetration profile has also been inferred.

20

A figure of merit for this technique would have little meaning since no details of a bulk charge distribution are observable. This method has been successfully applied to samples of micron thickness to millimeters [11] and used to learn about the charging behavior of electrets.

1.1.2 Kerr Electro-Optic Effect

A second method, which can be performed only on transparent samples, uses the Kerr electro-optic effect to probe electric field concentrations in a non-linear electro-optic material [13]. A schematic of a typical system is illustrated in Fig. 1.2 for measuring the field distribution in a PMMA sample exposed to an electron beam radiation. The laser system measures the field between two plates by observing the electrically induced birefringence. An electro-optically non-linear property of many materials is the *Kerr* effect, which alters the material index of refraction to polarized light propagating in the direction of the internal field as compared to light propagating perpendicular to the field.

A monochromatic polarized laser propagates visible light through a material with a finite Kerr coefficient and electric field. The signal will emerge out the other end with a phase shifted polarization. The phase, ϕ, is related to the E-field by

$$\phi = 2\pi B L \times E^2$$

where L is the sample length through which the laser propagates and B is the Kerr constant ($B = 2 \times 10^{-15} \frac{m}{V^2}$ For PMMA) [13]. The resulting phase shift is monitored with two video cameras through perpendicular polarizers.

Intensity variations of the collimated light across the sample are measured by a microcomputer after being recorded on a standard video cassette.

The variations in grey scale are used to determine of the E-field at each point in the video display, giving a 2-dimensional E-field profile. The total polarization change of the laser through the sample is proportional to the length of the sample, perpendicular to the video monitor. A longer sample is more sensitive to variations in field and will provide a more detailed output [14].

The electrically induced birefringence of an amorphous material is independent of its physical orientation since there are no crystalline planes to consider. As long as the material under test is homogeneous and free of crystalline order, the Kerr effect only depends on the field perpendicular to the direction of laser propagation and the length of the sample. The Kerr constant is the first order approximation for the electro-optic non-linearity causing a field dependent refractive index. For many insulating materials, this parameter remains proportional to the square of the field intensity and is used routinely to monitor the E-field in liquids and transparent dielectrics [13, 14].

The spatial resolution of the field density is limited by the magnification and pixel density of the video screen. This system is, consequently, limited in its ability to resolve a space charge distribution by the accuracy of taking the spatial derivative of the *noisy* E-field data. Consequently, various smoothing techniques must be used to achieve a reasonable result. The best resolution using the Kerr effect for space charge measurements in PMMA is reported by Hikita et.al [16] who measured 920 $\frac{nC}{cm^2}$ with a signal to noise ratio $SNR \approx$ 25, resulting in a sensitivity-resolution product

$$R \approx 70\frac{nC}{cm^2}$$

allowing for a minimum detectable charge with $SNR = 2$. The figure of merit for detecting space charge is deceptively high since this method has the
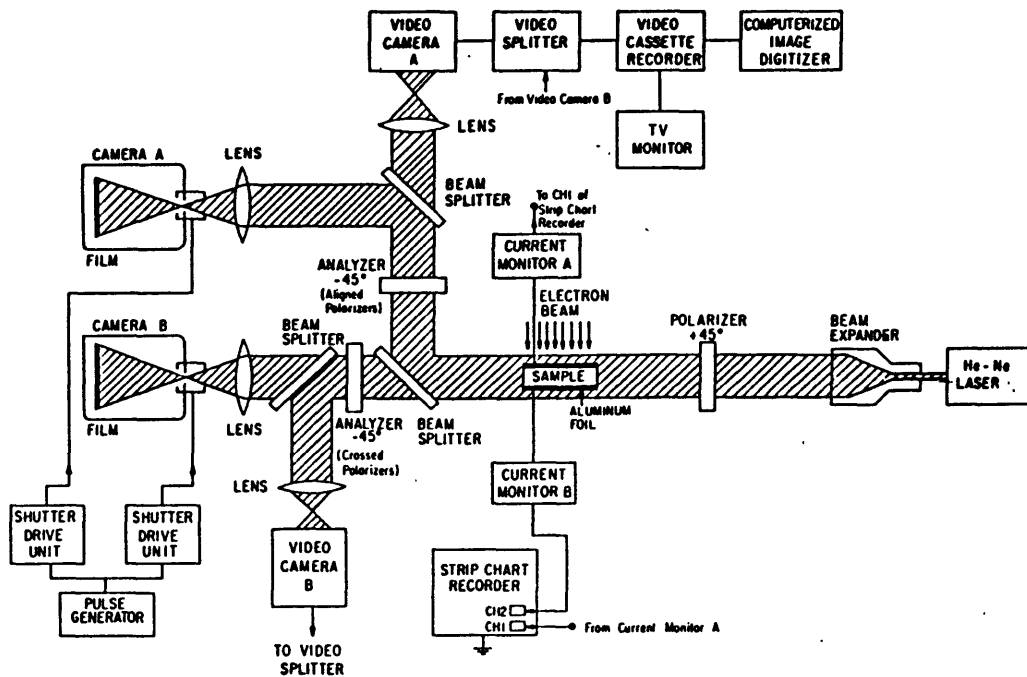
Figure 1.2: The measurement system of the electric field distribution using
Electro-Optic Kerr effect [16]

advantage of recording a 2-dimensional profile. This technique is sensitive to
field, not to charge, and this figure of merit is not appropriate for measuring
internal electric field concentration.

1.1.3 Pressure Wave Pulse

The earliest technique developed to profile space charge in one-dimension
is the Pressure Wave Pulse method [17]. A high intensity laser pulse is
aimed at a metal target which absorbs the energy. The quickly expanding
metal launches a short but intense pressure pulse into the dielectric. As
the pulse propagates through the sample, embedded charges are perturbed
by the strained material in the presence of the traveling pulse. If the local
molecular displacement from equilibrium is u, then the strain, $S(x)$ is defined

23
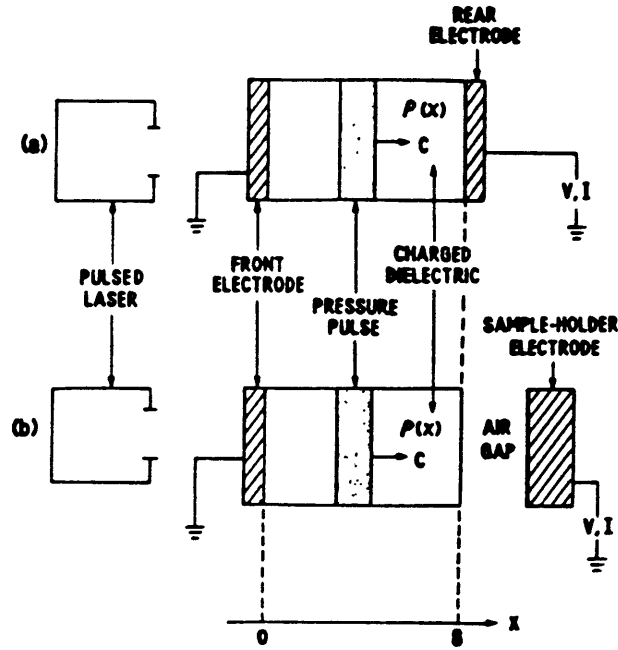
Figure 1.3: Schematic setup and geometry of the experiment for (a) two-sided-metalized and (b) one-sided-metalized samples where V,I represent current and voltage sensors [18].

as

$$S(x) = \frac{du}{dx}$$

If space charge is fixed to the molecular lattice, then the charged material will experience the same displacement when the wave approaches. The microscopic motion of fixed charges due to the strain pulse will cause a displacement current at the electrodes. This current can then be detected directly, or integrated to produce a voltage waveform which can be detected. The apparatus is shown schematically in Fig. 1.3. The pressure pulse propagates from the front electrode to the rear while the current or voltage is measured across the sample. The output is recorded with time as the pulse moves through the sample in either the open or short circuit configuration.

The open circuit voltage is proportional to product of the electric field

24

in the dielectric and the width of the pressure pulse τ_p as given by

$$V(t) = -(2 - \epsilon^{-1})\chi Pc\tau_p E(x) \qquad (1.1)$$

where χ is the compressibility of the material, P is the pulse pressure, c is the velocity of sound, and $x = ct$ is the position of the pulse within the sample [18]. Differentiation of the open circuit voltage waveform gives the short circuit current, producing a signal proportional to the bulk charge $\rho(x)$

$$I(t) = -(2 - \epsilon^{-1})\chi Pc^2\tau_p \frac{A}{s}\rho(x) \qquad (1.2)$$

where A and s are the sample area and thickness respectively. Gerhard-Multhaupt [19] presents a thorough analysis of this technique.

The use of narrower pulse widths have improved the resolution to $\approx 2\mu m$, and may become narrower in the future [20]. However, as can be seen in (1.1) and (1.2), a narrower pulse gives a smaller signal. Hence, the figure of merit remains the same at [20, 18]

$$R \approx 10\frac{nC}{cm^2}$$

Low Density polyethylene (LDPE) samples as thick as 2 mm were measured using this technique, where the same figure of merit has been achieved with wider resolution [22].

1.1.4 Pressure Wave Step

An alternate way to measure the electric field profile, similar to the *pulse* method, is by probing the short circuit current waveform with a Pressure Wave Step excitation. The acoustic propagation is identical to the previously discussed technique, except a sharply rising pressure step moves through the material. A step excitation produces an output proportional to the

integral of its corresponding pulse excitation. Integrating (1.2) with x gives an expression for the E-field within the material by applying the integral form of Gauss' Law

$$E(x) = \int_{-\infty}^{x} \frac{\rho(\xi)}{\epsilon} d\xi$$

resulting in an expression for the electric field $E(x)$ from the short circuit current waveform. This is the same expression as the open circuit voltage waveform with a pulse excitation (1.1), except τ_p represents the step risetime.

The acoustic transit time across a sample is equal to the velocity of sound times the thickness. An acoustically homogeneous material will propagate a planar wave packet from one end to the other in a time defined as the acoustic transit time. If two materials have different thicknesses and velocities of sound, but have the same transit time, they can be said to have the same *acoustic thickness*. This notation will be convenient when comparing the relative transit times of different materials in the same acoustic propagation path.

Pressure step excitation is accomplished with a transducer that is acoustically thicker than the sample being tested. The apparatus of Fig. 1.4 uses an X-cut quartz or a 36° Y-cut $LiNbO_3$ transducer, excited by a 100 ns long pulse whose risetime is < 300 *ps* [23]. The electric field across the transducer launches a uniform pressure wave toward the thin sample. As the resulting wavefront propagates through the dielectric under test, a high speed recording scope monitors the current, $I(t)$, waveform.

The thickest sample one can measure is limited to the generated pulse width divided by the velocity of sound in the dielectric under test. For a pulsewidth of 100 ns, and velocity of sound in PE approximately equal to

26
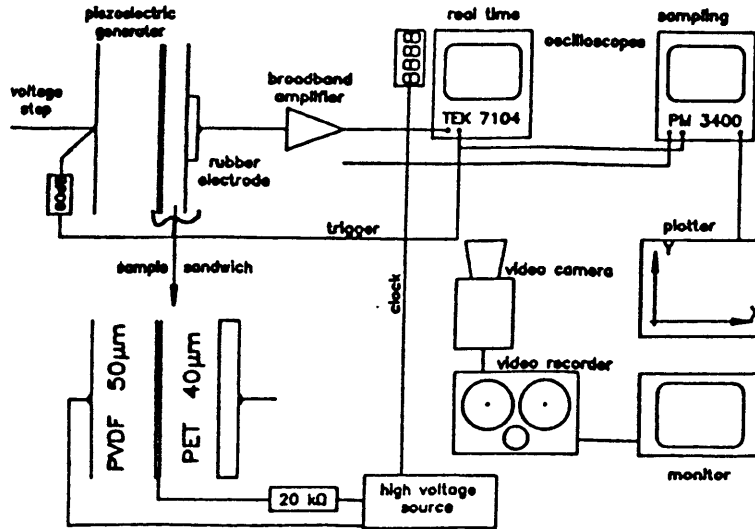
Figure 1.4: Schematic assembly of the Pressure Wave Step apparatus including the sampling scope [23].

$2\ \frac{\mu m}{ns}$, the thickest sample one can profile is 200 μm thick. The authors who first developed this technique [23] determined a sensitivity of

$$R = 20\frac{nC}{cm^2}$$

for sufficiently thin samples.

This technique is not as reliable as the Pressure Pulse technique for samples thicker than about 100 μm since it is difficult to get a true step for signals much longer than about 100 ns. The sensitivity is lower; however, the resolution for observing large charge densities in films thinner than $\approx$ 100 μm is superb.

1.2 Overview

The remainder of this document will present the work performed to develop the ESAW method of probing space charge in poly(methyl methacrylate) PMMA and polyethylene (PE). Chapter 2 is a discussion of the experimental setup and details of the charge probing system. ESAW is an acoustic technique based in principle on the dual of the pressure pulse technique. An electrical impulse excites trapped space charge to produce a pressure signal which then propagates through an electrode. The acoustic signal is then detected by a piezoelectric transducer after a delay. The received acoustic signal carries the space charge information which is processed to visualize the original charge profile.

The acoustic system will be described including computer simulations and calibration data to demonstrate the applicability of this method to samples as thick as nearly 1 cm. The figure of merit will be shown

$$R \approx 0.13 \frac{nC}{cm^2}$$

in the section describing the system calibration. Evidence for the linearity and range of reliable charge concentrations will also be mentioned.

Chapter 3 contains the plots of several profiles after having been exposed to various poling conditions, demonstrating the range of profile shapes that can result in PE and PMMA and how ESAW is able to detect them. Chapter 4 presents the time resolved distribution profiles of samples poled at temperatures below glass transition and fields between 4 and $40\frac{KV}{cm}$. A description of how an electron beam implanted charge layer was used to impose a space charge limited virtual cathode within the bulk of a PMMA sample is later discussed in chapter 4, followed by the experimental findings.

The results of chapter 4 will be shown to offer insight into bulk transport mechanisms in Chapter 5, where the data will be combined with other published works. The results of optical absorption, X-ray spectroscopy and triboelectrification experiments will be used to build a simplified band diagram for the electronic structure of PMMA. The band diagram will be shown to fit with published I-V data and the results of this investigation.

Chapter 2

ESAW Method

The technique developed for detecting space charge profiles in dielectric materials is the Electrically Stimulated Acoustic Wave (ESAW) method. Sheets of plastic insulator stock, on the order of a few millimeters thick, are electrically *poled* by applying a constant voltage at raised temperatures for hours or days, accumulating space charge within the material. The poled samples are periodically placed in the ESAW apparatus at room temperature to determine the effects of the field by observing the resulting space charge accumulation. Comparing the profiles of a particular sample at different times throughout the accumulation process allows one to gain insight to the charge dynamics which have taken place.

This study is concerned with one-dimensional *pancake* geometries. The charge accumulations, E-fields, and acoustic wave propagations will be considered constant in the $x - y$ plane, varying only in the z-dimension. A diagram of the apparatus is shown in Fig. 2.1, with a sample placed in the detection equipment.

The detection scheme is based on the Lorentz force law. An externally applied pulse field induces a perturbing force density on the material in the

presence of resident charge. A time dependent mechanical force density (F_0) results from the charge density, $\rho_q(z)$, at every point within the sample times the perturbing Laplacian field $E_z(t)$ results.

$$F_0(z,t) = \rho_q(z)E_z(t) \tag{2.1}$$

which becomes the driving force that propagates a stress wave $T_z(z,t)$ from every point across the sample ($0 < z < d$). The time dependence of the excitation field is a square pulse voltage V_p, applied across the sample thickness d

$$E_z(t) = \frac{V_p}{d}\Delta t\delta(t) \tag{2.2}$$

where $\Delta t\delta(t)$ is the short duration time dependent approximation for a pulse of width Δt. The relation (2.1) describes the time dependent fraction of the excessive force in the system which propagates as an acoustic wave that can be detected by a piezoelectric transducer on the other side of the lower electrode.

A distributed charge density, $\rho(z)$, within an insulator will be fixed for times much shorter than the dielectric relaxation time $\tau_r = \frac{\epsilon}{\sigma}$. As long as the perturbation is applied for a negligible time compared to τ_r, the applied field will not affect the charge distribution. A perturbing electrical pulse that is much shorter in duration than the acoustic transit time of the material

$$\Delta t \ll \frac{d}{v_s}$$

will produce a stress wave that closely resembles the charge distribution profile. The induced stress at every point across the sample propagates away without interference from neighboring charges, allowing the application of superposition principles for determining the one-dimensional charge distribution.

31

+ or -
0 - 20 KV DC

Upper electrode

Sample

Capacitor

Pulse Generator

.1 - 50 MHz
RF Amplifier

100 ns

0

V_{pulse}

Delay line /
Lower
electrode

30 db

-1500 V

BNC connector

Transducer

Absorber

Signal Output

Digital Recording
Scope

Desktop
Computer

Data
Storage
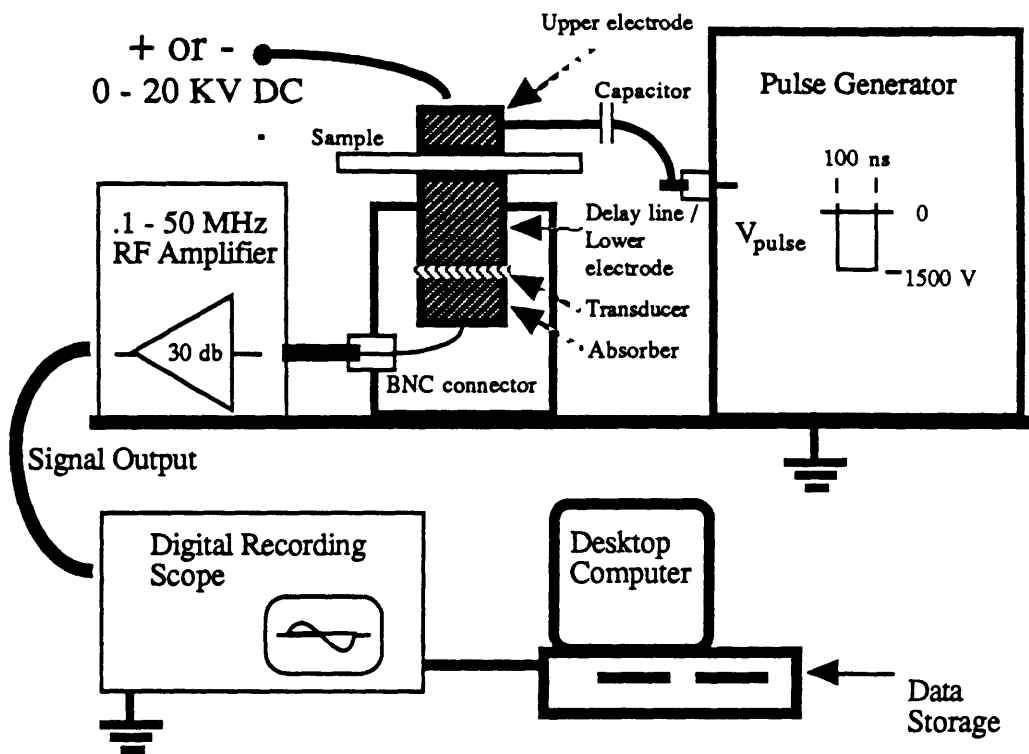
Figure 2.1: Diagram of the ESAW charge profiling system.

The stress signal produced by a charge density excited by a perturbation field $E_z(t)$ propagates at the velocity of sound v_s and the charge density returns to its equilibrium position once the field is removed. The resulting acoustic time signal is related to position by the velocity of sound within the sample

$$z_{rel}(t) = v_s t$$

where $z_{rel}(t)$ is the relative position in the sample with respect to the lower electrode boundary since signals are detected from the lower to the upper electrode. The delay time for a signal to propagate from the lower electrode boundary to the detector is τ_{delay} (see Fig. 2.2). This is the relative position due to the adjusted time, $t = t' - \tau_{delay}$, where t' represents the time after the pulse is applied. Thus, z_{rel} across the sample corresponds to the time between the electrodes $0 \leq z_{rel} \leq d$.

The dielectric permittivity, conductivity, and acoustic properties must also be uniform within the time frame of the applied electrical pulse to insure that the detected acoustic response faithfully reflects the embedded charge profile. Under these assumptions, (2.1) gives the total acoustic excitation from a distributed charge density perpendicular to the axis of excitation.

A sample under test is placed within the apparatus illustrated in Fig. 2.1 where it is sandwiched between two brass electrodes. Brass was chosen because it acoustically matches to the transducer material (see section 2.1) which detects the acoustic signals and it is a conductor. A conductor is needed to provide electrical contacts to both sides of the sample. The upper electrode is connected to the pulse generator and an external DC voltage source. The lower electrode has a dual purpose: to provide an electrical ground, and an acoustic delay. Acoustic stress waves generated within the

33

material propagate towards the electrodes and impinge at the boundaries. Signals which impinge at the lower electrode are transmitted to the transducer.

This method was first introduced by Takada et.al. [24] in 1985 as the Electro-Acoustic Pulse method. The principles of this detection scheme have remained nearly unchanged since its inception. The process of determining the charge profile from the recorded acoustic signal received by the transducer uses a simple signal processing algorithm as described in a publication by Maeno et.al. [25]. The detector response to a known sheet charge is taken as the impulse response $e(t)$ at time $t = 0$ after the acoustic coupling delay τ_{delay} as seen in Fig. 2.2. The signal arrives at the detector from the bottom electrode at $z = 0$, to the top at $z = d$, at the velocity of sound in the sample v_s.

The detector then integrates the impulse response for each arriving differential element of signal resulting from the charge distribution, generating a voltage signal $V_i(t)$ which is detected by the recording scope

$$V_i(t) = K \int_0^t \frac{V_p}{d} \rho_q(\frac{z}{v_s} - \tau_{delay})p(t)v_s dt \qquad (2.3)$$

where the pulse function, $p(t)$, is defined by the shape of the electrical excitation

$$e(t) = \frac{V_p}{d}p(t)$$

and the trace output corresponds in time to the charge distribution in space.

A double Fourier transform is performed on the output signal, maintaining both real and imaginary components so the spatial information contained in the phase terms are maintained. Using the principle

$$f(t - t_0) \iff F(\omega)e^{j\omega t_0}$$

34

the transform of the output signal can be used to recover the actual charge distribution once divided by the transform of the unshifted impulse response. The transform of (2.3) into frequency domain is

$$V_i(\omega) = \frac{KV_p v_s}{j\omega d}(1 - e^{-j\omega \Delta t})e^{j\omega \tau_{delay}} R_q\left(\frac{\omega}{v_s}\right) \qquad (2.4)$$

where $R_q(k_z)$ is the spatial transform of the charge distribution and is the only term that can vary from one sample to the next. All the terms remain constant for a particular material and thickness, along with the identity

$$\omega = v_s k_z$$

allowing a one-to-one mapping of the time domain signal into a spatial distribution.

This scheme is demonstrated in section 2.4 for the system presented here. Previous work used piezoelectric detectors having differential impulse responses, suggesting that high frequencies are detected at the expense of low frequency attenuation. The transducer output waveforms presented in the works of Maeno et.al [25] were studied in order to improve the detection scheme for measurements of wide space charge distributions.

Through understanding the nature of detecting the acoustic waves, it was determined that a differential impulse response is unacceptable since low frequency components corresponding to broad signals will be attenuated to below acceptable levels for profiling. This chapter will justify the system used to achieve a flat signal response in frequency range of interest and show that the developed system provides a means of detecting space charge distributions within polymeric insulation up to approximately 1 cm thick.

The acoustic detector is a thin layer of poled piezoelectric lead zirconium titanate (PZT), bonded to a brass coupling delay line (lower electrode). The

35

transducer converts acoustic stress waves into electrical signals by creating a voltage difference proportional to the stress across its thickness. The front of the transducer is electrically coupled to the lower electrode and the back of the transducer is connected to the absorber. The output of the transducer is taken between ground and the absorber, which is fed to the amplifier through a 50Ω coaxial shielded cable. The voltage generated across the transducer with respect to ground is amplified and detected by a digital recording scope.

The remainder of this chapter provides an examination of the ESAW method, detailing its advantages and its limitations. The analysis is based on a one-dimensional model in which all the acoustic excitations are longitudinal plane waves recorded in the time domain. The recorded signals is then decomposed into their Fourier components by a standard Fast Fourier Transform algorithm to reproduce the charge profile.

2.1 Propagation

In order to maintain a consistent set of electrical and elastic terms, the conventions used in the text by G. Kino [27] have been adopted. The stress, strain, and velocity of sound are represented by T, S, and v_s respectively; while $u, \dot{u},$ and $\ddot{u}$ are particle displacement, velocity, and acceleration. The force density in the material bulk is

$$\rho_{m0} \ddot{u} = \frac{\partial T_z}{\partial z} + F_0(z,t) \tag{2.5}$$

where ρ_{m0} is the specific mass density. The stress in a material is defined in linearized form in one-dimension

$$T_z = c_{33} \frac{\partial u}{\partial z} \tag{2.6}$$

36

where c_{33} is the bulk elastic modulus in the z-direction with z-directed excitation. which can be substituted back into (2.5) to yield the wave equation with a temporal and spatial excitation

$$\frac{\partial^2 u}{\partial t^2} = v_s^2 \frac{\partial^2 u}{\partial z^2} + \frac{F_0(z,t)}{\rho_{m0}} \qquad (2.7)$$

and the velocity of sound

$$v_s = \sqrt{\frac{c_{33}}{\rho_{m0}}}$$

which is the velocity at which stress and strain waves travel through the material.

The solutions of (2.7) are found for all time and space by knowing the stress at every point, z, at time $t = 0$. The boundary condition is found from (2.5) by integrating (2.1) at each point, z', with the unit delta function, $\delta(z - z')$, which gives

$$T_z^+(z') - T_z^-(z') = \int_{z'-}^{z'+} \left[\rho_{m0} \ddot{u} - \frac{V_p \Delta t}{\rho_{m0} d} \rho_q(z) \delta(t) \delta(z - z') \right] dz \qquad (2.8)$$

and is only finite at $z = z'$. The initial condition on the velocity is

$$\dot{u}(z, t = 0^-) = 0$$

The integral of (2.8) is over an infinitesimally small space, making the left hand term within the brackets go to zero (the second temporal derivative is finite across the region in space). As long as the *observer* at any point, z, is outside the region of excitation, the stress at any time is found from the initial condition, after propagation at the velocity of sound.

$$T_z(z,t) = T_z^-(z', t - \frac{z' - z}{v_s}) = \frac{1}{2} F_0(z', t - \frac{z' - z}{v_s}) dz' \qquad (2.9)$$

where z' indicates the position of the charge density, in reference to an observer at z. The factor of $\frac{1}{2}$ results from the assumption of homogeneous

37

material and that half the stress propagates in either direction from its point of origin.

The stress arriving at z is found by superposition of the contributions from every point excited by the driving function

$$F_0(z',t) = \rho_q(z')\Delta t \frac{V_p}{d}\delta(t)$$

This can than be integrated over all z' to find $T_z(z,t)$ for all space and time

$$T_z(z,t) = \int_{-\infty}^{\infty} \rho_q(z')\frac{V_p\Delta t}{2d}\delta(t - \frac{z'-z}{v_s})dz' \qquad (2.10)$$

which is only defined when the argument of δ is identically zero, giving the result

$$T_z(z,t) = v_s\frac{V_p\Delta t}{2d}\rho_q(z + v_s t) \qquad (2.11)$$

for a wave propagating in the $-z$ direction, with $z < 0$.

The initially generated stress will be defined here as

$$T_i(z)_{t=0} = v_s\frac{V_p\Delta t}{d}\rho_q(z)$$

for the propagation of a signal from its initial position within the sample, as illustrated in Fig. 2.2. The signal which propagates towards the lower electrode is

$$T_z(z,t) = \frac{T_i(z + v_s t)}{2}$$

impinging at the sample-electrode interface and transmitted toward the detector. The interaction of the acoustic signal with the interface and the transmission coefficient will be addressed next.

2.1.1 Interfaces

The interface between the insulating polymer and the lower electrode is composed of evaporated aluminum, less than $0.5\mu m$ thick, contacted by
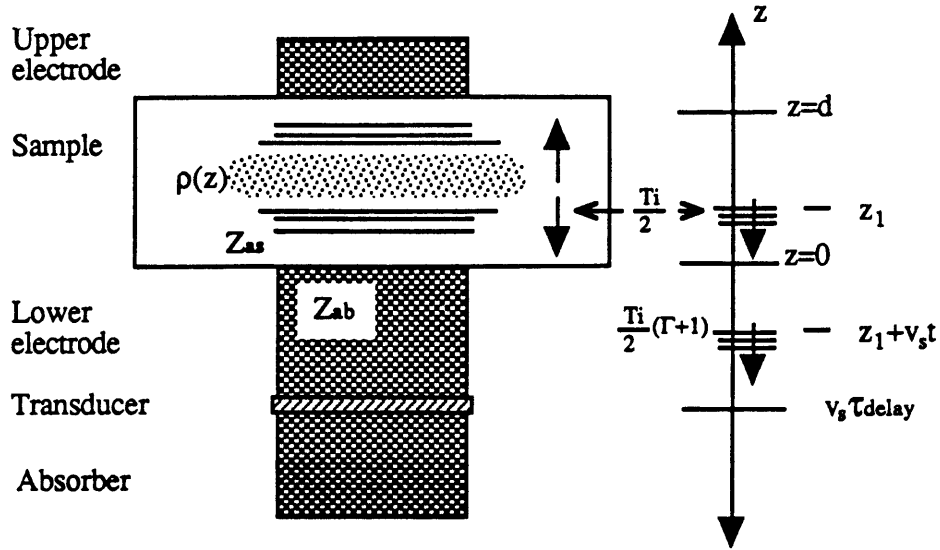
Figure 2.2: Simplified acoustic model of a charge layer of density $\rho_q(z)$ under the influence of an E-field $E_z(t)$, causing a stress $T_i(z,t)$ to propagate outward through the electrodes.

a layer of silicone oil between 10 and 50 μm thick. The oil provides an acoustic coupling between the sample and the delay line. The velocity of sound in oil is approximately 1.4 $\frac{\mu m}{ns}$ [35], consequently, a 100 ns pulse would propagate $140\mu m$. Since this is around the resolution limit of the detection system (see section 2.7) and no interference is seen from the interface, the oil layer thickness is assumed to be much narrower than the smallest detectable feature width. Hence, the polymer under test is effectively in direct acoustic contact with the delay line for the chosen pulse width.

The specific acoustic impedance Z_a is the property that determines the degree of matching from one material to the next. It is defined [27] as

$$Z_a = \rho_{m0} v_s$$

and depends only on the inherent material properties. The interaction of a stress wave signal with a material boundary results in transmission across the interface and reflection back into the material. The ratios of the resulting stress to the incident stress are the transmission and reflection coefficients.
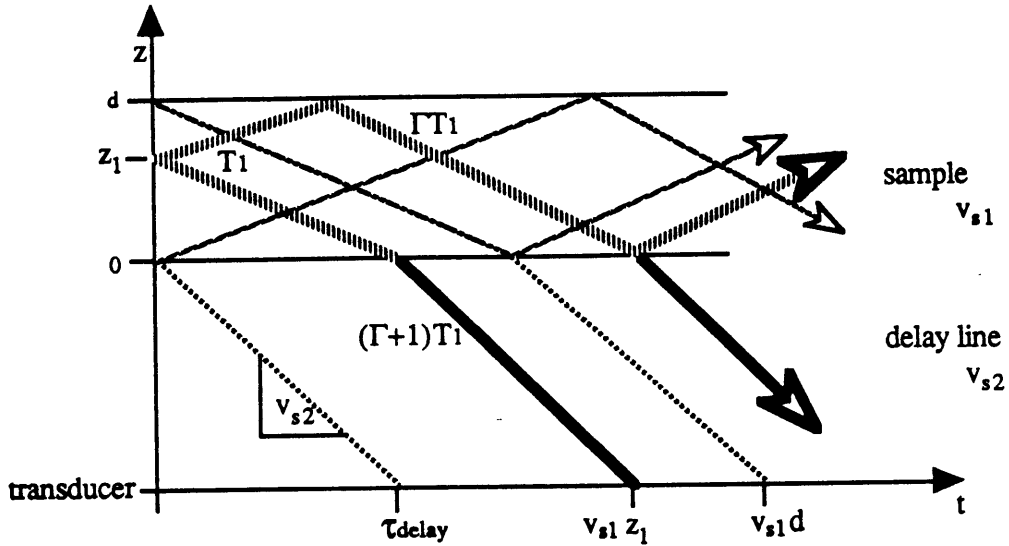
Figure 2.3: Plot of position vs time for an impulsive stress T_i originating at z_1, propagating at v_{s1} in the sample, and v_{s2} in the brass delay line.

The reflection coefficient for a signal propagating from material 1 toward material 2, Γ_{12}, is determined by the ratio of reflected stress in material 1 T_{r1} to incident stress T_{i1} at the interface

$$\Gamma_{12} = \frac{T_{r1}}{T_{i1}} = \frac{Z_{a2} - Z_{a1}}{Z_{a2} + Z_{a1}} \tag{2.12}$$

The ratio of the signal which propagates through the interface into material 2 to the incident stress in material 1 is the transmission coefficient. This can be found from conservation of stress in elastic media

$$T_{i1} = T_{t2} + T_{r1}$$

and the fraction of the signal which propagates through the interface into material 2, is the transmission coefficient

$$\frac{T_{t2}}{T_{i1}} = 1 + \Gamma_{12} = \frac{2Z_{a2}}{Z_{a1} + Z_{a2}}$$

40

which is positive for all values of Z_{a1} and Z_{a2}. What is interesting from this relation is that zero transmission results from a negative unity reflection coefficient and the transmitted stress is double the incident stress with positive unity reflection. Whereas this may seem counterintuitive, the acoustic power is proportional to $\frac{T^2}{Z}$, so the transmitted power through an interface is always less than the incident power

$$\frac{P_{T_t}}{P_{T_0}} = 1 - |\Gamma|^2$$

where P_T is the power contained in the stress wave and the subscripts t and 0 represent transmitted and incident portions respectively [27].

A detector that is perfectly matched to the delay line will generate no reflections at that interface; thus, all of the signal in the delay line contributes to the voltage output. Using a method described by Haus and Melcher [34] to visualize the signal propagation, a two dimensional z-t plot of the propagation of a stress wave is illustrated in Fig. 2.3. In this figure, one can see how a time domain signal contains spatial information originating between the electrodes.

For a charge induced stress created at time t, the signal received by the transducer after τ_{delay} exhibits acoustic features originating from within the sample being tested at z_1. The slope of lines in each region $\frac{dx}{dt}$ is the velocity of sound in that material. Once a signal reaches a boundary of different Z_a, it is reduced by the reflection coefficient Γ. This diagram does not illustrate the relative signal strength, but the relation of spatial variation and time resolved signal reception is clearly demonstrated.

By following the line of constant z at the detector, one can visualize the arrival of an excitation originating from the lower surface at $z = 0$ after the time τ_{delay} and from the upper surface at $z = d$ after an additional

41

$\frac{d}{v_s}$. The incident stress is reflected at the interface with a coefficient Γ and transmitted with $(1 + \Gamma)$. The transmitted signal propagates with a higher velocity of sound than in the polymer, so the slope in the lower portion of Fig. 2.3 is larger than in the sample. The characteristics of the signal originating within the sample are preserved as it propagates through the delay line as long as three-dimensional effects of normal diffraction are avoided. The next section discusses the limits within which the acoustic pulses propagating through a delay line can be considered one dimensional and the spatial variations of the received signal will be reliable.

2.1.2 Acoustic Diffraction

The delay line geometry is cylindrical with radius R and length L. Planar excitations occur at one end $(z = 0)$ as shown in Fig 2.4a. A complete modal analysis of the acoustic system should be performed to understand the actual dynamics of a signal propagating through the acoustic delay toward the detector. Such an analysis would be beyond what is needed to be sure that an initially planar wave remains planar as it propagates and is finally detected by the transducer. A worst case condition will, thus, be considered to provide approximate limits on the geometry of the delay line.

If excitation occurs at the boundary to a semi-infinite half space a planar wave will undergo Fresnel diffraction [27], adding curvature to the signal as it moves through the material as illustrated in Fig 2.4b. The signal at each point propagates outward, maintaining its shape at first, but spreading out as it travels. The rate at which curvature is added depends on the wavelength of each frequency component. Wavelengths much smaller than the radius remain planar to a greater distance than larger wavelengths.

The outer boundary is open to air, making it nearly perfectly reflecting
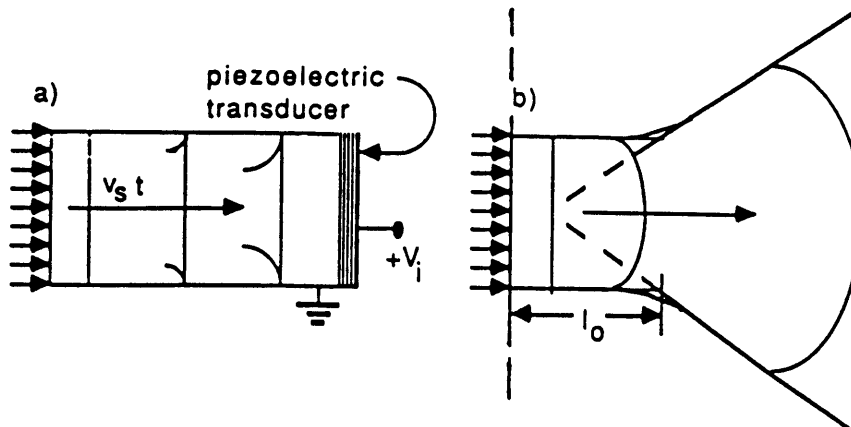
Figure 2.4: a) Cylindrical delay line with acoustic signal entering the front and detected by the piezoelectric transducer at the back. b) Propagation of an initially planar wave through a homogeneous semi-infinite half-space.

with $\Gamma \approx -1$ ($Z_{a2} \ll Z_{a1}$), causing signals to remain within the delay line by being reflected back in as seen in Fig. 2.4a for a propagating impulsive sheet wave. The cylinder may tend to guide the wave, keeping the pulse planar throughout the propagation. For a worst case, one can consider a delay line length which consideres the tendancy for a signal to spread in a semi-infinite media, allowing for acoustic diffraction.

Diffraction would cause signal spreading resulting in stress tails following the initial signal. Upon first arrival at the transducer, reflections of the spreading signal interfere with the reception of further acoustic signals. This is three dimensional effect must be avoided in ESAW experiments to detect details of the actual acoustic signal. A geometry which keeps signals planar while they propagate through the delay line is required for this technique to give reliable output.

An ultrasonic acoustic pulse is analogous to an electromagnetic pulse and can be treated with the formalisms of optics. The Huygen-Fresnel principle[1]

---

[1]For a complete analysis of this principle, see *Principles of Optics*, M.Born and E.

43

applies to the propagation of planar sound waves as well as optic waves and allows one to find a length threshold for which a wave in the Fresnel region remains nearly planar. This length $l_0(\lambda)$ is the distance at which a plane wave of wavelength λ begins to exhibit curvature in a semi-infinite half space, shown schematically in Fig 2.4b [28]

$$l_0(\lambda) = \frac{2\pi R^2}{\lambda} \tag{2.13}$$

Choosing the delay line length such that $L = \frac{1}{2}l_0(\lambda)$, the longest tolerable wavelength

$$\lambda_{max} = \frac{\pi R^2}{L}$$

above which, signals can not be considered planar and details of the signal may be obscured by surface reflections converting longitudinal mode waves into shear mode waves.

To translate the maximum acoustic wavelength to the largest time span,

$$\tau_{max} = \frac{\lambda_{max}}{2v_s} = \frac{\pi R^2}{2Lv_s} = \frac{\pi R^2}{2L^2}\tau_{delay} \tag{2.14}$$

for

$$\tau_{delay} = \frac{L}{v_s}$$

where v_s is the longitudinal velocity of sound in the direction of propagation in the delay line. Materials with a high velocity of sound require a larger ratio of area to length to maintain a one dimensional analysis.

A typical brass delay line used in recent experiments has a velocity of sound .35 $\frac{cm}{\mu s}$, and radius and a length of 1.5 cm, giving a 4.3 μs delay and $\tau_{max} = 6.7\mu s$. Signals longer than τ_{max} may be distorted. Therefore, as long as the received signals of interest are shorter than $\approx$ 6μs, they can be

---

Wolf, chapter 8; Pergamon press, sixth edition 1980.

considered planar and a one-dimensional model is sufficient to describe the behavior.

Mode conversion is the major difficulty with signals propagating at an oblique incidence to side walls [29]. Accounting for surface effects would greatly complicate the model while not necessarily adding insight into the propagation dynamics. Hence, the delay line geometry must be designed to maintain acoustic pulses well within the Fresnel limit of planar longitudinal propagation.

2.1.3 Acoustic Attenuation

Acoustic loss due to internal friction in the material can be modeled as proportional to the velocity $\dot{u}$ in the wave equation (2.7).

$$\frac{\partial^2 u}{\partial t^2} = v_s^2 \frac{\partial^2 u}{\partial z^2} + \frac{F_0(z,t)}{\rho_{m0}} - \frac{\alpha}{\rho_{m0}} \dot{u}$$

Both sides can be differentiated with respect to z and combined with (2.6) to yield the *stress* wave equation without the driving term (F_0) for a propagating wave

$$\frac{\partial^2 T}{\partial z^2} = v_s^2 \frac{\partial^2 T}{\partial t^2} - \alpha \frac{\partial T}{\partial t} \tag{2.15}$$

where the time dependent attenuation term is a first order perturbation on the free-space solution. The result has an exponential loss term, which is proportional to the frequency squared [27]. The solution to (2.15) for a freely propagating stress signal in a lossy material.

$$T_z(z,t) = \int_0^\infty A(k_z) e^{jk_z(z \pm v_s t)} e^{-(v_s t)\alpha(v_s k_z)^2} dk_z$$

where $A_0(k_z)$ is the Fourier transform of the signal at $t = 0^+$, with k_z representing the spatial frequency components with units of mm^{-1}. The

form of this integral is actually the convolution of a Gaussian in space with the waveform $A_0(z)$.

If the initial signal is an ideal impulse in space, the transform $A_0(k_z)$ is unity for all frequencies. Solving for $T_z(z,t)$ in this instance gives a Gaussian whose width in space increases with time

$$T_{zi}(t) = K e^{-(\frac{v_s t}{2W})^2}$$

where T_{zi} is the time shifted Gaussian wave packet with width W. If the units of time are seconds and the units of distance are mm, the units of the loss parameter α are $\frac{sec^2}{mm}$ [27]. It can be seen that the width of this Gaussian depends on the time of propagation t, assuming the impulse was formed at $t = 0$

$$W = (2\alpha t v_s^3)^{-\frac{1}{2}}$$

where W is the characteristic width of the Gaussian waveform caused by an impulsive excitation.

A more accurate representation of the initial signal produced by the electrical excitation of a sheet charge used in ESAW experiments would be a square wave whose width is $W_0 = v_s \Delta t$. An originally square waveform convolved with a Gaussian gives a signal whose width, W, is determined by the transcendental function

$$\left(\frac{W_0}{X}\right) \left[ln(1 + \left(\frac{W_0}{X}\right)) - ln(1 - \left(\frac{W_0}{X}\right)) \right] = 2\left(\frac{W_0}{W}\right)^2 \qquad (2.16)$$

where X is the resultant characteristic width and W_0 is the width of the square pulse. The solution is plotted in Fig. 2.5. For the limit $W_0 \gg W$, the loss is negligible, and $X \approx W_0$. Similarly, for $W_0 \ll W$ then $X \approx W$, as expected.
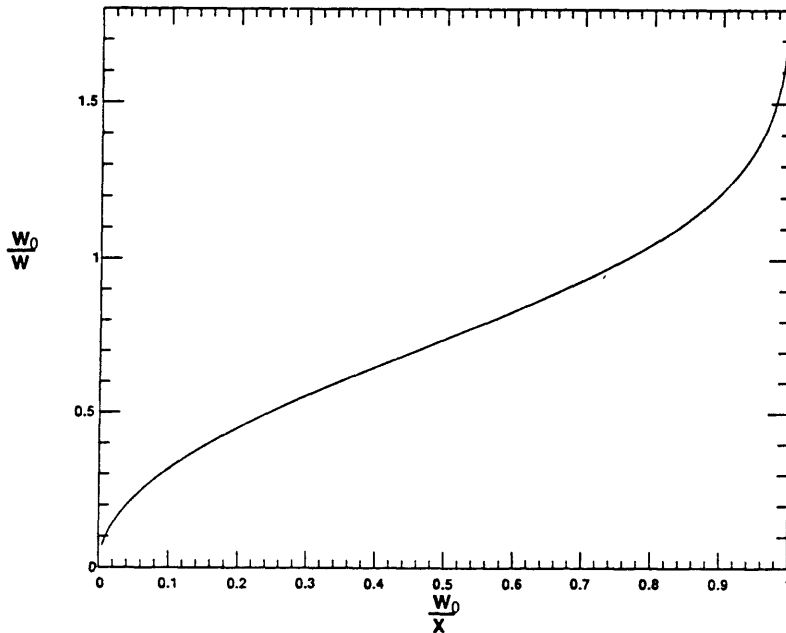
Figure 2.5: $\frac{W_0}{W}$ vs $\frac{W_0}{X}$ between 0 and 1.

An initially square pulse becomes more and more Gaussian-like as it propagates away from its point of origin. Fig. 2.6 illustrates the simulation of a pulse with initial width .1 mm, and height 1, in a linear material with frequency dependent loss. This simulation is in the x-dimension where $x = 0$ and $x = 1$ are perfectly reflecting boundaries sending an impinging signal back into the region with opposite sign. The example shows the stress wave within the material at four different times; 0, 250, 500, and 1000 ns, where the attenuation constant is $\alpha = 0.001$ and velocity of sound $v_s = .5\frac{mm}{\mu s}$.

The simulation illustrates the two waves with $\frac{1}{2}$ the original signal propagating in each direction, so the peaks are each 0.5, summing to 1. The walls are perfectly reflecting with $\Gamma = -1$, so the negative signal seen after 1000 ns is inverted from the positive signal which has not reached the far wall at 1 mm. This simulation does not propagate a negative signal in one

47

time = 0ns
time = 250ns
time = 500ns
time = 1000ns

1

0.5

0

S(x) atten = .001, vs = .5 mm/microsec

0   0.1   0.2   0.3   0.4   0.5   0.6   0.7   0.8   0.9   1
x (mm)
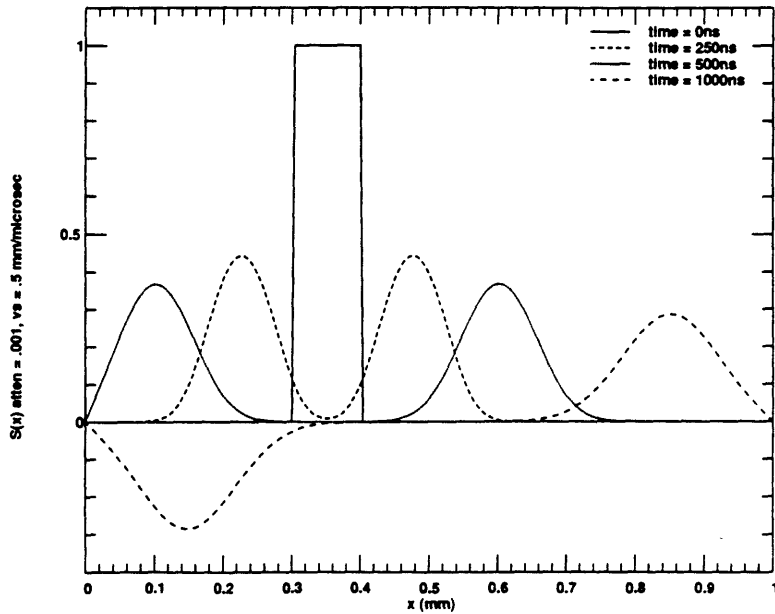
Figure 2.6: Propagation of a square stress pulse in a linear lossy material

direction for the purpose of visualizing the boundary. In actuality, one direction would contain a *tensile* wave, while the other would be *compressive*.

The voltage output from the transducer depends on the acoustic signal it receives from the delay line. The transducer is sensitive to the sign of the generated signal packet and can be calibrated accordingly. The presence of attenuation limits the propagation of high frequency components, placing an absolute limit on the minimum achievable spatial resolution. The next section details how the piezoelectric transducer detects a pressure signal by generating a voltage output that is amplified and received by the recording apparatus. It will be shown that the response of the transducer puts a greater restriction on the bandwidth achieved in the ESAW system in this work.

48

2.2 Transducer

The piezoelectric acoustic transducer used in the ESAW system converts stress waves into electrical signals by producing a voltage across the stress sensitive media. Signals produced by the transducer are amplified and sent to a recording oscilloscope which stores the signal waveform with respect to time. Acoustic information enters the crystal from the *front* and either exits the *back* into an absorbing material or is reflected back into the transducer. For the remainder of this discussion, front and back will refer to the crystal surfaces while top and bottom refer to the sample. Also, the term *crystal* will be used interchangeably with transducer.

For the purpose of understanding how to design an optimal transducer for ESAW measurements, a simplified analysis of longitudinal mode, linear, time invariant acoustic detection will be presented. A systems approach will provide a method for visualizing the detection of first arrival pulses by knowing the frequency response of the crystal through Fourier decomposition of the response to an impulsive stress.

One can transform a single waveshape into its Fourier components by assuming periodicity with a fundamental frequency f_0. A single time domain signal may be represented as a linear superposition of steady state modes whose frequencies are integer multiples of the fundamental.

$$f_n = n f_0 = n \left(\frac{1}{2 v_s d} \right)$$

where d is the acoustic thickness of the material, and f_0^{-1} is the round-trip time of a signal in that material.

Time domain system noise is the background signal from the piezoelectric detector, amplifier and oscilloscope. By comparing a signal with the

49

RMS noise, one can determine the signal to noise ratio. Components below the noise threshold will be lost, limiting the sensitivity to small and high frequency signals. The minimum signal times the narrowest resolution is determined by the noise from the transducer-amplifier-detector combination and the signal strength from a true sheet charge. The signal processing scheme to recover the calibrated charge profile should filter unwanted components since high frequency will be amplified along with the signal. The high frequency cutoff of an impulsive signal determines the resolution width resulting in the figure of merit described in section 1.1.

2.2.1 Constitutive relations

Consider the relation for dielectric displacement D with a permittivity ϵ, and local piezoelectric polarization P_p

$$D = \epsilon E + P_p \tag{2.17}$$

In a piezoelectric material, the internal polarization is proportional to the stress

$$P_p(z) = \epsilon g_{33} T_z(z)$$

where g_{33} is the z-directed field constant for z-directed stress [27]. If the crystal is assumed homogeneous and charge neutral, Gauss' law states

$$\nabla \cdot D = 0$$

resulting in

$$E_z(z) = -\frac{1}{\epsilon} P_p(z) = -g_{33} T_z(z) + const \tag{2.18}$$

where the constant must satisfy the surface boundary conditions.

50

The local z-directed electric field $E_z(z)$ is proportional to the stress at position z in the bulk of the piezoelectric material. Hence, the open circuit voltage across the transducer at a given time is

$$V_i(t) = -\int E(z,t)dz = g_{33}\int_{z=0}^{L_t} T_z(z,t)dz \qquad (2.19)$$

for the transducer thickness

$$L_t = v_{st}\tau_a$$

with v_{st} and τ_a as the velocity of sound and transit time across the transducer.

Under short circuit conditions, the voltage at both boundaries are equal so $V_i(t) = 0$. The transducer current i_t is found by the change in charge at the surfaces

$$i_t(t) = \frac{dQ_s}{dt} = C_0 g_{33}\int_{z=0}^{L_t} \frac{d}{dt}T_z(z,t)dz$$

where C_0 is the effective capacitance of the transducer. One can therefore model the crystal as a voltage source with an inherent capacitance due to its geometry and permittivity ϵ where

$$C_0 = \frac{\epsilon A_t}{L_t}$$

for a transducer area A_t.

The transducer capacitance is connected to the detector, having electrical impedance Z_{e0}, dominated by the resistive input impedance of the amplifier

$$Z_{e0} \approx R_0$$

A first order Thevenin equivalent model of the electrical output network for the piezoelectric voltage source in series with a single capacitor and resistor shown in Fig. 2.7. This first order high pass filter with electrical time

51

delay line | **transducer** | **absorber**

$T(z,t)$

$V_s\,t$

0 L z

$\dfrac{(V_s\tau_a)}{2}$

$$V_i(t) = \int_0^L T(z,t)\,dz \implies$$

C_0

$+$ V_i R_0 $+$ V_o
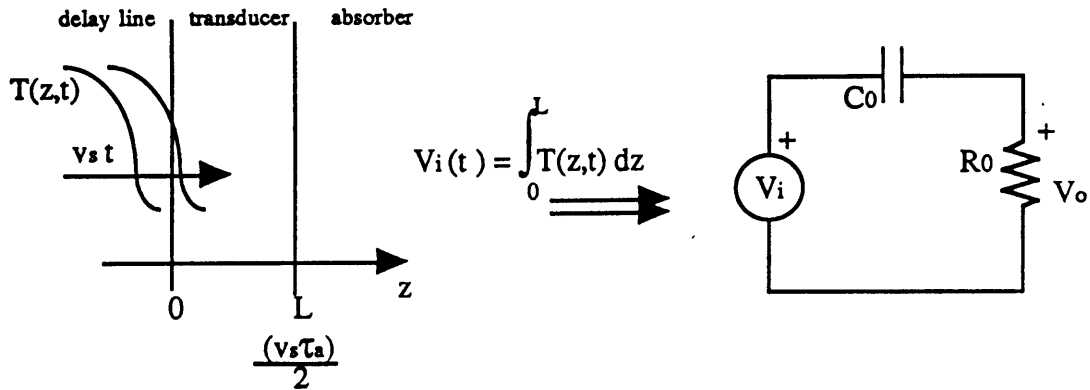
Figure 2.7: RC circuit used for detecting the output voltage signal $V_o(t)$ from the open circuit transducer excitation $V_i(t)$.

constant $\tau_e = R_0 C_0$, and output voltage V_o across the resistor represents the transducer response to a stress signal input.

The voltage signal detected by the amplifier and recorded by the scope is found by solving for $V_o(t)$

$$V_o(t) = \tau_e \frac{d}{dt}\left(V_i(t) - V_o(t)\right) \tag{2.20}$$

an expression that is easily transformed into frequency domain for steady state excitation. Once the solution is found for all conditions of τ_e and $V_i(\omega)$, the time domain impulse response is recovered by taking the inverse Fourier transform. Hence, the detector must be linear for a meaningful transform.

2.2.2   Signal Response

Acoustic signal reception is affected by two time constants and by possible reflections from the boundaries of the crystal. The acoustic time constant τ_a is the single trip time for an acoustic signal to move across the transducer. The electrical time constant τ_e is the RC product of the crystal in series with the amplifier. Consequently, two situations exist: one for $\tau_a \gg \tau_e$ and

52

the other for $\tau_a \ll \tau_e$.

Independent of the electrical configuration, three acoustic situations exist: a system where the transducer is acoustically matched on both faces, a system where the front is matched and the back is open, and one where neither side is matched. This third case results when the delay line and transducer materials are selected without regard to acoustic impedance.

Ray acoustics (high frequency approximations) will be assumed for the simplicity in understanding wave fronts propagating in straight lines with no diffraction, dispersion, or loss. This assumption was justified in section 2.1 for the materials and dimensions used.

Assume further that the glue bonds between the metal and PZT crystal are negligably thin so each material interface is characterized by a single Γ value. The bond thickness was measured on a caliper to be less than 10 μm, thinner than the resolution of the instrument and thin enough to be ignored. Two interfaces are present at the detector, one at the transducer front and one at the back, two reflection coefficients therefore characterize the boundary effects. The front reflection coefficient will be referred to as Γ_a and is the amount returning into the delay line as the stress wave enters the crystal while Γ_b is the amount reflected back into the crystal at the back interface.

A quasistatic approach to understanding transducer operation is appropriate for broad-band crystals (low Q), operated far from resonance, receiving purely planar waves. At or near the resonant frequency of a bulk wave transducer, the response may be influenced by second order effects which will not be discussed here. The following analysis assumes that signal frequency

53

components ω are not near τ_a^{-1}

$$\omega \ll \tau_a^{-1} \text{ or } \omega \gg \tau_a^{-1}$$

The response of the RC high-pass filter is the Fourier transform of (2.20), resulting in the transfer function

$$\frac{V_o(\omega)}{V_i(\omega)} = \frac{j\omega\tau_e}{1 + j\omega\tau_e}$$

where $\tau_e = \rho\epsilon$. This transfer function appears independent of the acoustic transit time τ_a. In reality, however, the thickness of the transducer is inversely proportional to the capacitance. Therefore, the two time constants depend on the material used, device area and amplifier input impedance, but will be treated independently for this analysis.

The transducer produces a frequency-dependent open-circuit voltage by integrating stress across its thickness (2.19) which is then detected through the RC high-pass filter (2.20). The time-domain output is the convolution of these two functions, which is the inverse Fourier transform of the product in frequency space. The received voltage signal V_o depends on the frequency characteristics of the acoustic signal and the mechanical termination at both ends. The following are the three general cases of transducer output functions based on their acoustic termination.

Matched transducer

A perfectly matched system is one with equal acoustic impedances on either side of the transducer so it does not reflect any signal at either boundary.

$$\Gamma_a = \Gamma_b = 0$$

The frequency domain representation of the output voltage for an arriving stress signal is found through the Fourier transform of (2.19) in the sinusoidal steady state, which gives

$$\frac{V_i(\omega)}{T(\omega)} = 2\frac{g_{33}v_s}{j\omega} sin\left(\frac{\omega\tau_a}{2}\right) e^{\frac{-j\omega\tau_a}{2}} \tag{2.21}$$

where the exponential term results from the time delay across the transducer. This transfer function is periodic in frequency, which is only intuitively helpful under certain limiting cases. Looking at the small frequency limit $\omega\tau_a \ll 1$, the sine function may be approximated by its argument. Hence, the magnitude of (2.21) reduces to

$$\left.\left|\frac{V_i}{T}\right|\right|_{\omega\tau_a\to 0} = g_{33}v_s\tau_a$$

When the acoustic transfer function is combined with the electrical response, the output for a steady state signal whose frequency is much lower than τ_a

$$A(\omega) = \left|\frac{V_o(\omega)}{T(\omega)}\right| = g_{33}v_s\tau_a\frac{\omega\tau_e}{\sqrt{1+(\omega\tau_e)^2}} \tag{2.22}$$

and is independent of τ_a. This states that the voltage output is independent of frequency as long as $\tau_e^{-1} \ll \omega \ll \tau_a^{-1}$.

To understand the system response at frequencies greater than the inverse acoustic time constant, one can look at the time domain response function (2.19) once again. An acoustic waveform propagating through the transducer at an instant of time may be decomposed into a superposition of normal acoustic modes with zero stress boundary conditions

$$T(t) = \sum_{n=0}^{\infty} C_n sin\left(\frac{n\pi}{\tau_a}t\right)$$

for the components C_n that solve $T(t)$ at a fixed point in space. We are only interested in the region between 0 and τ_a since that is the portion of

the signal integrated in (2.19) giving a voltage output. Consequently, the frequency domain representation is a series of impulses

$$T(\omega) = \sum_{n=1}^{\infty} C_n \delta \left(\omega - \frac{n\pi}{\tau_a} \right)$$

at integer multiples of the fundamental frequency.

Finding the frequency domain response of the open circuit crystal voltage V_i for a stress signal $T(\omega)$, requires finding the response from (2.21) at each frequency $k_n = \frac{n\pi}{\tau_a}$. This results in the expression

$$V_i(\omega) = \sum_{n=1}^{\infty} \frac{g_{33} v_s C_n}{j k_n} 2 \sin \left(\frac{n\pi}{2} \right) e^{-j\frac{n\pi}{2}}$$

having values of $(0, \pm 1)$ for the sine function. Therefore, the magnitude of the open circuit voltage is inversely proportional to the frequency. Going back to the output function for a specific input stress wave in frequency space, the result for $\omega \gg \tau_a^{-1}$ is approximately

$$A(\omega) = \left| \frac{V_o(\omega)}{T(\omega)} \right| = \frac{g_{33} v_s \tau_e}{\sqrt{1 + (\omega \tau_e)^2}} \tag{2.23}$$

where a flat response is seen for $\tau_e^{-1} \gg \omega \gg \tau_a^{-1}$.

The relations (2.22) and (2.23) together give the complete asymptotic frequency domain picture for both limiting cases, shown in Fig. 2.8a,b for all frequencies. This representation illustrates the scaled response to different frequency components making up a time resolved signal. This frequency domain picture illustrates the resolution of signals with different time varying components corresponding to the spatial characteristics of the acoustic wave that generates the electrical signal output.

Asymptotic Bode Plots

a) $\log A$

$g_{33}{}^\tau{}_a$

$g_{33}{}^\tau{}_e$

matched

$\tau{}_a^{-1}$ $\tau{}_e^{-1}$ $\log \omega$

b) $\log A$

$g_{33}{}^\tau{}_e$

$g_{33}{}^\tau{}_a$

$\tau{}_e^{-1}$ $\tau{}_a^{-1}$ $\log \omega$

c) $\log A$

$g_{33}{}^\tau{}_e$

open
backed

$\tau{}_a^{-1}$ $\tau{}_e^{-1}$ $\log \omega$

d) $\log A$

$g_{33}{}^\tau{}_a$

$g_{33}\dfrac{\tau{}_a^2}{\tau{}_e}$

$\tau{}_e^{-1}$ $\tau{}_a^{-1}$ $\log \omega$
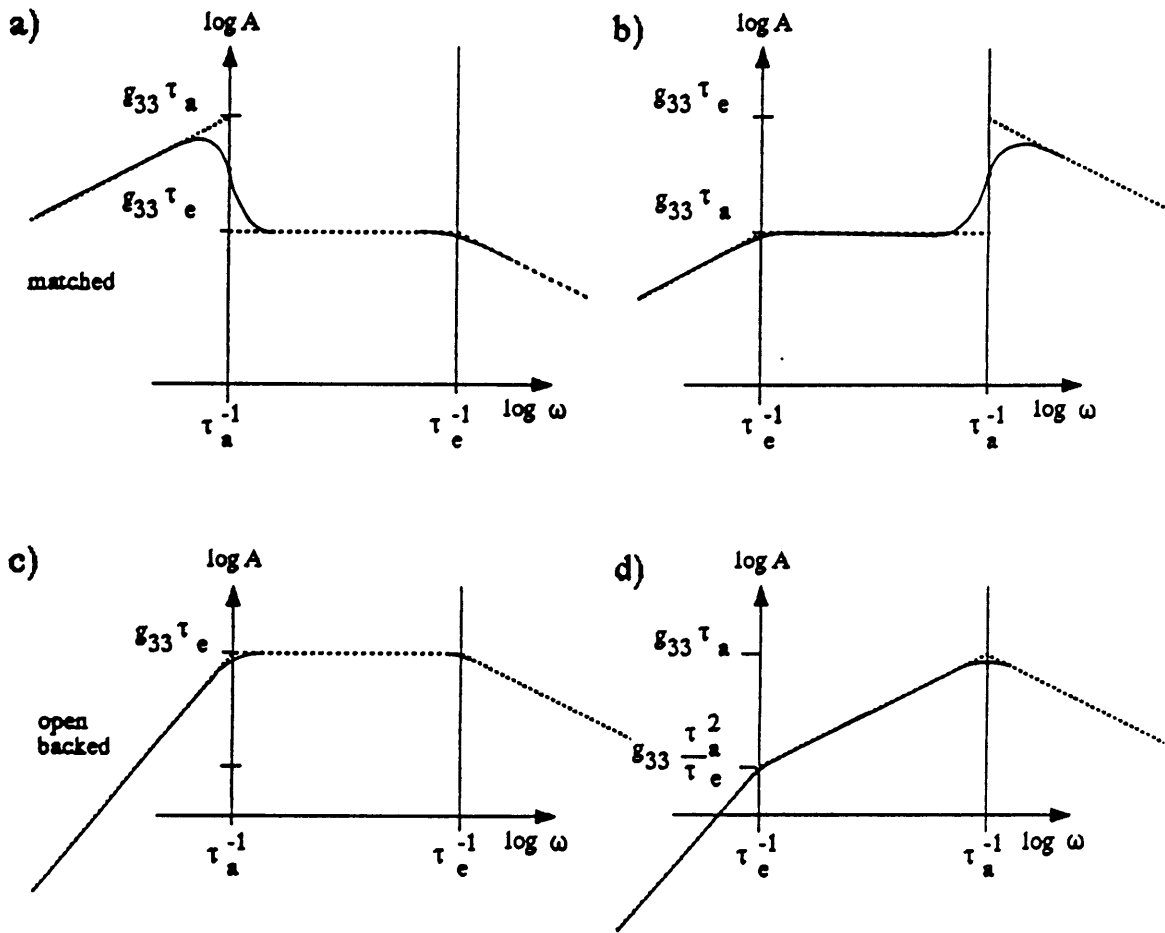
Figure 2.8: Modified Bode plots for four possible transducer configurations connected to a simple resistive load a) and b) are matched at both ends, and c) and d) are open on the back ($\Gamma_b = -1$).

57

Open back transducer

The second configuration is a transducer that is matched on the front side but open on the back ($Z_2 = 0$), so all the signal which impinges on the back surface is reflected with equal magnitude but opposite sign

$$\Gamma_a = 0 \text{ and } \Gamma_b = -1$$

and the signal reflected to the front returns, unimpeded, to the lower electrode. In the time domain, this configuration subtracts the integral of the delayed returning signal from the integral of the arriving signal.

$$V_i(t) = g_{33}v_s \left[\int_{t=0}^{\tau_a} T_z(z,t)dt - \int_{t=\tau_a}^{2\tau_a} T_z(z,t)dt \right] \qquad (2.24)$$

When transformed into frequency space, the result is similar to (2.21) with the sine term squared.

$$\frac{V_i(\omega)}{T(\omega)} = \frac{g_{33}v_s}{j\omega} 4sin^2 \left(\frac{\omega\tau_a}{2} \right) e^{-j\omega\tau_a} \qquad (2.25)$$

By direct analogy to the matched transducer relation (2.21), the output response for low frequencies $\omega\tau_a \ll 1$ will be

$$A(\omega) = g_{33}v_s\tau_a^2 \frac{\omega^2\tau_e}{\sqrt{1 + (\omega\tau_e)^2}} \qquad (2.26)$$

and is proportional to ω^2 for $\omega\tau_e \ll 1$. The inverse transform of (2.26) is proportional to the second derivative. An open backed set-up has a fast gain fall-off for low frequencies. Consequently, this crystal will yield poor resolution of low frequency components corresponding to broad spatial information.

Finding the response to high frequencies follows the same method described previously by breaking down the time domain signal into discrete

Fourier components within the crystal. Since the sine term is squared, the components C_n are multiplied by either 1 or 0 when substituted back in (2.25). Fig. 2.8c,d illustrate the response of an open backed transducer for the two limiting cases. The high frequency responses are the same as for the matched transducer. A narrow pulse whose width is much shorter than crystal acoustic thickness τ_a is not influenced the termination of the back side. Consequently, the high frequency response will be the same for all transducers when $\omega \gg \tau_a^{-1}, \tau_e^{-1}$.

The slope of the high frequency curves on the log-log plots of Fig. 2.8 is -1 which transforms to time integration. Similarly, the positive slopes seen on the low frequency sides correspond to differentiation for a slope of $+1$ and double differentiation for a slope of $+2$. The open backed configurations give the latter characteristics for $\omega \ll \tau_a^{-1}, \tau_e^{-1}$ which also represents a signal fall-off that is twice that of a matched transducer. In order to achieve a flat frequency response, one must be sure that the bandwidth of meaningful signals is within that region; then, the output will be proportional to the signal itself.

The only open-backed arrangement with a flat signal response region in Fig. 2.8 is (c) where $\tau_a \gg \tau_e$. This is a transducer that is acoustically thicker than the arriving signal connected to a low impedance amplifier keeping τ_e very short. Outside the flat region, an output signal will be proportional to the integral, derivative, or second derivative of the arriving acoustic signal. If the frequency components containing charge distribution information overlaps a transition region, recovering the actual acoustic response may be difficult because of noise overwhelming the signal in the attenuated portion of the output spectrum.

Multiple reflections

A transducer with non-zero reflection coefficients at both interfaces has reflections originating from each boundary. This is the general case for any combination of materials with different acoustic impedances Z_a, such that

$$0 < |\Gamma_a, \Gamma_b| < 1$$

whereby a fraction of the stress arriving at any time remains in the crystal and mixes with future signals. Lossless reflections would produce a signal at the fundamental resonant frequency of the crystal, resulting in a sharp frequency domain peak at $\omega = \tau_a^{-1}$. Finite reflection coefficients Γ_a, and Γ_b broaden out the peak and mix incoming signals with only a fraction of previous signals.

Reflections from both surfaces can be treated by direct analogy to the previous two situations. Multiplying the Fourier transform of the time domain open circuit voltage relation with the transform of the RC detector circuit gives the total electrical response. Summing the response over all time, weighted by the appropriate reflections produces the actual transducer response. Since only a portion of the arriving signal is seen across the transducer, the whole relation is multiplied by the transmission coefficient $1 + \Gamma_a$ at the front interface.

The resulting time domain expression for the open circuit voltage across the crystal is

$$V_i(t) = g_{33}v_s(1+\Gamma_a)\int_0^{\tau_a} \sum_{n=0}^{\infty}(-\Gamma_a\Gamma_b)^n\left[T(t + 2n\tau_a) + \Gamma_b T(t + (2n + 1)\tau_a)\right]dt$$

and its associated Fourier transform

$$V_i(\omega) = \frac{g_{33}v_s(1 + \Gamma_a)}{j\omega}\left[\left(T(\omega) + \Gamma_b T(\omega)e^{-j\omega\tau_a}\right)\sum_{n=0}^{\infty}(-\Gamma_a\Gamma_b)^n e^{-2nj\omega\tau_a}\right]$$

60

Asymptotic Bode Plots

a)

log A

$g_{33}{}^\tau{}_a$

$g_{33}{}^\tau{}_e$

τ_a^{-1} τ_e^{-1} log ω

b)

log A

$g_{33}{}^\tau{}_e$

$g_{33}{}^\tau{}_a$

$g_{33}\dfrac{\tau_a^2}{\tau_e}$

τ_e^{-1} τ_a^{-1} log ω
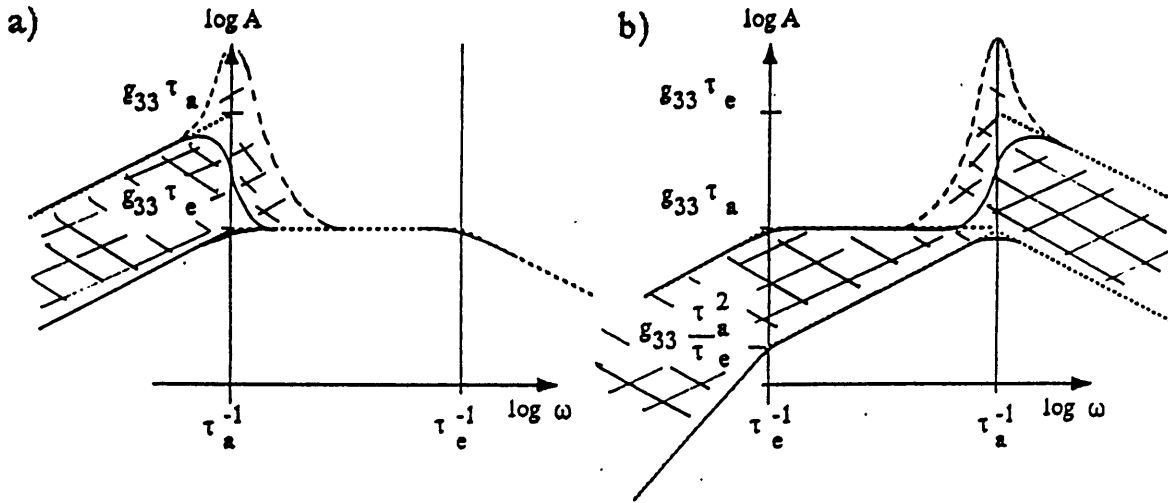
Figure 2.9: Loci of curves for unmatched systems, a) $\tau_a \gg \tau_e$ and b) $\tau_a \ll \tau_e$.

which can be simplified by solving the sum exactly to yield

$$\frac{V(\omega)}{T(\omega)} = \frac{g_{33}v_s(1+\Gamma_a)}{j\omega}\left[\frac{1+\Gamma_b e^{-j\omega\tau_a}}{1+\Gamma_a\Gamma_b e^{-2j\omega\tau_a}}\right] \tag{2.27}$$

and has a pole if $\Gamma_a\Gamma_b = -1$. This is a perfectly mismatched transducer in which case it is a resonator at the fundamental frequency $f_0 = \frac{\pi}{\tau_a}$. This could never occur in practice since it implies that the transducer is free-standing. In a more realistic matching situations, the transducer is loaded, at least on one side, making the relation stable and not resonant.

The amount of ringing depends on the size of both reflection coefficients as expected from (2.27). When the limiting cases of $\Gamma_a = 0$, and $\Gamma_b = 0$

or $\Gamma_b = -1$, there are no oscillations, and the results are the same as in Fig. 2.8. However, the loci of solutions for finite Γ_a and Γ_b are between the two extrema, with peaks near the resonant frequency and whose widths depend on the reflection coefficients. The solutions are illustrated in Fig. 2.9 for the asymptotic approximation appropriate for first arrival signals as discussed earlier.

Combining the open circuit frequency domain response with the detector response, and taking the magnitude gives the result

$$A(\omega) = \left| \frac{V_o(\omega)}{T_i(\omega)} \right| = \frac{g_{33} v_s \tau_e (1 + \Gamma_a)}{\sqrt{1 + (\omega \tau_e)^2}} \left| \frac{1 + \Gamma_b e^{-j\omega \tau_a}}{1 + \Gamma_a \Gamma_b e^{-2j\omega \tau_a}} \right| \qquad (2.28)$$

for the generalized frequency domain impulse response of an acoustic transducer sandwiched between a delay line and an absorber at the back. The resonant configuration gives a large response to signal components near τ_a^{-1}, but attenuates lower frequency components and superimposes a damped oscillation over the signal.

The next section presents some numerical simulations of the principles described in this section. A model has been designed to account for the propagation loss of a delay line, and the time domain response of a transducer with different values of Γ_a and Γ_b. The simulations are then compared to an actual impulse response output signal to show the validity of the model and the approximations.

2.3   Impulse and Step Response

The time domain response determines how a transducer receives an arbitrary waveform. To simulate the time domain impulse response, a 20 ns pulse with zero attenuation was used as input to the detector function described
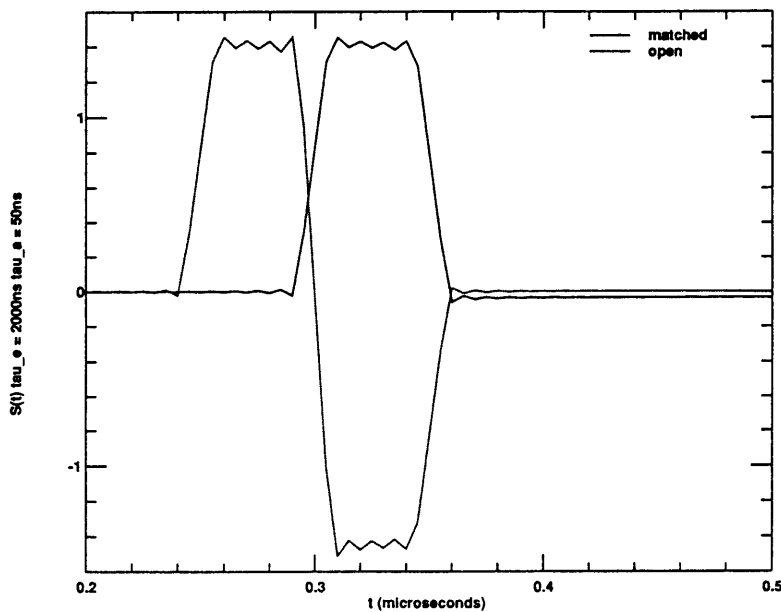
Figure 2.10: Simulation of the impulse response of a piezoelectric crystal having $\tau_a = 50$ ns and $\tau_e = 2000$ ns.

in section 2.1.3. The output from 0 to 1 μs is divided into 400 points for a numerical simulation, making the resolution on the output accurate to within $\approx$ 10 ns, justifying a 20 ns pulse to approximate a true impulse. The following four figures show the simulated impulse and the step responses of two transducers with zero delay line attenuation, both have $\tau_a = 50$ ns, while $\tau_e = 2000$ ns for Figs. 2.10 and 2.11 and $\tau_e = 10$ ns for the plots of Figs. 2.12 and 2.13.

Aside from numerical noise, these simulations clearly show how the output of a transducer approximates a stress signal, its integral, derivative, or second derivative, depending on which limit the system resides. If the same transducer is open on the back side, the output looks like a derivative of the matched case as seen in Fig. 2.10. A step input gives a response proportional to the integral of the impulse response for both the matched and the open
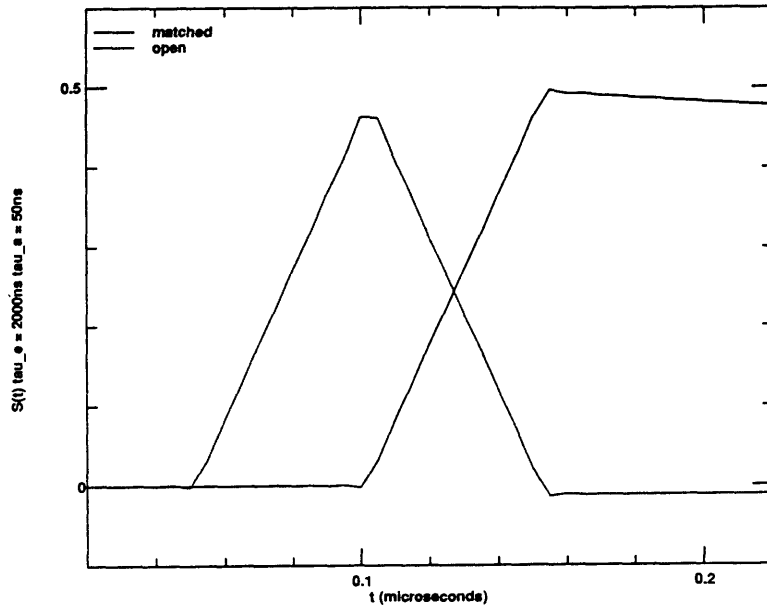
Figure 2.11: Simulation of the step response of a piezoelectric crystal having $\tau_a = 50\ ns$ and $\tau_e = 2000\ ns$.
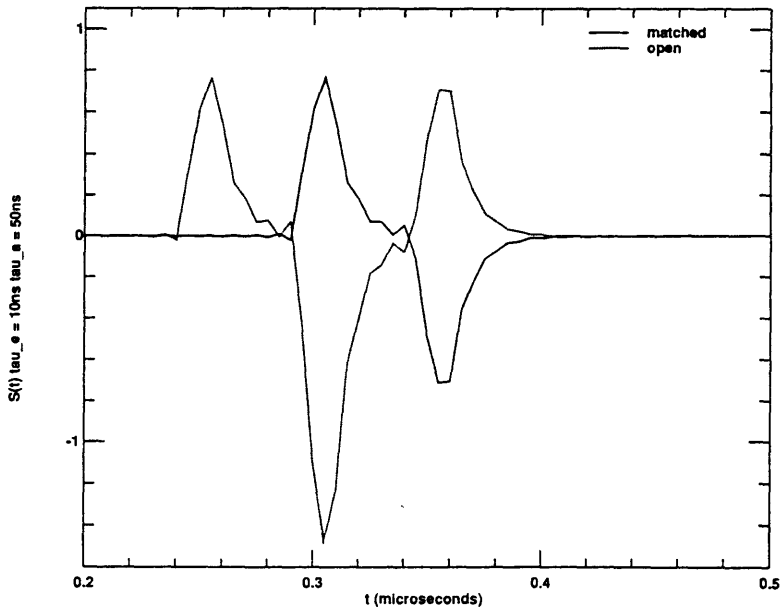
Figure 2.12: Simulation of the impulse response of a piezoelectric crystal having $\tau_a = 50\ ns$ and $\tau_e = 10\ ns$.

64
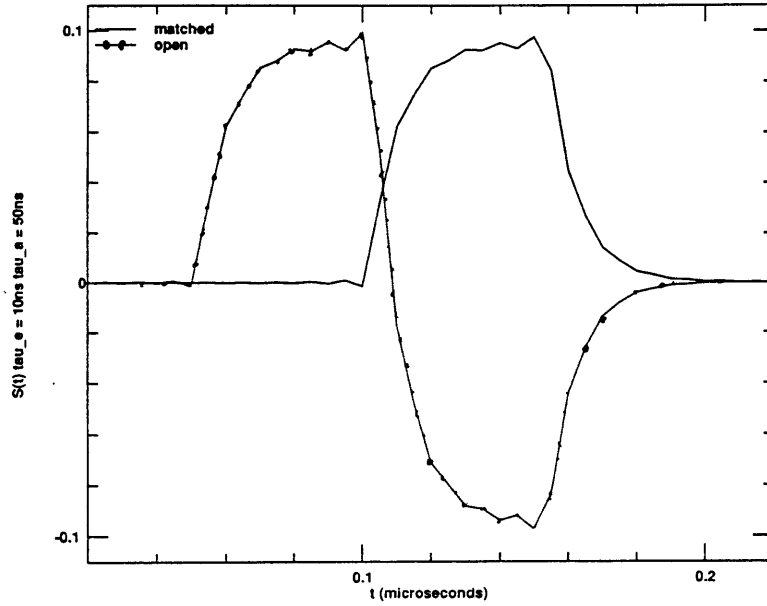
Figure 2.13: Simulation of the step response of a piezoelectric crystal having $\tau_a = 50$ ns and $\tau_e = 10$ ns.

backed transducer, as demonstrated by comparison to Fig. 2.11.

The short τ_e limits are shown in the Figs. 2.12 and 2.13. These plots demonstrate the system response to an impulse and a step for both matched and open backed transducers with $\tau_e = 10$ ns. The step response is also approximately proportional to the integral of the corresponding impulse response. The impulse response of an acoustically matched transducer gives an output signal proportional to the derivative of the input pressure wave for signals much wider than τ_a

$$\frac{dS}{dt} = \lim_{\Delta t \to 0} \frac{S(t) - S(t - \Delta t)}{\Delta t} \tag{2.29}$$

and the unmatched arrangement gives a signal proportional to the second derivative for the same input by comparison to the definition

$$\frac{d^2 S}{dt^2} = \lim_{\Delta t \to 0} \frac{S(t - \Delta t) - 2S(t) + S(t + 2\Delta t)}{\Delta t^2} \tag{2.30}$$

65

where $\Delta t = \tau_a$. The differential limit is approached when the signal width is much larger than τ_a.

Once reaching its minimum value, the signal decays exponentially as

$$e^{-\frac{t}{\tau_e}}$$

determined by the electrical time constant τ_e. For times much shorter than τ_e, the drop off is barely detectable as seen in Fig. 2.10, although the output of the matched transducer remains below zero for many time constants, $3\tau_e = 6~\mu s$ for this transducer. When $\tau_e < \tau_a$, the output approaches a narrow impulses whose width is approximately $\frac{1}{2}\tau_e$. Finite area under the curve determines the signal strength of a received impulsive pressure wave. A shorter τ_e consequently results in narrower resolution, but proportionally smaller signal strength.

A real system excitation is more accurately characterized by a finite rectangular pulse whose width is of the same order as τ_a, As long as the system remains completely linear, signal processing can recover the charge waveform by deconvolution with the appropriate system function. Next will be presented some simulations of commonly found transducer applications. This analysis has lead to the selection of the final transducer setup used in the detection apparatus.

2.3.1 Simulation Results

Integrations for the Fourier transforms are performed with a simple trapezoid approximation, sufficient for periodic waveforms [30]. The following simulations are calibrated in time to a square pulse excitation of 160ns. The magnitude of the input signal is 1; however, half the signal propagates in each direction, making 0.5 the peak signal in these simulations. To ob-

66
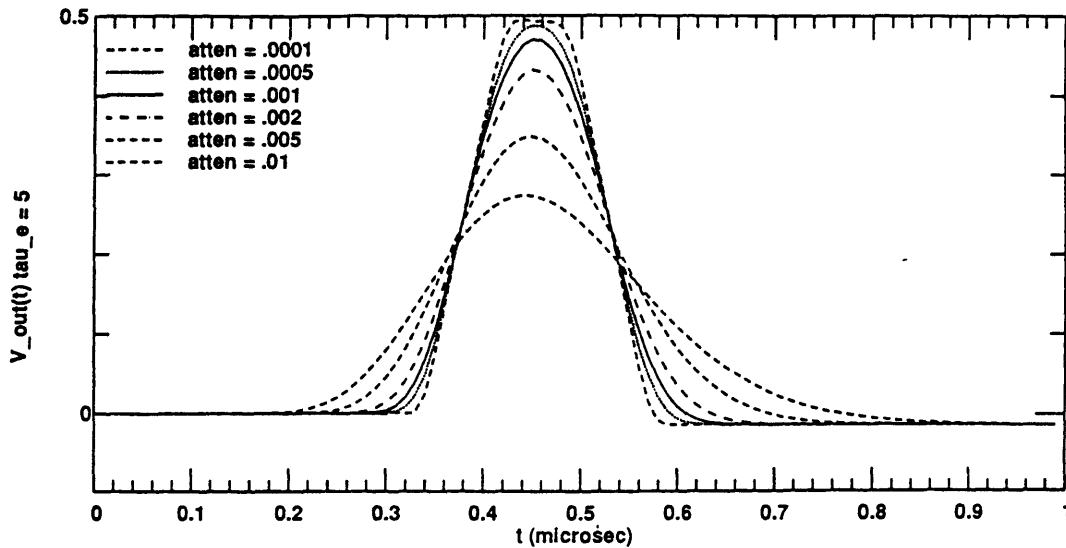
Figure 2.14: Simulation of a signal received by a transducer with $\tau_e = 5\mu s$, $\tau_a = 80ns$, a 160ns pulsewidth, and several values for the attenuation coefficient α = "atten".

serve the effects of attenuation, different values for α have been substituted with constant electrical and acoustic time constants τ_e and τ_a as seen in Fig. 2.14. Attenuation spreads out the signal pulsewidth by removing the high frequency details of the incoming signal, while overall characteristics of the pulse are preserved.

The effect on the pulse shape of increasing the attenuation coefficient is exactly the same as allowing the signal to propagate farther. Comparing the family of pulses in Fig 2.6 with those of Fig. 2.14 shows that a short delay line made with a more lossy material will produce a pulse which looks identical to a longer delay line made with less lossy material. Fig. 2.14 shows the detected signal at the same point within the delay line, perfectly matched on both ends ($\Gamma = 0$).
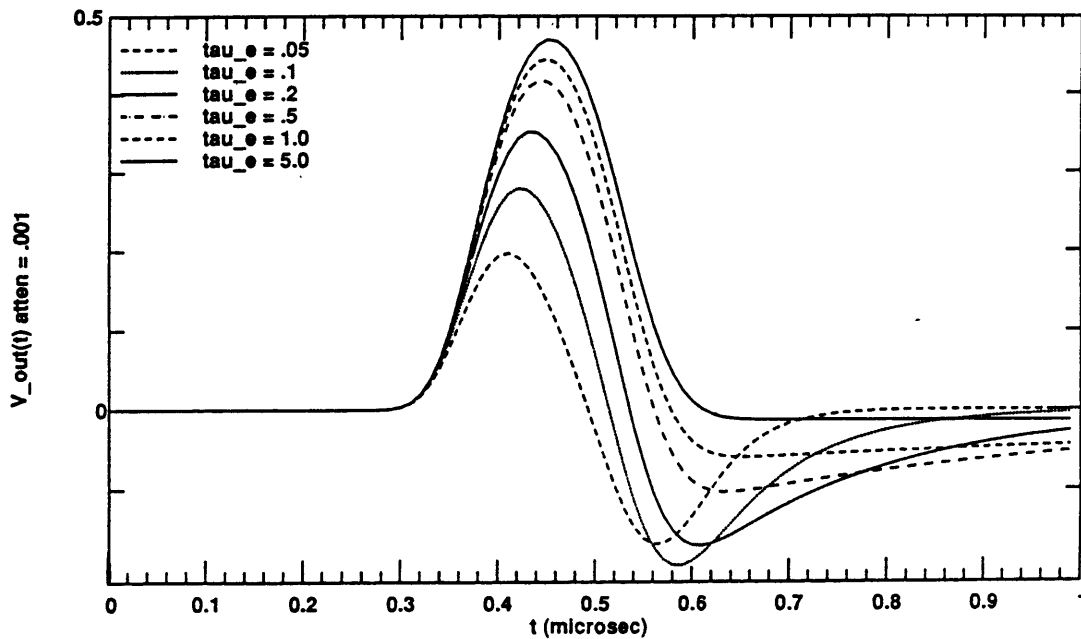
Figure 2.15: Simulation of a matched transducer having acoustic time constant $\tau_a = 80$ ns receiving a 160 ns pulse through a detection circuit with different electrical time constants τ_e.

The effect of varying electrical time constant is illustrated by the series of simulations shown in Fig. 2.15 where the electrical time constant (τ_e) is changed from 0.05 to 5.0 while all other parameters are held constant. The attenuation coefficient is fixed at 0.001, the pulsewidth is maintained at 160 ns and τ_a is at 80ns. There are no reflections in this simulation; hence, the zero crossing is due to the interaction of the incoming signal with the RC detection circuit. The amplitude becomes smaller with τ_e, as does the length of time to recover; thus, the tradeoff of amplitude verses recovery time becomes apparent with decreasing RC.

The matched transducer of Fig. 2.16 illustrates that reflections do not cause a significant deviation from the ideal pulse, even when half the signal is reflected for $\Gamma = 0.5$. However, when the same crystal is not matched on

68
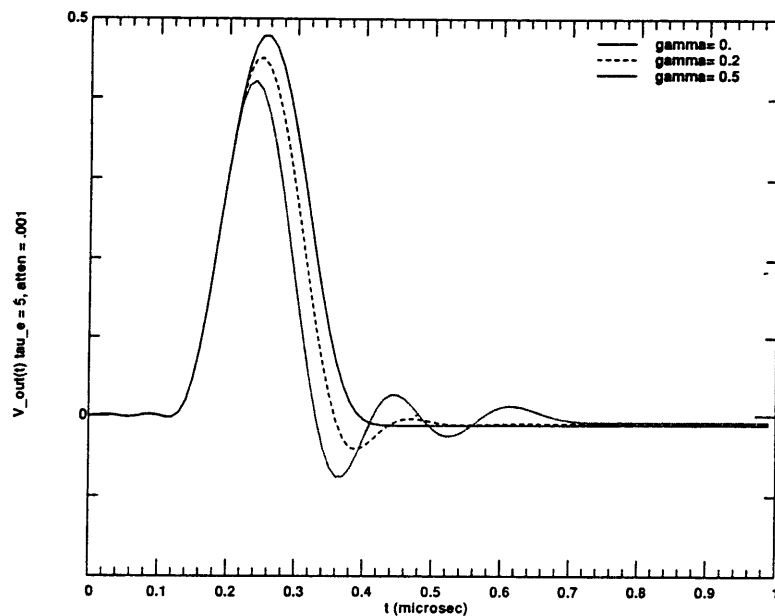
Figure 2.16: Matched transducer response with $\tau_e = 5\mu s$ and various reflections

the back side, as in Fig. 2.17, the undershoot is more significantly altered. Both of these simulations assume the electrical time constant is very long ($5\mu s$) and the output is approximately the integral of the stress signal across the transducer, which is 80 ns long.

For the next two figures, $\tau_e = 10$ ns, so the transducer behaves like a signal differentiator. The first set, Fig. 2.18, shows that the reflections give a very clear ring after the signal arrives. The $\Gamma = 0$ trace of Fig. 2.18 does not ring and is similar to the $\Gamma = 0$ trace of Fig. 2.17, which is approximately the derivative of Fig. 2.16. Reflections in the matched transducer with $\tau_e = 10$ ns are still not as significant as in the open back case of Fig. 2.19. Here, the $\Gamma = 0$ trace looks approximately like the derivative of Fig. 2.18, and the second derivative of Fig. 2.16, as expected from the systems analysis.

Reflections interfere with the incoming signal and can be tuned to re-

69
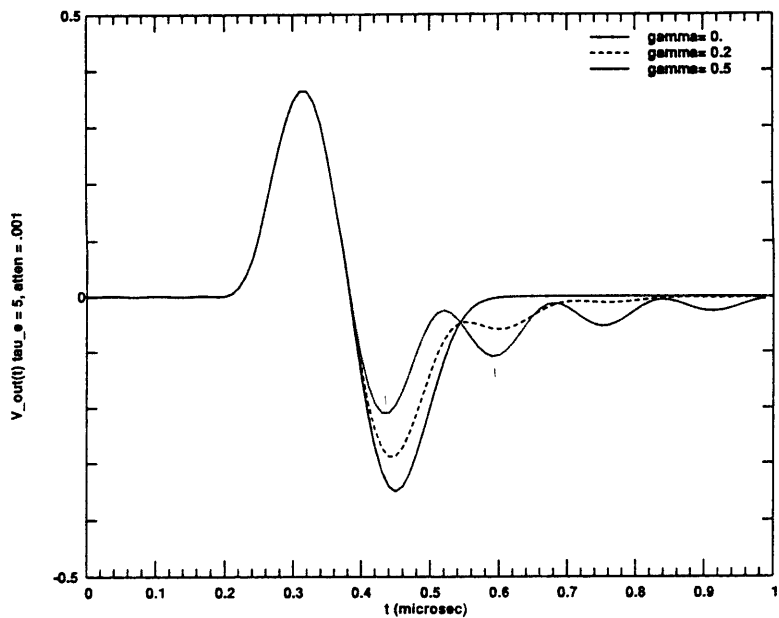
Figure 2.17: Open ended transducer response with $\tau_e = 5\mu s$ and various reflections
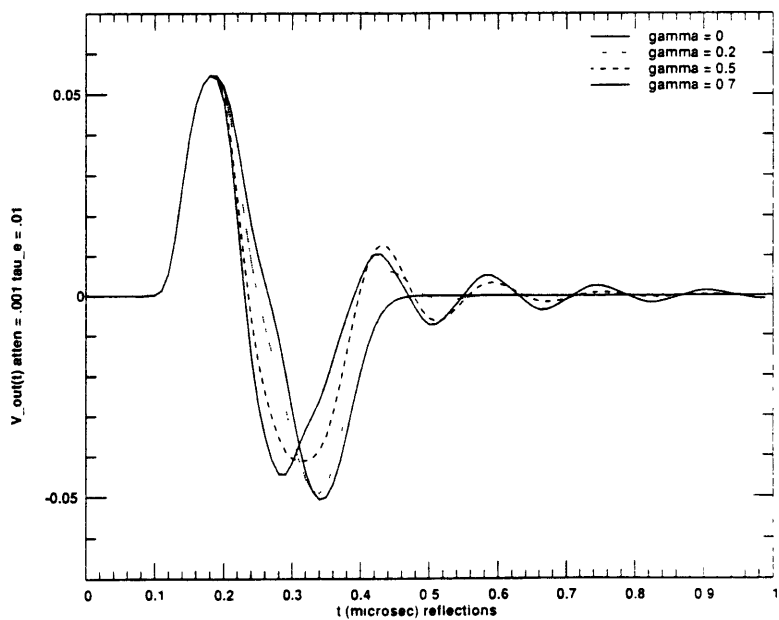
Figure 2.18: Matched transducer response with $\tau_e = 10ns$ and various reflections

70
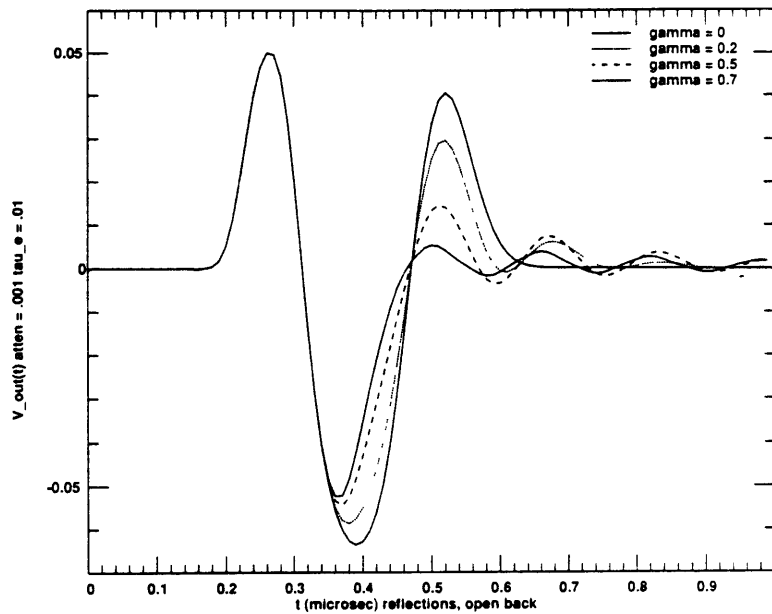
Figure 2.19: Open ended transducer response with $\tau_e = 10ns$ and various reflections

duce the ringing seen afterwards. The pulsewidth in these simulations is approximately twice the acoustic time constant τ_a, so the second reflection is canceled out in the largest Γ trace of Fig. 2.19. This illustrates how a poorly matched transducer can be tuned by a pulse whose width is twice τ_a. If the reflection coefficient is high, this second derivative signal can be forced to approximate a first derivative, improving the low frequency response of the detector.

A transducer set-up similar to the one used by Maeno et.al [25] has been simulated and can be compared with the recorded output. A 1.5 mil thick $LiNbO_3$ transducer with $\tau_a = 50$ ns was mounted on an aluminum delay line with radius $R = 1.5$ cm and length $L = 3.0$ cm. The delay time $\tau_{delay} = 5.8\mu s$ as seen in Fig. 2.20, suggests that $\tau_{max} = 2.3\mu s$, is a much longer time than the length of the test. The transducer was mounted on the

back face, calling for an *open back* simulation.

The reflection coefficient is calculated from the acoustic impedances of Al and $LiNbO_3$

$$Z_a = 1.73 \text{ and } 3.40 \frac{gm}{cm^2 \mu s} \qquad .$$

respectively[2] which yields $\Gamma \approx 0.3$. The electrical time constant was approximated as $\tau_e = 10ns$ from the measured capacitance, $C = 200$ pf, times 50Ω for the amplifier input impedance. The simulation is shown in Fig. 2.21 and it looks very close to the recorded data. Hence, the numerical results correspond well with experiment.

The simulation allows one to analyze the complete one-dimensional response of the delay line and the piezoelectric transduction in the ESAW acoustic imaging scheme. Deviations from the simple linear model may be due to imperfect excitation, surface waves, scattering within the delay line, or external electrical noise. The detection apparatus also introduces noise, so the frequency response is limited by the signal to noise ratio at the high frequency end. When an output waveform is deconvolved with its appropriate impulse response, the numerical filter determines the maximum frequency at which the signal can be detected over the system noise.

2.4 Deconvolution

A charge distribution can be divided into many thin sheet charges of equal width. Each charge results in a pulse amplitude proportional to the charge magnitude. The resulting wave form is the convolution of the impulse response of the pulse-transducer system with the charge profile. Therefore, deconvolving the output signal with the impulse response of a known sheet

---

[2]from Appendix B of the textbook by G. Kino [27]

Time resolved waveform
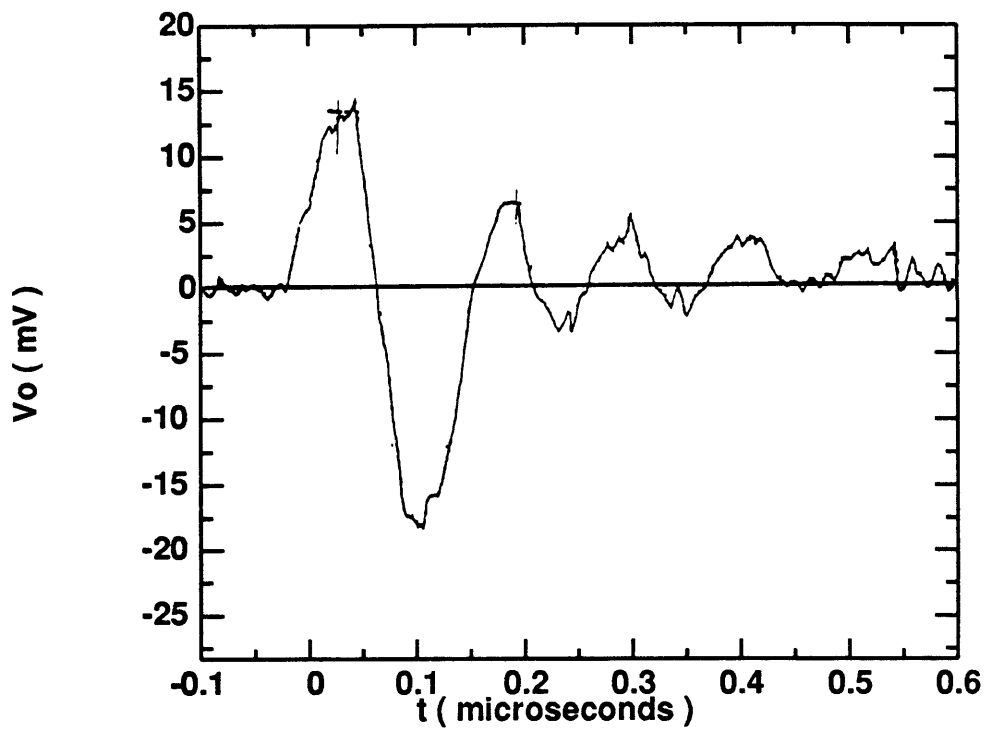
Figure 2.20: Recorded data from a 100ns excitation pulse through an aluminum delay line into a $LiNbO_3$ transducer with $\tau_a = 50ns$.
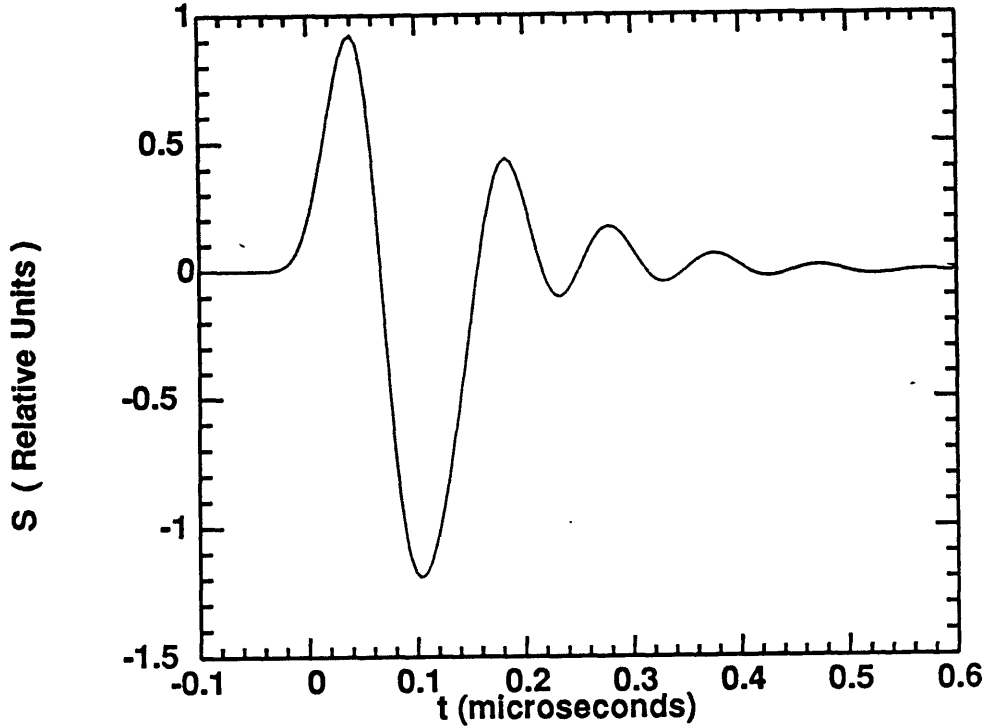
Figure 2.21: Simulation of a 100ns excitation pulse through an aluminum delay line into a $LiNbO_3$ transducer with $\tau_a = 50ns$.

charge reconstructs that profile. This principle is illustrated in Fig. 2.22.

A fast Fourier transform algorithm computes as many frequencies as spatial points for a string of length 2^n where n is an integer. Any time domain signal is transformed in this way to produce a corresponding frequency domain spectrum containing the same number of points. If the output voltage signal and the impulse response signal are found and placed in strings of equal length, their corresponding spectra may be computed resulting in transformed strings.

A transformed output voltage waveform $V(\omega)$ and impulse response $H(\omega)$ produce the transformed charge distribution $P(\omega)$ by dividing numerically

$$P(\omega) = \frac{V(\omega)}{H(\omega)} \tag{2.31}$$

at every frequency ω. The charge distribution is then recovered by taking

74
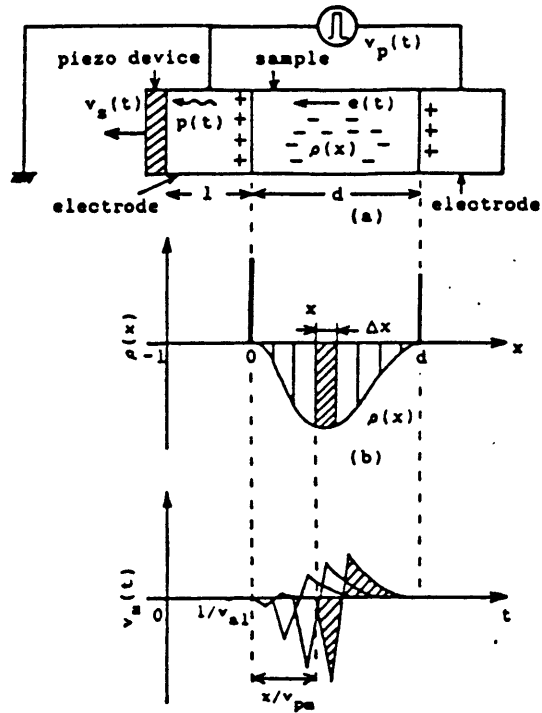
Figure 2.22: Demonstration of the convolution principle applied to a charge distribution $\rho(z)$ between the electrodes. b) charge density plotted with z. c) resulting output voltage signal [25].

the inverse transform of $P(\omega)$ to yield $p(z = v_s t)$.

Knowing the high and low frequency limits of real information, the resulting transformed distribution is filtered by removing the extraneous components. High frequency noise is magnified by the deconvolution process, so only a small portion of the frequency spectrum is used. Consequently, the output can be made as smooth as desired by removing higher frequency components, but this also limits the resolution.

A filter algorithm used by the ASYST[3] software package for IBM compatible personal computers provides a sharp cutoff frequency with a smooth time domain transform. The filter function is called *Blackman's lucky guess*, described by the window function

$$W(f) = 0.42 + 0.5cos(\pi \frac{f}{f_0}) + 0.08cos(2\pi \frac{f}{f_0}) \qquad (2.32)$$

for all frequencies f and a cutoff frequency f_0.

A narrower resolution may be achieved with a higher cutoff frequency; although, proportionately more noise will be introduced. For this reason, the deconvolution process is only reliable as a complement to the time resolved data for extracting information. Reliable output is obtained by analyzing the deconvolved charge distributions after comparison with the raw time data.

2.5 Electrostriction considerations

Electrostatic force exerted on the material due to an applied field depends on the charge associated with that field, and the electrostriction coefficient

---

[3]ASYST is a signal processing software package copyright 1985 by Macmillan Software Company, a division of Macmillan Inc.

γ, defined as

$$\gamma = \epsilon(1 + c_a)$$

[36, 37] where c_a is a material constant defined by

$$c_a = \frac{\rho_{m0}\partial\epsilon}{\epsilon\partial\rho_m} = \frac{\gamma}{\epsilon} - 1 = const$$

with ρ_m representing the mass density. One can determine γ by measuring the electrostriction force with an applied field [36] and ϵ from the capacitance [32] to get a value for c_a.

The force per unit area on a thin sample with no embedded charge is found directly by

$$F_z = \gamma E_z^2$$

for a uniform electric field E_z terminating on the sample boundary. Therefore, if $E_z(t)$ contains a DC and a time varying component

$$E_z(t) = E_{dc} + e_z(t)$$

then

$$E_z^2 = \frac{1}{2}E_{dc}^2 + E_{dc}e_z(t) + \frac{1}{2}e_z^2(t)$$

whereby the first term has no time dependence and shifts the equilibrium stress in the presence of localized charges. The perturbation field $e_z(t)$ generates a stress wave proportional to the electrostatic force exerted at the surface

$$f(t) = \gamma E_{dc}e_z(t) + \frac{1}{2}\gamma e_z^2(t) \qquad (2.33)$$

where E_{dc} is the surface field due to the applied DC voltage. If the DC field is much larger than the excitation field, the second term in (2.33) may be ignored and the DC field term may be replaced by the surface charge where

$$Q_s = \frac{\epsilon}{d}V_{dc}$$

77

where V_{dc} is the applied DC voltage used to calibrate the detection system.

A bulk sheet charge of value Q_s will respond in the same way as one on the surface without the $e_z^2(t)$ self-field term. The stress density for an embedded sheet charge under excitation by a small field is therefore

$$T_q(t)_z = \frac{\gamma}{d} V_{dc} e_z(t) = (1 + c_a)\, e_z(t) Q_s(z)_{x,y} \qquad (2.34)$$

for constant charge in the x-y plane. Making the substitution for Q_s at the surface with the induced surface charge ϵE_{dc}, the calibration stress signal T_o is the signal induced by a known applied voltage V_{dc},

$$T_o(t) = \frac{\epsilon(1 + c_a)}{d^2} \left[(V_{dc} + v_{pulse})\, v_{pulse}(t) \right]$$

allowing one to calibrate the detector to a known charge

$$Q_0 = \frac{\epsilon\, (V_{dc} + v_{pulse})\, v_{pulse}(t)}{d^2}$$

being the surface charge due to capacitance and applied voltage. The resulting acoustic signal will be considered the impulse response, calibrating the acoustic waveform due to an internal charge with a corresponding surface sheet charge. The sign of the charge is also preserved since a negative charge launches an opposite stress wave from a positive charge and it is distinguishable by the transducer.

If the embedded charge is not located at a single sheet, but is distributed over an area within the bulk, the resulting pressure wave will be a time varying signal across the sample, uniform in x and y. A charge distribution $\rho_q(z)_{x,y}$ produces an acoustic stress perturbation in time and space $F_0(z,t)$ which launches an acoustic wave $T_i(z,t)$, as described in section 2.1

$$F_0(z,t) = \frac{\gamma}{\epsilon} E_z(t)\rho_q(z)_{x,y} \qquad (2.35)$$

78

and propagates away at the velocity of sound to be received by the transducer. The constant term, $\frac{\gamma}{\epsilon}$, is a material parameter, so it does not vary from one sample to the next. Once the stress produced from a known sheet charge layer is found, the detector can be calibrated to charge layers from different samples of the same material. A sample containing bulk space charge that is exposed to the impulsive perturbation field, produces a stress waveform that mimics the charge distribution. The distribution is then calibrated by the surface charge of a sample that is free of bulk space charge with an applied DC voltage to produce the calibrating surface sheet charge.

Details of the final system will be presented next. Test samples were produced to simulate sheet charges embedded within a PMMA dielectric solid and compared to the signal produced from a surface sheet charge. Thus, it will be shown that the arrangement used for taking ESAW data provides actual charge profiles in the tested polymer samples.

2.6 Acoustic Impulse Response

The delay line is made of brass because it has an acoustic impedance similar to the PZT detector [27]

$$Z_{PZT} = v_s \rho_{m0} = 3.3 \frac{gm}{cm^2 \mu s}$$

$$Z_{brass} = 4.0 \frac{gm}{cm^2 \mu s}$$

For an example of a polymer sample, consider polyethylene in the detection apparatus. If the initial pulse stress due to the electrical excitation is T_i, half the signal goes in each direction so

$$T_t = \frac{T_i}{2} (1 + \gamma) = T_i \frac{Z_b}{Z_b + Z_s} \qquad (2.36)$$

79

reaches the detector through the delay line. PE has an acoustic impedance
of

$$Z_s = .18 \frac{gm}{cm^2 \mu s}$$

making a reflection coefficient of $+0.9$, so most of the signal is reflected back
into the sample. Because the brass has such a high impedance, a large stress
is transmitted $(T_t = 0.85 T_i)$ to the detector.

2.6.1 Front Surface Sheet Charge

The magnitude of the stress waves resulting from a sheet charge at the
lower electrode interface is found by solving the wave equation with the
same boundary conditions discussed in section 2.1 :

$$T_{tb} + T_{rs} = T_{is} \tag{2.37}$$

for T_{rs} representing the component moving into the sample as if it were a
reflection from the surface and T_{tb} moving through the electrode, transmitted
to the detector.

The continuity condition which must be satisfied is the velocity $\dot{u}$ across
the boundary. This gives the result for a transmitted stress wave [33].

$$T_{tb} = T_{is} \frac{Z_b}{Z_b + Z_s} = T_{is} \frac{1 + \Gamma}{2} \tag{2.38}$$

which is the same result as (2.36). This states that the acoustic response
of a sheet charge at the surface has the same response of a sheet charge
originating from within the bulk, allowing the calibration of an impulsive
sheet charge within the sample to a surface sheet charge at the electrode.
The acoustic mismatch between the sample under test and the acoustic
delay line has no effect on the relative signal received. Consequently, as
long as the impulse response is chosen with the same sample material, a

80

single sheet charge response signal can be used to deconvolve all subsequent charge distribution profiles.

A liquid interface assures that no air gaps occur at the interface. Non-uniformities at the plastic surface will be acoustically coupled to the oil as it fills in microvoids. Silicone oil works well for this since it is acoustically very close to PE and PMMA with $Z \approx 0.2$ while having a similar dielectric constant of $\epsilon \approx 3$, making a good electrical match [35].

2.6.2 Opposite Surface Sheet Charge

The response to a sheet charge residing at the upper electrode will experience the same conditions for the magnitude of the generated signal. The portion of the initial stress which propagates in the direction of the sample, towards the detector, is the conjugate of that which propagates into the electrode. The upper electrode is also made of brass, so the transmitted signal from $z = d$ has

$$T_{td} = T_{id}\frac{Z_s}{Z_b + Z_s}\left(1 + \Gamma\right)$$

Since the acoustic impedance of brass is much larger than that of PMMA, the resulting signal will be greatly attenuated from the upper electrode.

The resulting signal is much larger than could be expected with this assumption since the actual boundary at that surface is a thin oil layer in contact with the brass. The result is some effective impedance due to the interactions between the polymer, oil, and the brass. Details of the interface are important at the upper interface, in contrast to the lower interface, as seen by the relations (2.38) and (2.36). Therefore, in order to observe the details at both interfaces, the sample should be profiled twice, once from each side.

81

2.6.3 Bulk Charge

Measuring bulk charge as a superposition of distributed sheet charges requires one to use signal processing to recover the actual profile from the time domain signal. The surface sheet charge (per unit area) resulting from the perturbing electrical pulse across the insulator is the sum of the DC charge and the component due to the excitation.

$$Q_s = Q_{s0} + \frac{\epsilon}{d}E_z(t)$$

where Q_{s0} is the static surface charge and is either the result of internal charges or an externally applied voltage.

If the excitation field is small by comparison to the static internal field, a buried charge and its subsequent images on the outer surfaces will give signals proportional to their charges. This has been performed with a double layer of PMMA with the results shown in Fig. 2.23. A thin aluminum sheet, 10 μm thick, was glued between two sheets of PMMA, one 6.4 mm and the other 2.9 mm thick. A 15KV DC voltage was applied at the center electrode while the outer two surfaces were grounded. The resulting time and deconvolved waveforms are shown. The time data shows the result of the sample with applied voltage superimposed on the same sample with zero volts applied in order to visualize the actual response.

In this example, the voltage was applied through a 100 MΩ resistor to the aluminum sheet. The capacitance can be approximated by assuming the electrode area is 7 cm^2 and the permittivity is 3.7 ϵ_0, giving approximately 0.8 pf. This makes the RC time constant of the system very long with respect to the pulsewidth $\Delta t = 10^{-7} sec$

$$RC = 8 \times 10^{-5} sec \gg 10^{-7} sec$$
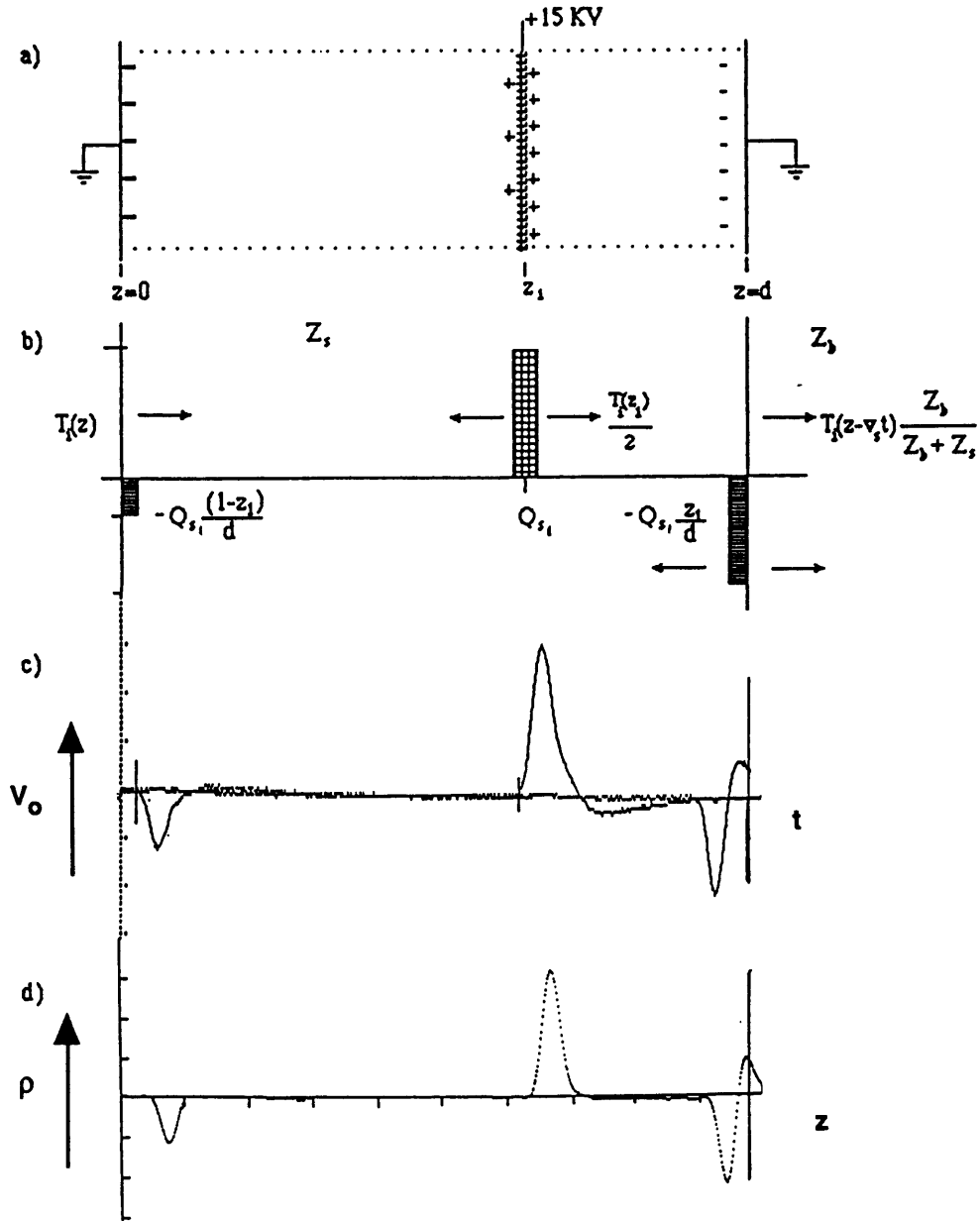
Figure 2.23: ESAW principle for sheet charge a) Q_{s1} and image charges Q_{s0} and Q_{sd} on the electrodes, b) resulting pressure wave signal, c) actual induced voltage waveform resulting from reception by the transducer, and d) the resulting deconvolved charge profile.

The embedded positive charge Q_{s1} is located at z_1. Image charges Q_{s0} and Q_{sd} appear at the front and back electrodes under short circuit conditions as seen in c) and d) of Fig. 2.23b. Pressure pulses are produced with widths equal in time to the applied pulsewidth, and amplitudes proportional to their corresponding charge. The resulting pulses propagate out the insulator, through the electrodes, into the piezoelectric transducer, producing a voltage waveform $V_s(t)$. The signal is delayed by the lower electrode in order to separate the acoustic signal from electronic noise from the voltage pulse. This voltage waveform is then amplified, detected, and recorded by the digitizing oscilloscope.

The first and second peaks of Fig. 2.23c are true indications of the characteristic charges; however, the signal due to the top electrode ($z = d$) is obscured by an immediate reflection at that surface. Consequently, to find the surface charge at both electrodes, two tests should be performed, one with one side up, then another with that same side down. Comparing the two waveforms provides a measure of the actual charges at the surface on each side under short circuit conditions while providing a redundant test for the bulk charge in between.

The area under the processed waveform (Fig. 2.23d) is proportional to the relative total charge in that portion of the bulk, whether it lies in a single sheet or is distributed. The total signal scales directly with pulse field as well as embedded charge, so it is proportional to the impulsive voltage and inversely proportional to the sample thickness.

The impulse signal is obtained by applying a known DC voltage across the bulk-charge-free sample of thickness d and relative permittivity ϵ. The output scales linearly with applied voltage and gives the acoustic response

to an impulsive charge layer with a known magnitude. Since the field scales linearly with thickness, the output must also be scaled with sample thickness for the same waveform is to be used on other samples of the same material.

The deconvolution in Fig. 2.23 was performed using the response of a 5.28 mm PMMA sample with 10 KV DC excitation. The filter cutoff frequency was selected at 10 MHz to eliminate most of the noise introduced by the system. The measured charges at each electrode, found by integrating under the peaks, were determined to be: -8.0 and 24.2 $\frac{nC}{cm^2}$ at $z = 0$ and $z = z_0$ respectively. The actual charge density was found by assuming $\epsilon = 3.7\epsilon_0$, were expected to be -7.65 and 24.4 $\frac{nc}{cm^2}$, both values are within 5%. The following section describes how a calibrated charge distribution is obtained from numerical filtering and deconvolution by reference with a known sheet charge.

2.7 Calibration

The waveform resulting from an infinitely narrow charge layer is taken as the impulsive system response. The output waveform of Fig. 2.24 is from a 0.528 cm thick PMMA sample with a DC potential of 10 KV applied and no internal space charge. The top curve is the scaled down input voltage pulse ($V_{peak} = $ -1500 volt, width = 120 ns). The lower curve is the delayed output from the matched transducer made of Lead Zirconium Titanate (PZT) sandwiched between a brass delay line and absorber. The initial pulse arrives at the transducer after 4.38 μs and the second pulse arrives 1.94 μs later. Thus, the velocity of sound in the sample is $2.72\frac{mm}{\mu s}$, a value in agreement with the literature.

The first 1.5 μs of this waveform was used as the impulse time function

Time resolved waveform
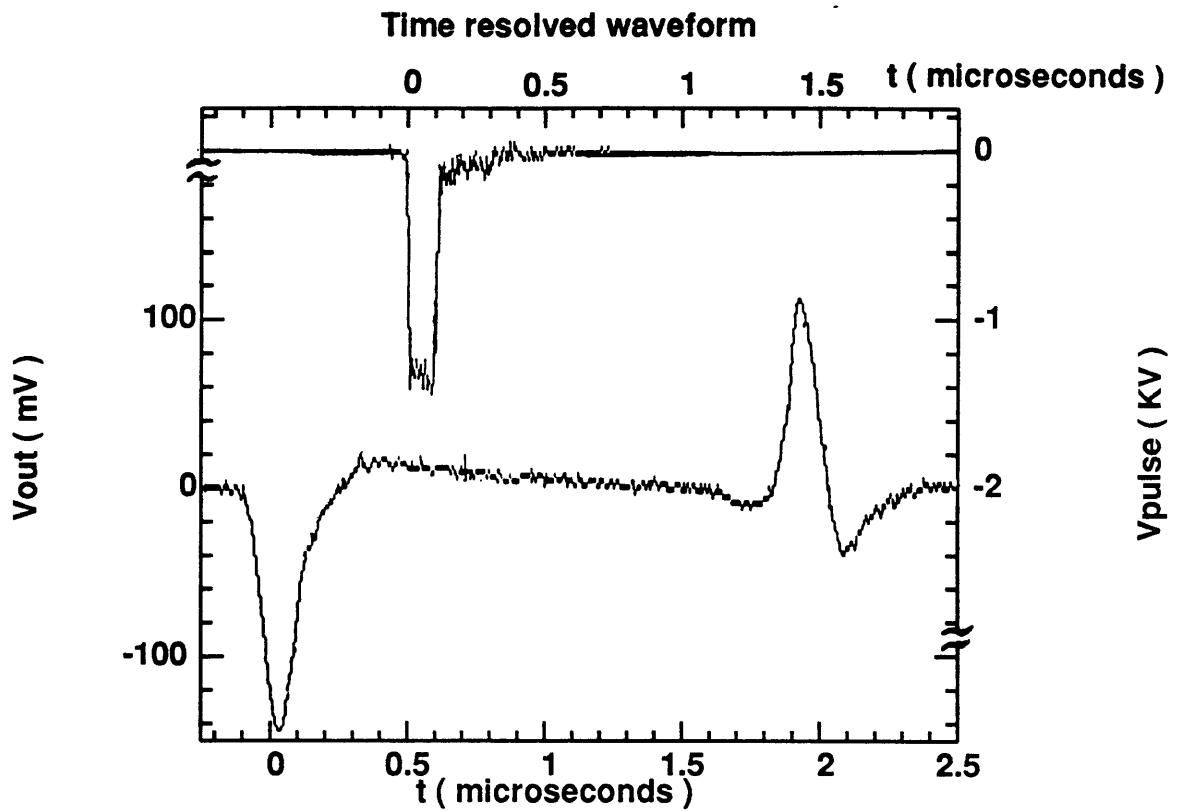
Figure 2.24: Voltage pulse input, V_{pulse} (top), and amplified transducer output, V_{out} (bottom); Applied pulse preceeds acoustic response by the coupling delay of 4.38 μs. Surface charge results from an applied DC voltage of 10 KV across a 5.28 mm PMMA slab with no internal charge distribution.

86

to deconvolve the whole waveform. The result is seen in Fig. 2.25 after averaging with a 10 MHz filter. The small amount of structure in the region between the two electrode peaks is due to the associated error. In this calibration example, a sample without bulk space charge, the surface charge peaks are only due to the 10 KV applied DC and $\frac{1}{2}V_p = 0.75$ KV from the pulse. Therefore, the applied E-field is

$$E = \frac{10.75 \ KV}{0.528 \ cm} = 20.4 \frac{KV}{cm}$$

producing a surface sheet charge density, calculated from the relative permittivity $\epsilon = 3.7\epsilon_0$ as

$$\sigma_s = \epsilon E = 6.67 \frac{nC}{cm^2}$$

calibrating the magnitude of the output signal to a charge density.

2.7.1 Volume Charge Density

The value for surface sheet charge calibrates the deconvolved charge distribution allowing one to plot the charge profile in real units of charge density, $\frac{nC}{cm^3}$. The FFT routine used returns a constant value of $\frac{\pi}{2}$ as the integral of the impulse signal deconvolved with itself. A charge distribution will be proportional to any the charge layer of thickness $v_s\delta_d t$ where $\delta_d t$ is the digitizing interval, equal to 5 ns for the recording scope used. The scaled output from the deconvolution is multiplied by

$$\frac{2\sigma_s v_s \delta_d t}{\pi} \ in \ \frac{nC}{cm^3}$$

at every point in the output data string. This scale factor is determined for each sample and accounts for all the parameters for a particular sample; including velocity of sound, thickness, and electrostriction coefficient. This is because the sheet charge, σ_s, which causes the impulse is presumed correct.

87

Deconvolved waveform
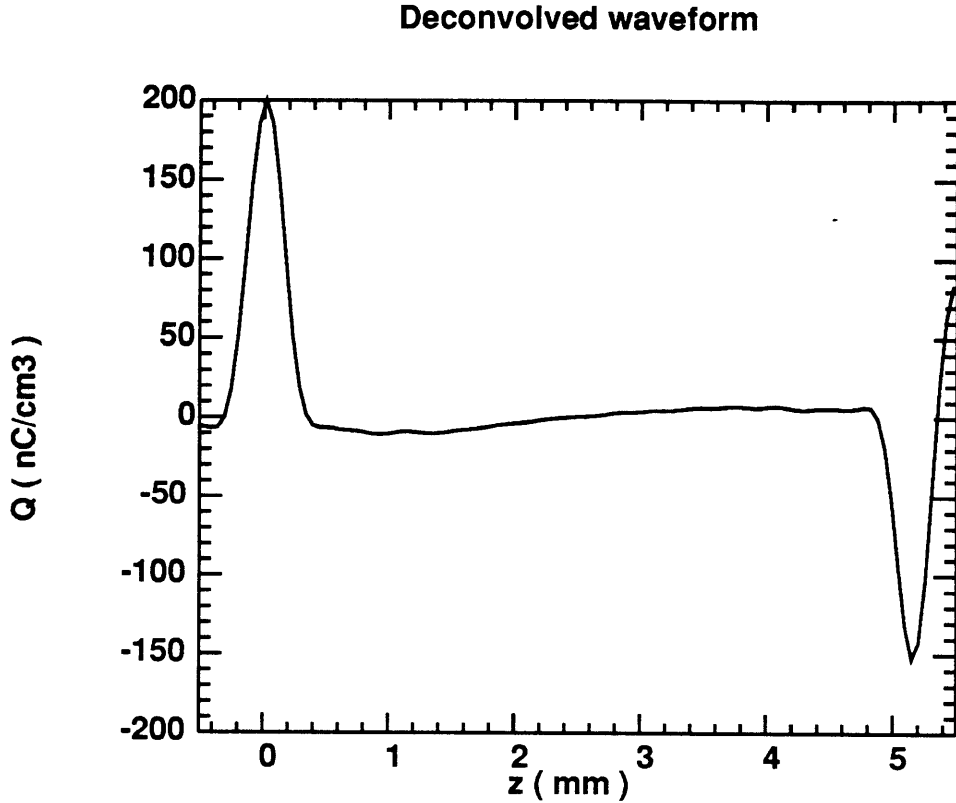
Figure 2.25: Deconvolved and filtered waveform, scaled to the selected impulse response. Area under pulse $Q_s = 6.67 \frac{nC}{cm^2}$.

2.7.2 Resolution Limit

The applied sheet charge gives a signal that is 120 ns wide, corresponding to 324 μm in the sample. One can say that the resolution is good to approximately half the full width at half maximum, giving a real spatial resolution in PMMA of 162 μm. The sensitivity is found from the signal to noise ratio of the output signal. Looking at Fig. 2.25, the central region zero charge shows a non-zero value within approximately 8 $\frac{nC}{cm^3}$. This makes an approximate value for the resolution product figure of merit defined in

section 1.1

$$R \approx 0.13 \frac{nC}{cm^2}$$

a far better value than any other acoustic technique.

2.7.3 Linearity

Throughout this discussion, the linearity of the material has been assumed. No signals may exceed the limits of linear stress-strain relations, or all the analysis is no longer valid. Starting with the yield stress for low density PE as an example, we find

$$T_{yield} = 700 \frac{N}{cm^2}$$

from *CRC Handbook of Chemistry and Physics* [35]. This may be compared to the stress induced by electrostatic forces. Consider a DC field much larger than any which will be performed in this study, $100 \frac{KV}{mm}$. The calculated surface stress for this field is

$$T_i = \frac{\epsilon}{d^2} V_{dc}^2 = 0.02 \frac{N}{cm^2}$$

assuming $\epsilon = 2.3\epsilon_0$. Which is approximately five orders of magnitude lower than the yield, justifying the assumption of acoustic linearity.

Furthermore, one can measure the peak stress due to the impulse charge layer shown in section 2.7. The peak voltage may be plotted with applied DC voltage to correlate the output signal strength verses a known sheet charge. This is shown in Fig. 2.26 for the same 5.28 *mm* thick PMMA sample shown in Fig. 2.24 with voltages from -20 to +20 KV across the sample.

The slope of the curve indicates the output signal with respect to surface sheet charge. A 10 *KV* DC voltage across the 5.28 *mm* thick sample of PMMA gives a peak output signal of -150 *mV*, corresponding to $6.67 \frac{nC}{cm^2}$.

89

Peak output signal
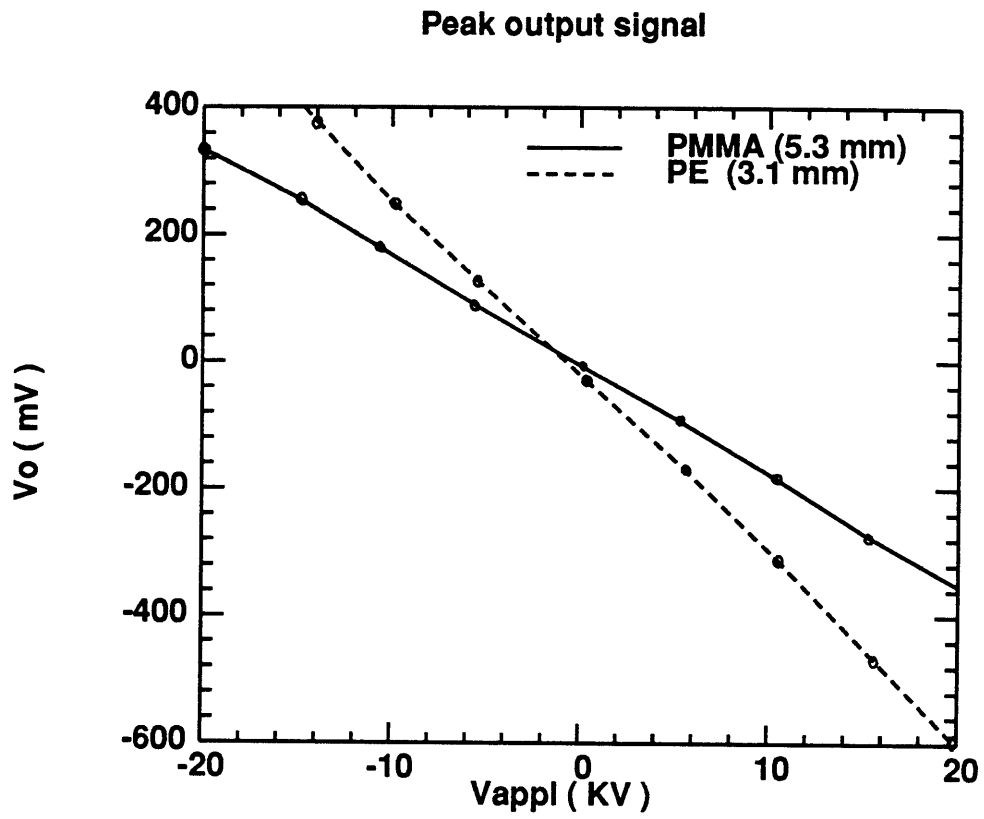
Figure 2.26: Peak detected signal verses applied DC voltage for a 5.28 mm PMMA sample (solid) and a 3.1 mm PE sample.

Thus, a sheet charge of value Q_s within the material will give an output voltage V_{oPeak}

$$V_{oPeak} = -22.5\frac{mVcm^2}{nC}Q_s$$

Although surface charges will be offset by the pulse-induced charge corresponding to $11mV$ at the output.

The next chapter will demonstrate the effectiveness of this technique for measuring bulk space charge distributions. Several samples which have undergone different thermal and electrical histories will be presented to show how the ESAW charge profiling method can be used as a powerful analysis tool for observing the effects of different stimuli.

Chapter 3

Static Charge Measurements

Evidence confirming the accuracy and reliability of ESAW measurements was provided in the previous chapter. Linearity and superposition were shown to apply for measuring sheet charges within uniformly unpoled samples. The measurement of bulk charge profiles from poled and electron irradiated samples will be demonstrated in this chapter. The bulk profiles have been determined by the method described in chapter 2 [15] which involves numerical deconvolution of the bulk acoustic response referenced to a known sheet charge imposed at the lower electrode interface. The general characteristics of electrically stresses samples poly(methylmethacrylate), PMMA, and polyethylene, PE, will be discussed.

Two methods of space charge generation in insulators will be examined: DC electrical poling and electron-beam implantation. Poling is the process of applying a constant DC voltage across an insulator at a raised temperature, allowing the material time to adjust to the electrical stress. E-beam implantation, on the other hand, is the process of accelerating electrons and allowing them to come to rest inside the material. DC poling can result in dipolar charge accumulation with or without the presence of unpaired

charge. Implantation forces a net negative charge due to the excess electron concentration.

At any time during the poling process, a sample can be tested with an ESAW measurement to profile the resulting charge inside the material. Given the poling field, temperature, and length of time the poling took place, a single measurement can give some indication of the processes which have taken place. The charge distribution will indicate whether the bias field resulted in bulk polarization, injection at an electrode interface, or some combination of the two.

The experiments were performed on PMMA and PE, each sample of which was sectioned from the same pellets to assure the properties were constant from one sample to the next. This removes the possibility of material processing conditions due to different stocks; although, variations may still occur across the same sheet. Since the area of the electrodes are much larger than the thickness, the internal fields can be considered perpendicular to the electrodes. All the effects will be essentially one-dimensional as the equipotentials are constrained to be parallel.

The PMMA samples were general purpose *Plexiglas-G* sheets manufactured by *Rohm&Haas* cut into squares measuring 2 to 3 inches on a side. The PE samples were sheets of cross linked cable material formed by *Conductor Products Corp., TX* from *Union Carbide* stock. Each sample had aluminum electrodes deposited by vacuum evaporation at MIT over a 1.25 *in* diameter on both sides. The electrodes were aligned to assure uniformity of fields during excitation and measurements.

Measurements were performed at room temperature after turning off the DC field, then removing the samples from the poling oven (see section 3.2.1).

Each sample was profiled under short circuit conditions using ESAW testing, giving the internal charge profile as well as the image charges at each surface. The magnitudes of the image charges at both the poling anode and cathode provide a self consistent check on the internal charge profile in the bulk. Interpretation of the values of surface charge will be discussed next, some static data will also be presented as well as preliminary interpretations of the data.

3.1 Surface Image Charge

Under short circuit testing conditions, images of internal charges are induced at the electrodes. The magnitudes of these surface sheet charges depend on the total charge density and position between the two electrodes. From the boundary conditions imposed by shorted electrodes, a differential element of charge $\rho(z)dz$ as seen in Fig. 3.1 is imaged on the electrode at $z = 0$

$$dQ_s(0) = - \left[1 - \frac{z}{d} \right] \rho(z)dz$$

where the contribution of charges closer to the electrode weighs more heavily on the surface charge [6].

The charges on the electrodes at $z = 0$ and at $z = d$ are found by integrating the charge density

$$Q_{s0} = Q_s(0) = - \int_{z=0}^{d} \rho(z)(1 - \frac{z}{d})dz \qquad (3.1)$$

and

$$Q_{sd} = Q_s(d) = - \int_{z=0}^{d} \rho(z)\frac{z}{d}dz \qquad (3.2)$$

A net charge between the electrodes will result in the two surface image

94

$-\left(1-\frac{z_i}{d}\right)\rho(z_i)dz$ dz $\rho(z)$ $-\left(\frac{z_i}{d}\right)\rho(z_i)\,dz$

z

0 z_i $\bar{z}$ d
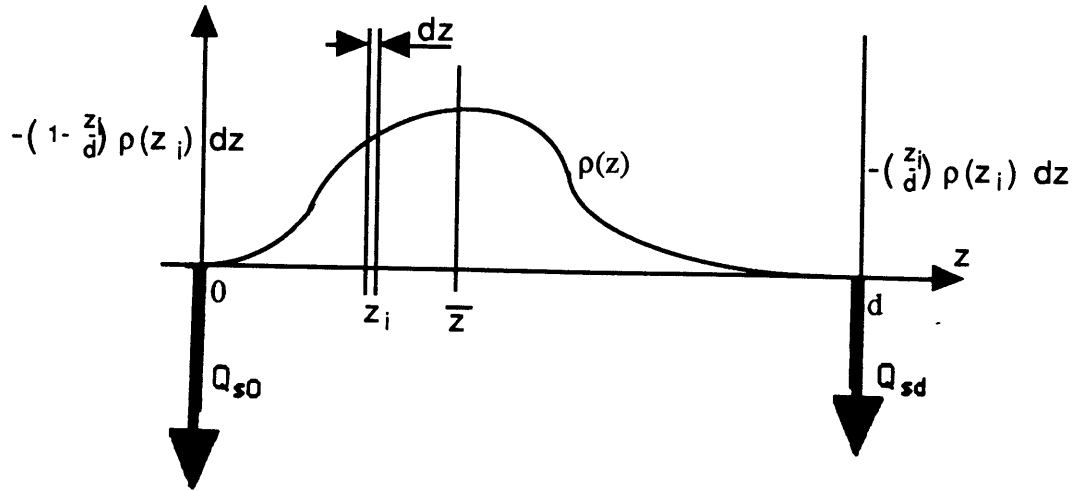
Q_{s0} Q_{sd}

Figure 3.1: Representation of the image on short circuited electrodes of a material containing a space charge distribution

charges summing to the negative integral of the total charge

$$Q_{s0} + Q_{sd} = -\int_0^d \rho(z)dz \tag{3.3}$$

the relative values of the two image charges depending on the distribution within the bulk. The first moment of the charge centroid $\bar{z}$ can be determined by knowing the relative sheet charges at the electrodes and the sample thickness

$$\frac{\bar{z}}{d} = 1 - \frac{Q_{s0}}{Q_{s0} + Q_{sd}} = \frac{Q_{sd}}{Q_{s0} + Q_{sd}} \tag{3.4}$$

as long as both sheet charges are of the same sign.

3.1.1 Determining Polarization

A poled sample with no net charge will have surface sheet charges equal in magnitude but opposite in sign. The absolute magnitude of the charge on either electrode is the net polarization (P_t), illustrated by reference to Gauss' law for electric field in a polarized material

$$\nabla \cdot (\epsilon E + P_t) = \rho_q(z) = 0 \tag{3.5}$$

95
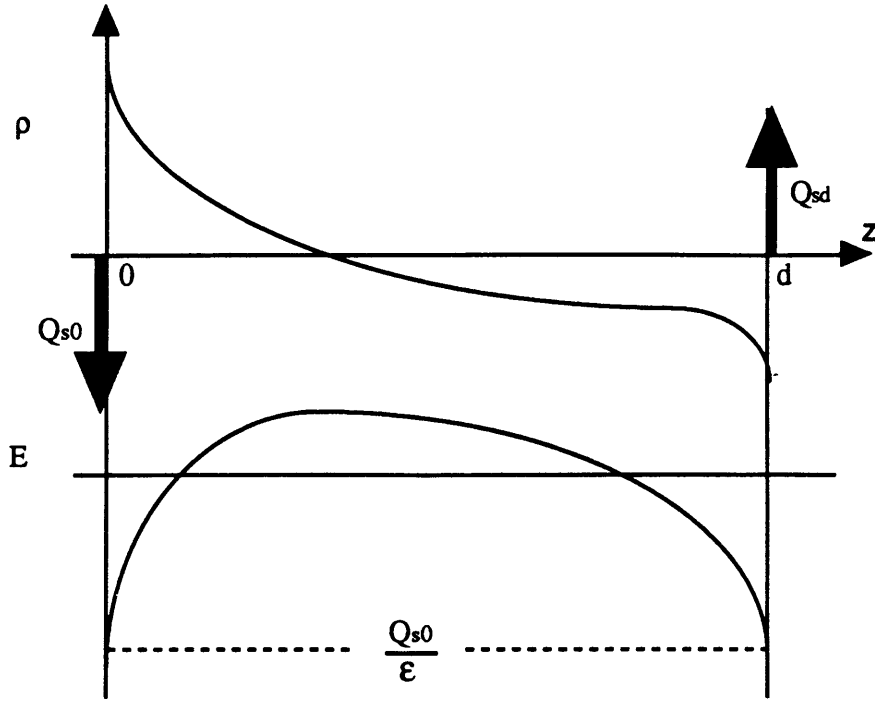
Figure 3.2: Asymmetric charge distribution profile with resulting E-field distribution and surface sheet charge

Imposing short circuit boundary conditions yields a surface E-field proportional to P_t at the electrode. Hence, the charge at either surface is equal in magnitude to the net polarization

$$|Q_{s0}| = |Q_{sd}| = Q_s = \epsilon_n \cdot E_{int} = P_t$$

for the E-field at the electrode interface E_{int} and ϵ_n is the net permittivity. Since the field discontinuity at each boundary is opposite in direction, the resulting sheet charge is opposite in sign and equal in magnitude regardless of how the charge is distributed. This is demonstrated in Fig. 3.2 where an asymmetric charge distribution is shown, along with its resulting E-field. Note that the integral of E-field across the sample must be zero for a sample with both electrodes shorted together.

The surface sheet charge density (per unit area) at the lower electrode

($z = 0$) is determined from the ESAW acoustic wave by the peak signal arriving after the $4.3\mu s$ coupling delay, as discussed in section 2.1. The time domain voltage of that initial signal peak is linearly dependent on the applied voltage as seen in Fig. 2.26. Therefore, an opposing external DC voltage may be applied to cancel that surface image charge. Knowing the thickness d, ϵ, and the voltage applied to cancel the surface charge, one can determine the short circuit image charge which lies at that interface

$$Q_s = \frac{\epsilon V_{cancel}}{d} \tag{3.6}$$

where V_{cancel} is the voltage applied to cancel out the surface charge.

When the bulk charge density is small, even too small to detect directly, the resulting surface charge may still be detectable since it is proportional to the integral of the charge across the sample. In a situation where a distributed charge is too small to be reliably detected, the resulting surface charges can be used to measure the net charge and polarization. This becomes important for certain poling tests where the charge distribution does not produce a signal significantly enough above the noise to permit a reliable measurement of the bulk distribution.

The next section will demonstrate some typical ESAW measurements of samples having undergone poling at various temperatures and fields. The calibrated charge profiles demonstrate where charges end up after reaching quasi-equilibrium within the time frame of the tests performed. Afterwards, the results of E-beam implant data will be shown.

3.2 Poling Experiments

Several samples of PMMA and PE were measured after having been poled by exposure to moderate fields of 0.4 to 5.0 $\frac{KV}{mm}$, at temperatures ranging

97
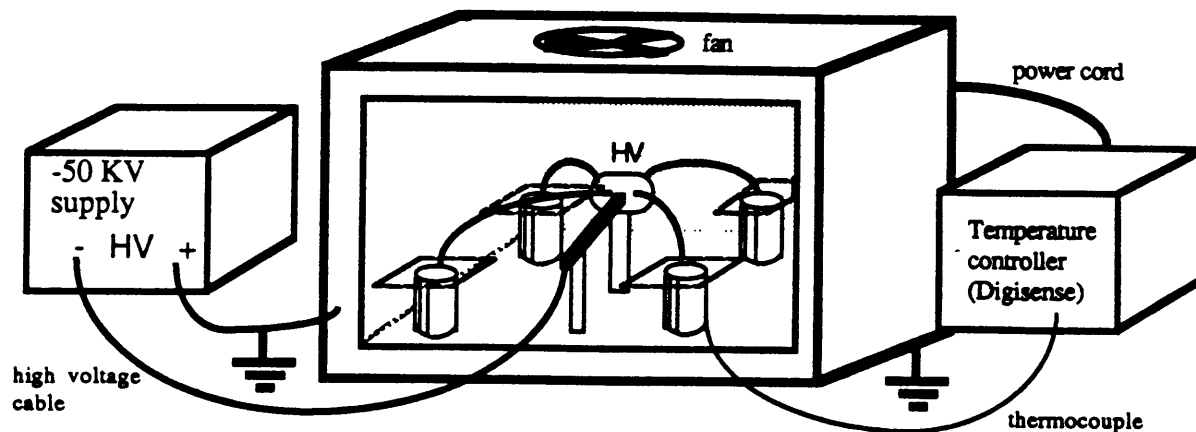
Figure 3.3: Convection oven with high voltage supply used for poling.

from room temperature to 90° C. All these samples have accumulated space charge distributions within their bulk; although, striking differences in the charge profiles suggest the presence of a variety of dominant space charge creation mechanisms.

This section will describe the poling procedure by presenting the apparatus and the materials, followed by a series of charge profiles of samples which have reached a nearly steady state charge distribution. Comparison of the profiles provides an indication of some of the physics involved. The next chapter will show the time resolved poling data in order to gain further physical insight.

3.2.1 Poling Oven

The apparatus used for poling was a simple convection oven connected to a *DigiSense* temperature controller. An aluminum plate with four raised electrodes was fashioned to fit within the oven to hold the samples under bias at the constant elevated temperature. A schematic diagram for this

equipment setup is shown in Fig. 3.3. A high voltage supply, capable of providing 0 to -50 KV, is connected to any or all of the four top aluminum electrodes via the center electrode. The bottom plate and all four lower electrodes are connected to ground.

Heated air surrounding the samples is circulated by a fan through heating coils in the oven. A thermocouple bolted to the supporting aluminum plate, holding the four aluminum stands, provides the temperature sense input to the controller.

Samples are inserted and removed from the oven and tested at room temperature. The samples are cooled down quickly with a cool air blower to *freeze in* the accumulated space charge distribution. Time is still needed for the temperature to equilibrate in the oven and in the sample. There is, consequently, an error associated with the poling times assigned to measurements at temperatures greater than 50° C. The samples are reinserted into a preheated oven to speed up the heating transient in order to minimize the poling time error.

The voltage is maintained across the sample during the thermal transition periods so the behavior is predominantly determined by the time at the peak temperature. The error in poling time has been determined by measuring the fall time of the oven. The worst case of cooling the oven from 90° C to room temperature takes approximately 5 *minutes*. However, if one assumes the poling effects are thermally activated, the error can be found by the time to cool below $\approx$ 70° C, taking less than 3 *min*, which will be assumed for the error associated with each time interval.

After exposure to the raised temperature and electric field, the samples were cooled down to room temperature and tested in the ESAW apparatus.

Raw time data, showing the main characteristics of the charge profile, is viewed immediately at the computer terminal. The signal is then processed to produce a calibrated charge profile using an appropriate impulse response.

Data from PMMA and PE samples will be presented. Afterwards, some prominent characteristics common to poled samples in general will be discussed. The time evolution of the charges are in the following chapter where transport mechanisms will be considered. The remainder of this chapter will be concerned with samples after having been poled under different conditions of field and temperature.

Space charge will be plotted in units of $\frac{nC}{cm^3}$ versus z in mm. The electrode boundaries are within the resolution width of the left and right borders of the plots. This resolution limit is approximately 0.2 mm (shown in section 2.7) and will be the spacing of the minor ticks. All the waveforms shown in this and the following chapters are calibrated deconvolved waveforms.

3.2.2 PMMA Data

The *Plexiglas* samples were 5.28 mm thick and cut from the same sheet stock to ensure that the material properties were reasonably similar from one sample to the next. The only treatment performed on the samples was a methanol wipe before evaporated aluminum electrodes were applied. Electrode dimensions were defined in the chamber by a shadow mask in the evaporation path.

Two series of tests were performed; one at constant poling field and different temperatures, the other at constant temperature and different poling fields. The constant voltage used for the first set of tests was 5 KV (corresponding to field strengths of 0.95 $\frac{KV}{mm}$), for a sequence at 40, 50 and 90° C. Then, at 50° C, two further tests were performed at 2 and 15 KV. This

100

section will present profiles obtained after a nearly steady state condition was established within the time frame of a few days for most of the experiments. The time resolved progression of the charge accumulation profiles will be shown in the next chapter.

Constant Poling Voltage

The charge distribution profiles for 40 and 50° C test are shown in Figs. 3.4 and 3.5 with the anode at $z = 0$ in the solid traces, and the cathode at $z = 0$ in the dashed traces. These curves exemplify the nearly steady state charge distributions, as will be described in section 4.1.1, obtained after 11 days for the 40° C sample and after 5 days for the 50° C sample.

The resolution of these curves is limited by the signal to noise ratio, as determined in the previous chapter. The minimum detectable sheet charge is the resolution limit $R = 0.13 \frac{nC}{cm^2}$ for the system used. Considering a minimum spatial width of 0.165 mm, the error associated with the charge concentration is $\pm 8 \frac{nC}{cm^3}$.

The sheet charges residing at the two electrodes are due to unpaired bulk charge and net polarization, P_t, from the electrical excitation. These image charges have been found to be opposite in sign, but not equal in magnitude. The samples are initially charge neutral; therefore, the resulting unpaired charge must be due to an imbalance of injection from one or both of the electrodes. Adding the surface charges residing at the anode and cathode interfaces gives the negative of the net charge across the bulk, as demonstrated in section 3.1. The net internal charge has been calculated for these samples: at 40° C, the net charge is $-1.1 \frac{nC}{cm^2}$ and at 50° C, the net charge is $-4.2 \frac{nC}{cm^2}$ as determined from the peak signal of the first arrival

101
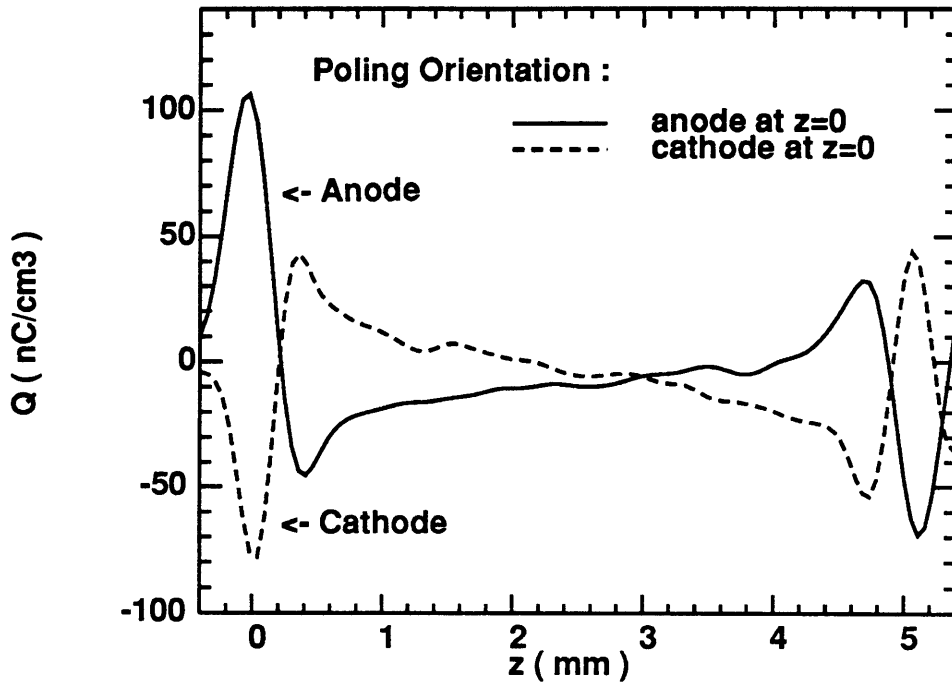
Figure 3.4: Space charge distribution from 5 KV poling of PMMA at 40° C for 270 hours with the (solid) anode side and (dashed) cathode side at $z = 0$.

PMMA
Poled at 50 C with 5 KV for 5 days
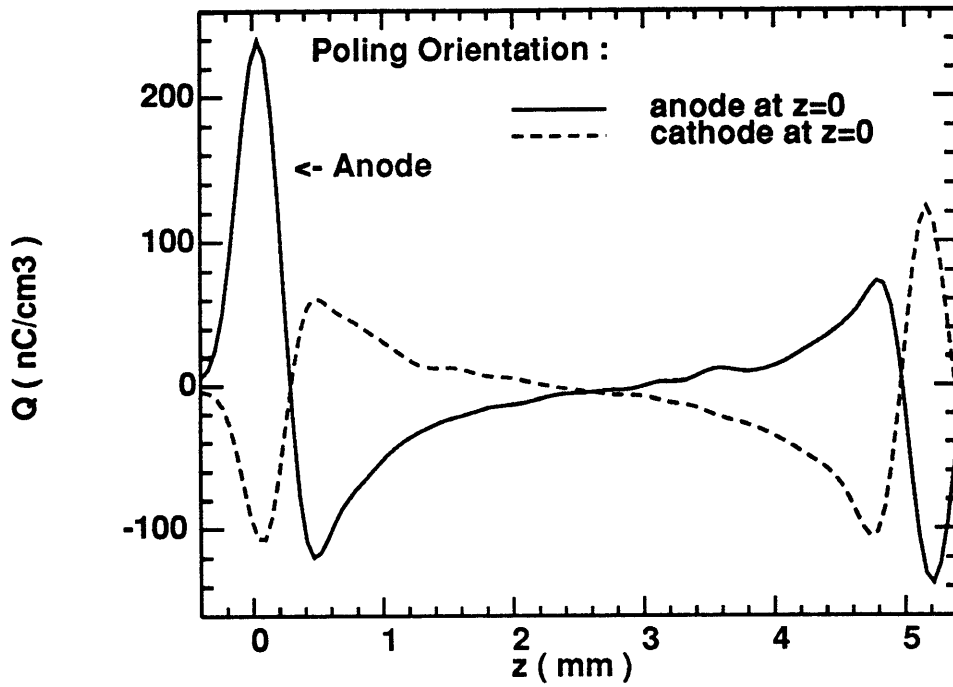
Figure 3.5: Space charge distribution from 5 KV poling of PMMA at 50° C for 120 hours.

103

impulse.

Narrow Homocharge Layers

Similarities in the central regions of the two curves indicate that differences between them are most profound nearest the electrodes. The central regions of the samples shown in Figs. 3.4 and 3.5 have a smoothly varying distribution of space charge from near zero in the middle, increasing towards the electrodes. Net negative charge, evidenced by the difference in surface charges at the anode and cathode, appears to be an effect of injection at the cathode. The symmetric charge distribution suggests that there is no detectable bulk transport of the injected charge through the sample, leaving the homocharge within a narrow layer beneath the electrode.

A large net charge density is seen at 90° C as shown in Fig 3.6. This sample has been placed under 5 KV bias for 6 hours and accumulated a large negative charge near the anode. Since both surface sheet charges are positive, a net charge moment may be found from the ratio of either peak to the sum. The result is a total embedded charge $Q_t = 22\frac{nC}{cm^2}$ and $\bar{z} = 0.44mm$.

Field and Voltage Evaluation

The charge density across the sample is sufficiently above the resolution limit, allowing direct integration of the charge profile to provide a meaningful field distribution. This is demonstrated by the solid curve of Fig. 3.7, where the charge profile of Fig. 3.6 is numerically integrated with z to give the E-field distribution. The dashed line is the potential distribution across the same sample found by negative integration of the E-field. Both the potential

104

PMMA
Poled at 90 C with 5 KV for 6 hours
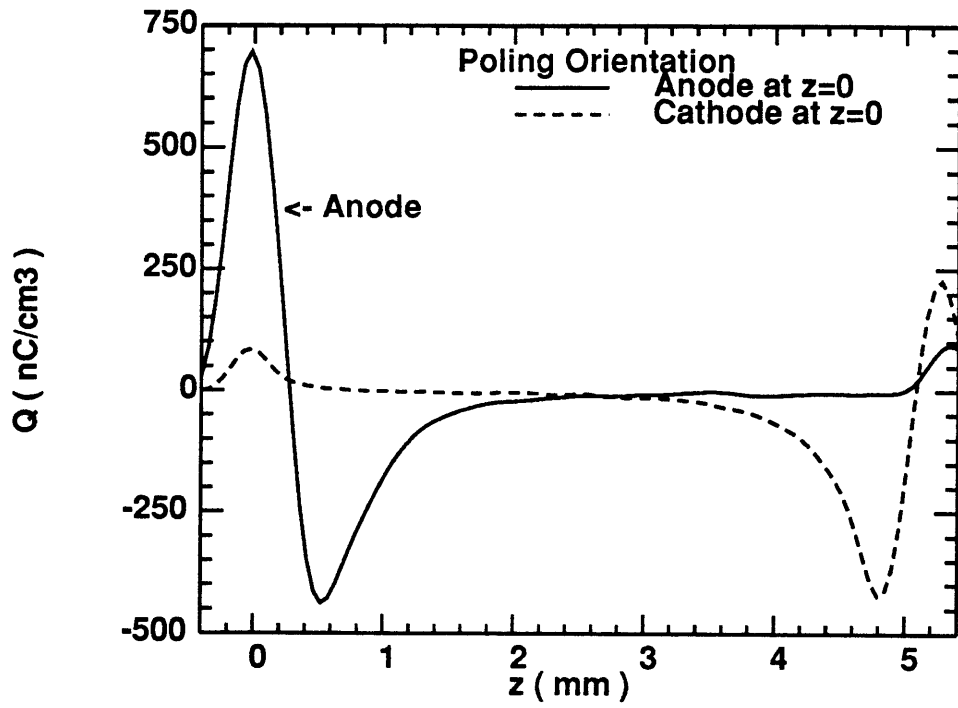
Figure 3.6: Space charge distribution from 5 KV poling of PMMA at 90° C for 6 hours.

105

PMMA
Poled at 90 C with 5 KV for 6 hours
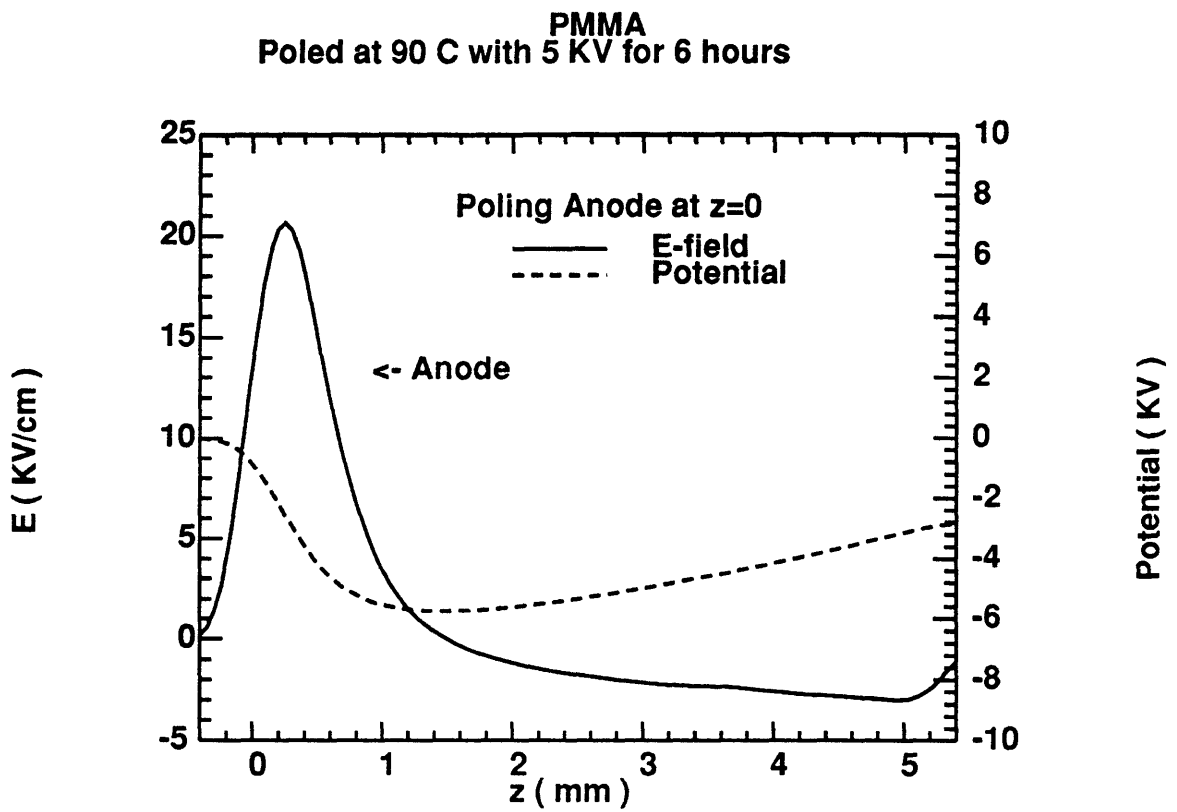
Figure 3.7: E-field (solid) normalized to voltage across the sample and Potential (dashed) distributions from Fig. 3.6 found by integration of the charge density.

and the field are assumed zero before the start of the front peak because the anode is at ground.

Neither the field or the potential end up at zero on the cathode side. This is primarily attributed to the reduced signal of the second interface. This peak may be reduced by as much as $\frac{1}{8}$ the actual charge because of the acoustic mis-match between the plastic and the upper-electrode (see section 2.6.2). Integration over the actual peak would bring these curves closer to zero at the cathode, $z = d$.

Some of this discrepancy in the cathode field and potential can also be due to the error in the detection apparatus. As seen in section 2.7, the uncertainty in charge resolution is $\Delta\rho = 8\frac{nC}{cm^3}$. If this were a constant error, for a worst case assumption, the resulting voltage difference would be

$$\Delta V = \frac{\Delta\rho d^2}{2\epsilon} = 3.4KV$$

which is larger than the observed voltage offset (dotted curve). Between both sources of error, the potential distribution shows that the E-field curve is in agreement with its expected shape, putting a large degree of confidence on the absolute values for the charge profile.

One observation that can be made from this curve is of the field just beneath the poling cathode. This is close to the field seen across the sample under bias of $5KV$, suggesting that after the 6 *hours* of poling, the field at the cathode is nearly zero while under bias. This is defined as the *virtual cathode* condition of space charge limited current [41]. Therefore, it can be seen that the E-field profiles can distinguish the limiting conduction process of a sample in a steady state condition. This result will be compared with current versus voltage tests in chapter 5 to draw more insight from the ESAW data.

107

PMMA
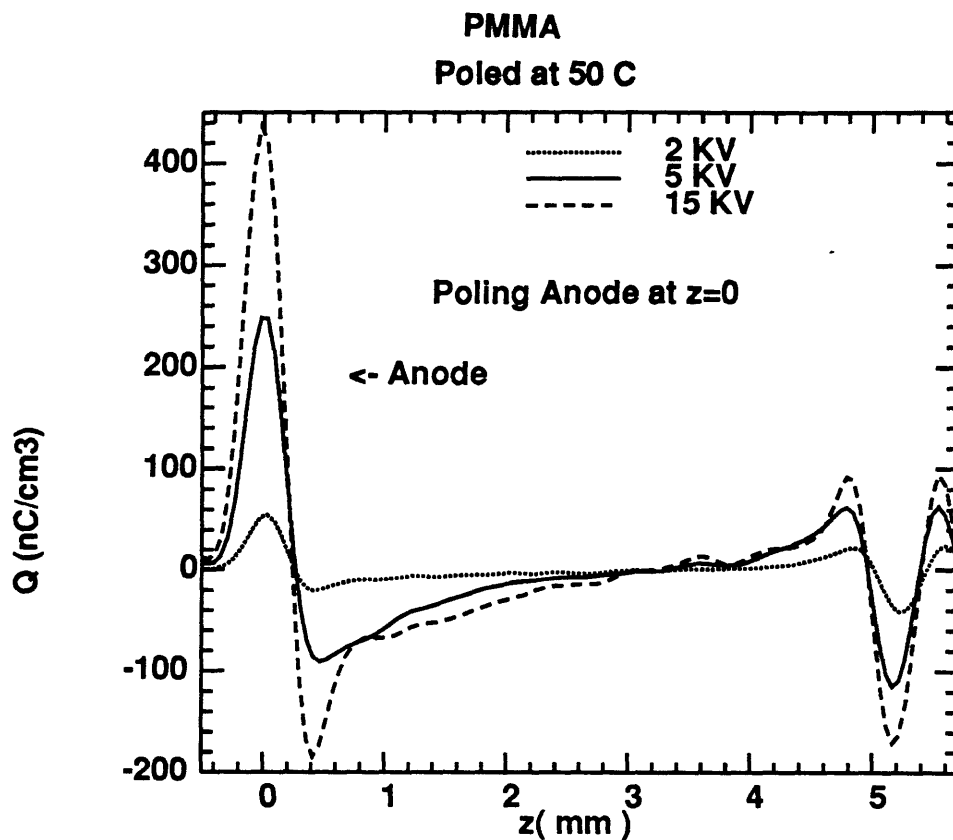
Poled at 50 C

Figure 3.8: Resulting space charge distribution from 50° C poling at 2 (dotted), 5 (solid), and 15 KV (dashed) for several days.

Constant Poling Temperature

Three samples were poled at 50° C for several days, with different applied fields: 2, 5 and 15 KV. These profiles are shown in Fig. 3.8. The Anode side is at $z = 0$, so these profiles illustrate heterocharge buildup within the sample bulk. This set of data was recorded after 41 *hours* for the 5 and 15 KV samples, but after 67 *hours* for the 2 KV sample. In these figures, the borders have been extended to show the total response to the sheet charge at the electrodes.

These profiles will be shown, in the next chapter, to have reached a nearly equilibrium condition. At the time the profiles were obtained, they have settled out to approximately steady state charge distributions where bulk polarization has reached an equilibrium within the time frame of a few days. One interesting characteristic of this set of data is the lack of proportionality between the surface charge and applied field. The surface sheet charge is found by the area under the curve of the initial peak around $z = 0$. The $z = 0$ peak of the 2 KV sample is less than $\frac{2}{5}$ the 5 KV peak, which is *more* than $\frac{1}{3}$ the signal from the 15 KV poled sample.

The data taken at $50°C$ is contrasted with a series of samples poled at $20°$ C, shown in Fig. 3.9 [1]. In these samples, peak charge densities are almost perfectly proportional to the applied field. These profiles show surface image charges that increase directly with field and have symmetric internal charge profiles about the center of the sample. This smoothly varying internal charge distribution is seen to be characteristic of many samples tested.

There appears to be a significant negative internal charge adjacent to the *positive* poling electrode (anode), changing to positive charge at the negative side (cathode). This internal *polarization* was consistently found at temperatures lower than 90° C for PMMA. The PMMA samples have accumulated *heterocharge* [38], defined as oppositely charged carriers accumulating near their respective electrodes. The 90° C sample has only accumulated heterocharge near the anode, while homocharge is seen near the cathode.

A schematic of the polarization is seen in Fig. 3.10 for two typical profiles. The figure in (a) shows a sample with heterocharge accumulation distributed across the bulk. A small amount of homocharge injection is illustrated as

---

[1]This series of data was taken from PMMA samples which were stressed at room temperature for a separate project by Dr. Chatham Cooke [39]

PMMA
Poled at 20 C for 60 days
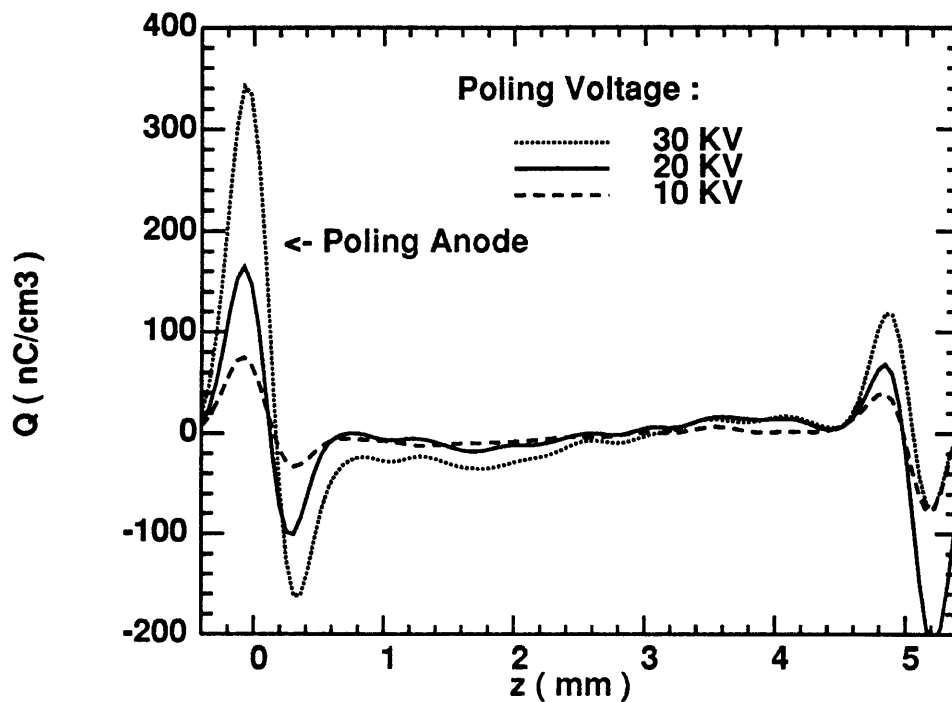
Figure 3.9: Resulting space charge distribution from 20° C poling at 30 (dotted), 20 (solid), and 10 KV (dashed) for 2 months.

Typical PMMA Sample T < 90° C

a)

Surface image charge

+ injected homo-charge

+ Poled Charge

Poling **Anode**

Poling **Cathode**

- Poled Charge

- injected homo-charge

(Injection Limited)

Surface image charge

Typical PE Sample T < 60° C

b)

Surface image charge

+ injected homo-charge

Surface image charge

+ Poled Charge

Poling **Anode**

Poling **Cathode**

(Space Charge Limited)

- Poled Charge

- injected homo-charge

Figure 3.10: a) Heterocharge accumulation, typically seen in PMMA samples poled at low temperatures and b) Homocharge accumulation with significant electron injection from the cathode, typical for PE samples.

111

the narrow regions in the immediate vicinity of the electrodes. This is the presumed interpretation of the data seen for the PMMA samples poled at $T < 90°$ C. The second part of this figure illustrates how injection can dominate the poling characteristic as will be seen to typically occur in PE in the following section.

To see how much the front peak affects the resolution of the embedded charge profile near the surface, an external voltage may be applied across the sample to apply an equal but opposite sheet charge at the electrode. The 30 KV poled sample of Fig. 3.9 has been tested with the anode at $z = 0$ while a DC voltage of 20 KV was applied across the 5.28 mm thick sample to bring that peak to zero. This is shown in Fig. 3.11 where the resulting profile (solid) shows the internal charge due to room temperature poling. A comparison of the two distributions of Fig. 3.11 also places a check on the system response. The acoustic impulse from the front peak does not obscure the detection of the internal distribution, witnessed by close fit in the central region.

The area between the two profiles represents the sheet charge at the electrode which is due to the image from the internal charge. This charge can be brought to zero with the application of an externally applied voltage. Charges that are bound to the material bulk can not be reduced with the application of an external bias since this voltage produces a Laplacian field. Therefore, the internal charge profile with bias follows the profile of the same sample under short circuit conditions. The discrepancy of the areas between the curves at $z = 0$ and $z = d$ is due to the acoustic response from the upper electrode (see section 2.6.2). The applied voltage creates a charge layer at the brass-PMMA interface, assuring that only a small fraction of

112

PMMA
Poled at 20 C for 60 days at 30 KV
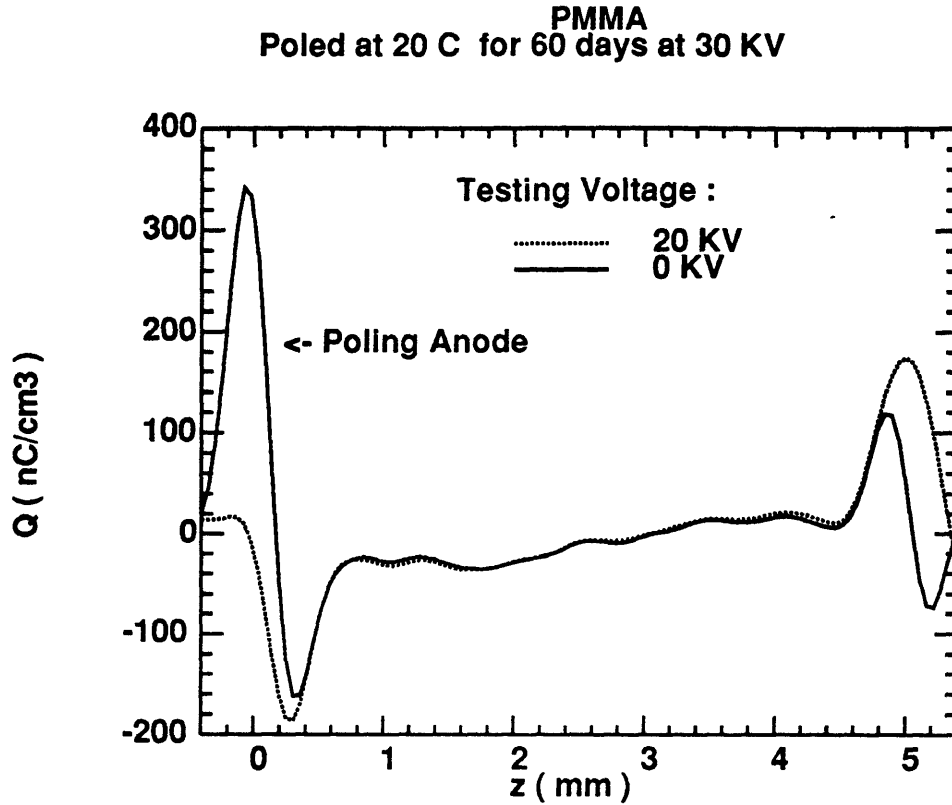
Figure 3.11: Resulting space charge distribution from 20° C poling at 30 KV for 2 months (dotted) and with 20 KV applied to cancel the first peak (solid).

the induced stress propagates to the detector.

The net polarization, P_t, is measured by this method. The surface sheet charge which exactly cancels the front peak is determined by the voltage applied across the sample from the upper electrode. A positive voltage applied to the upper electrode will produce a negative sheet charge at the lower electrode boundary. The charge layer in this example is positive and is canceled with a negative charge, resulting from a positive voltage on the upper electrode at $z = d$. The polarization obtained this way is positive and

found to be

$$P_t = Q_{s0} = \epsilon \frac{V}{d} \approx +12 \frac{nC}{cm^2}$$

assuming there is no net unpaired charge.

3.2.3 PE Data

It has been found that PE space charge characteristics vary from one supplier to the next [38], which limits the ability to generalize about the material properties based on the analysis of a single type of stock. In this study, all the tests were performed on samples prepared from the same 3.1 mm thick sheet stock so the characteristics can be assumed constant from one sample to the next. This section will first discuss the effects of two samples having been exposed to the same field at different temperatures and then the effects of various fields applied at the same temperature will be compared.

Constant Poling Field

The following two plots show the results of different PE samples poled with with 20 KV applied: one at 20° C, shown in Fig. 3.12 and the other at 60° C shown in Fig. 3.13. Injection is apparent in both samples, as seen by comparison with the proposed interpretation of Fig. 3.10b), where homocharge is in the vicinity of the electrode boundaries. Both the anode and cathode sides are shown at the lower electrode ($z = 0$) to demonstrate the homocharge accumulation.

Near the center of the 20° C profile, heterocharge is apparent, similar to the low temperature PMMA samples. This effect is most apparent by the inverse slope of the profiles at the center. With the anode at $z = 0$, the low temperature sample has a *negative* slope near the center while the

PE
Poled at 20 C for 35 days with 20 KV
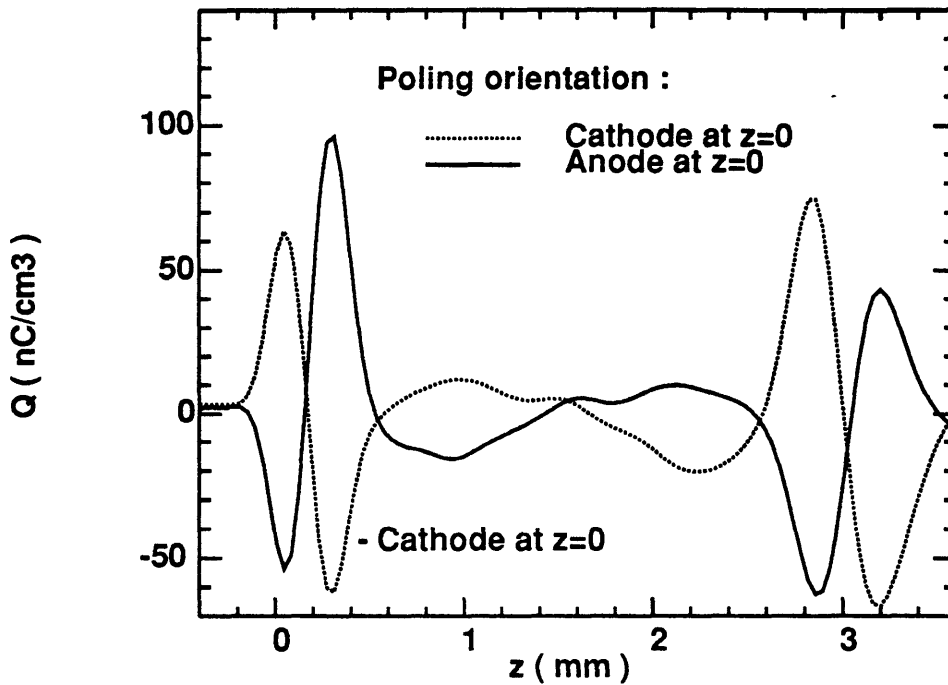
Figure 3.12: Resulting space charge distribution from 20° C poling at 20 KV for 35 *days* with the anode at $z = 0$ (solid) and cathode at $z = 0$ (dashed).

higher temperature sample has a positive slope. Also, the 60° C sample has a net negative charge distributed across most of the sample, indicative of bulk transport following asymmetric injection.

Looking at the pair of curves shown in Fig. 3.12, the actual profile near both electrodes becomes apparent. The two curves cross at a transition from charge of one sign to the other. This demonstrates the variety of effects taking place under these conditions. The surface sheet charges are approximately equal, while the layers immediately next to the electrodes are opposite. This figure also shows polarization deep in the bulk. Both
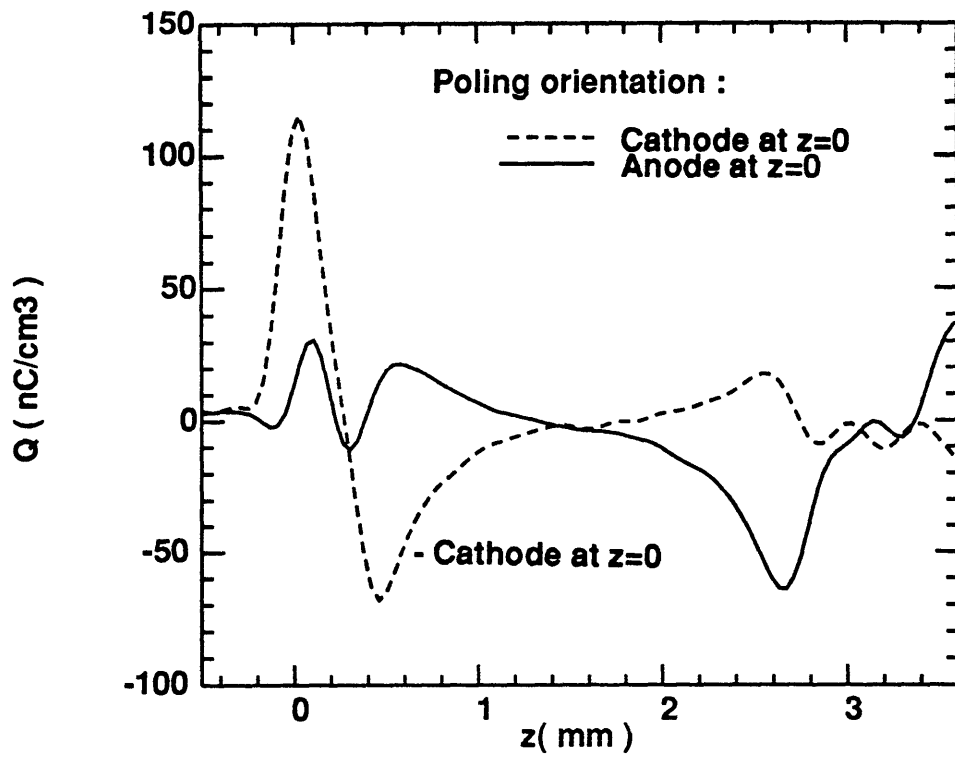
Figure 3.13: Space charge distribution from 60° C poling at 20 KV for 20 *minutes* with the anode at $z = 0$ (solid) and cathode at $z = 0$ (dashed).

polarization and electrode injection occurred in this sample; however, there is little macroscopic transport of the injected charge.

The dashed curve is the one with the cathode side *down* at $z = 0$, and it has a positive sheet charge with a negative charge concentration immediately beneath the electrode. The opposite is true for the anode side. Since positive charge remains beneath the positive poling electrode, producing a negative surface sheet charge, the open circuit voltage across this sample will be opposite in sign to the applied voltage. This will give a negative polarization, and results from *homocharge* injection being the dominant charging mechanism.

Evidence for injection is observed near the poling cathode at 60° C as seen in the short circuit profile, of Fig. 3.13, after 20 *minutes* of poling. The surface charge at the anode and at the cathode are indicative of the induced image charges. The sum of the signals near $z = 0$ for the two cases indicate the presence of a net *positive* image charge residing at both the anode and cathode; Therefore, a net *negative* charge resides within the sample.

The anode characteristic is notable. A small negative *bump* is seen at about $z = 0$, followed by a larger positive signal. Just beneath that within the sample lies an abrupt negative peak. This is similar to the low temperature sample, indicating a narrow layer of heterocharge (negative) in the vicinity of the anode. From these two curves, one can conclude that charge transport is enhanced at higher temperatures in PE.

Constant Poling Temperature

Three samples were poled at room temperature for 35 days at three different fields. The resulting space charge distributions are shown in Fig. 3.14 under

117
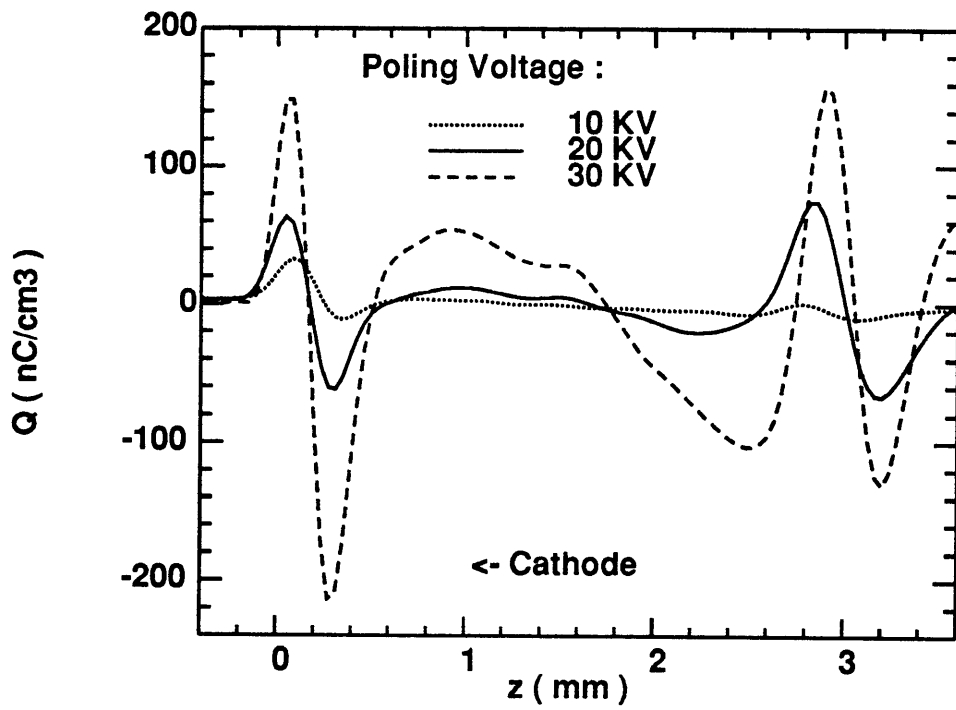
Figure 3.14: Space charge distribution from 20° C poling at 10, 20 and 30 *KV* for 35 *days* with the cathode at $z = 0$.

PE
Poled at 20 C for 35 days
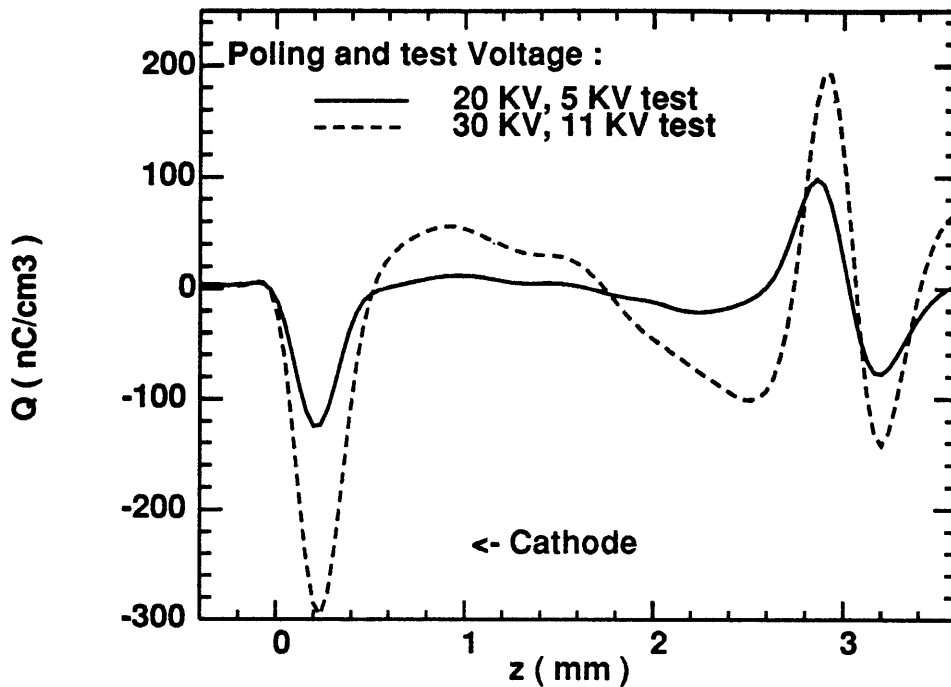
Figure 3.15: Space charge distribution from 20° C poling at 20 and 30 KV for 35 *days* with the front peak canceled.

short circuit conditions with the cathode side down at $z = 0$. What is obvious from these curves is the central polarization (heterocharge) from the 30 KV sample is more than 3 *times* that of the 20 KV sample. Homocharge resulting from injection at the higher field excitation is more than twice that of the lower one, even though the field is only $\frac{3}{2}$ as large. Similarly, the 10 KV sample has no apparent bulk characteristics; however, a small homocharge is observed.

The curves of Fig. 3.15 are the samples poled at 20° C with 20 and 30 KV. In this figure, the surface image charges are canceled during the

119

acoustic measurement of the two curves shown in Fig. 3.14. These samples used 5 and 11 KV to cancel that charge in order to obtain the true bulk charge figure. The result is a true indication of the space charge profile within the samples without being obscured by the surface charge.

The net poled charge can now be calculated from these samples in the same way as for the PMMA sample in the previous section and as defined in section 3.1.1. The surface image charges in these PE samples are opposite to the applied poling field. Thus, the polarizations are *negative* in sign. The values have been calculated for the 20 and 30 KV samples after room temperature poling for two months

$$P_t(20KV) = -3.4\frac{nC}{cm^2} \quad \text{and} \quad P_t(30KV) = -7.4\frac{nC}{cm^2}$$

3.2.4 Summary

Two general processes have been observed near the electrodes; polarization and injection. The former results in *heterocharge* or opposite space charge near the electrode while the latter yields *homocharge*. Both processes occur simultaneously; however, one may tend to dominate for a given temperature and perhaps electrode metal. At room temperature, the charge dynamics are slow enough to easily allow the few minutes needed to perform the ESAW profiling experiments.

Evidence for heterocharge in a sample is surface sheet charge at zero volts whose sign is the same as that of the applied poling field. This would have the effect of enhancing the field near the electrodes during poling. Charge that accumulates near the surface modifies the interfacial E-field until injection begins to counteract this effect. At the point of significant homocharge injection, the net accumulation slows down, or may reverse as an

120

equilibrium becomes established. PMMA consistently exhibits heterocharge accumulation near its electrodes reducing the field in the center, enhancing the field at the electrodes.

Injected homocharge charge is evidenced by near surface charge having the same sign as the poling voltage, resulting in a zero-volt surface charge *opposite* to the poling voltage. Homocharge reduces the E-field at the electrode while the field is applied, increasing the field within the bulk under constant voltage boundary conditions. As homocharge builds up beneath the electrode the surface field causing the transport is reduced at the electrodes while the internal field is increased. Enhanced bulk field increases the internal polarization of charges which would lead to heterocharge accumulation until an equilibrium between these two processes is reached.

Identifying two dependent processes of charge accumulation becomes apparent. The first is *polarization* whereby internal bulk charge redistributes itself within the sample as a zero-net charge process. The other, *transport*, is the means of adding or subtracting charge through the electrodes. Comments as to the mechanisms associated with these processes will be made after the dynamics have also been shown in the next chapter.

The limits of analyzing the charge profiles from the ESAW experiments have been demonstrated for DC poled samples and it has been shown that reliable profiles are obtained. Next, results from E-beam implanted PMMA samples will be presented. They provide a further check on the measurement system because they provide a characterized distribution profile.
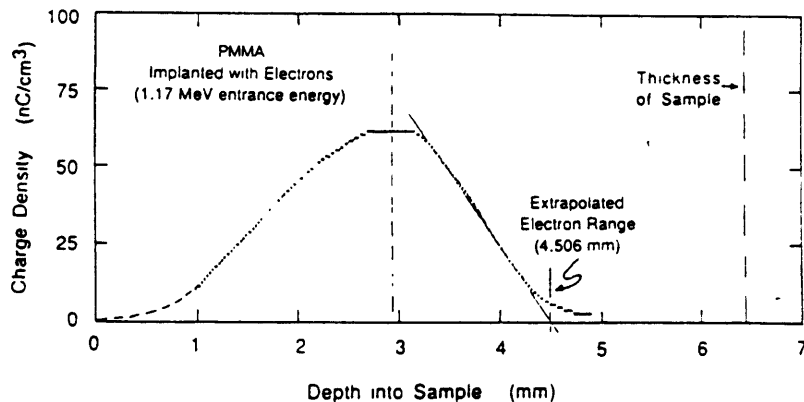
Figure 3.16: Measured volume charge after electron implantation [40]

3.3   E-beam Implantation

The apparatus used to inject electrons into the samples was a 3 *MV* Van
de Graff accelerator at the *High Voltage Research Laboratory* at MIT. The
dose and energy of the electron beam can be controlled to implant electrons
at depths up to about 1 *cm* in PMMA. The resulting profiles of implanted
charges have been analyzed using the ESAW apparatus[2].

Extrapolated projected ranges of several implanted samples were com-
pared to data and published by National Bureau of Standards (NBS). This
data was determined by implantation into layers of material. The individual
layers of known thicknesses were then measured for charge to provide a dis-
tribution profile. The NBS data has been compared to an electron charge
profile in PMMA measured with ESAW is shown in Fig. 3.16 [40]. The
measured range, 4.51 ± 0.05 *mm*, compares favorably to the expected range
of 4.58 ± 0.17 *mm*, and is well within the resolution limit of the apparatus.

The expected range in PE and PMMA, using the layered material ap-
proach, was tabulated [40] from an NBS circular compiled by Berger and

---

[2]Published in IEEE Conference on Electrical Insulation and Dielectric Phenomena
(CEIDP) 1989 Annual Report [40]
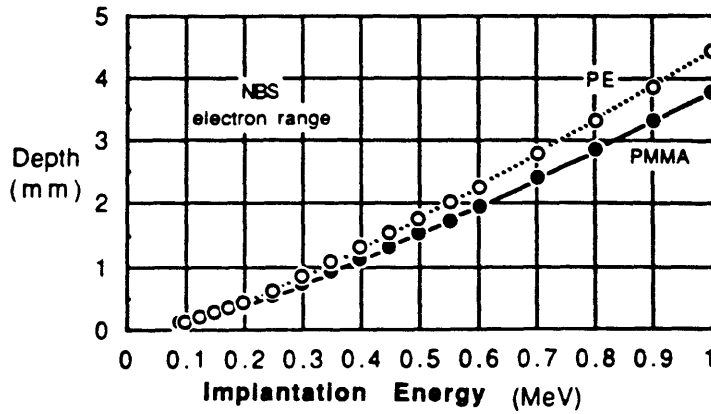
Figure 3.17: Electron range in PMMA and PE [40]

Seltz [3] and is shown in Fig. 3.17. The smallest reliable energy the accelerator can produce is approximately 0.6 MeV, so an energy of 0.64 MeV was chosen to produce a narrow implanted charge profile.

A low energy implant was performed in a 5.28 mm thick PMMA sample to keep all the charge near the surface. The chosen implant energy has a maximum extrapolated range of 2.2 mm as seen from Fig. 3.17. The profile should result in the same basic shape as that of Fig. 3.16, with the centroid at about $\frac{2}{3}$ the projected range.

The maximum voltage which can be reliably applied is 20 KV, so the dose was selected to allow the charge to be imaged on the opposite surface with this voltage. Consequently, the total charge needed depends on the centroid position z_c and voltage

$$Q_t = \epsilon \frac{V_{appl}}{d - z_c}$$

where V_{appl} is the 20 KV applied to image the charge on the opposite side.

---

[3]Data from NBS circular No. NBSIR 82-2550, *Stopping Powers and Ranges of Electrons and Positrons*, 1982

123

Assuming $z_c \approx 1\ mm$ deep

$$Q_t = 15.3\ \frac{nC}{cm^2}$$

The actual dose was chosen a little higher to allow for error in the centroid as well as the possibility of room temperature charge relaxation.

The samples were profiled under short circuit conditions twice, once with the implanted side *up* and once with that side *down*. The two curves are shown in Fig. 3.18 where they are compared to illustrate the measurement accuracy, as in the previous section. From these plots, the projected range is determined by extrapolating the profile tail on the bulk side down to the zero charge line. This line crosses at $\approx 2.15\ mm$ from the *down* curve. This value agrees closely with the expected range of from Fig. 3.17.

Normalized E-field and potential plot are shown in Fig. 3.19 where the field is multiplied by the sample thickness. This allows one to visualize how much voltage across the sample corresponds to that field. The maximum field in the shorted sample is 20 KV, meaning that a 20 KV DC voltage across the sample will impose a zero E-field at the front electrode. Integrating the field gives the negative potential with respect to $z = 0$ in order to check the boundary conditions. The voltage at the other surface $z = d$ should agree with the applied voltage if the field and charge profiles are consistent.

In both tests, the voltage agrees well with this known voltage. The dashed line is the potential through the sample with short circuit boundaries and integrates to nearly 0 KV. Similarly, the double dotted line is the potential of the sample with 20 KV applied from the opposite side ($z = d$ to $z = 0$), and this curve goes to just over 20 KV as expected. Consequently, the E-field curves and the charge distributions are self-consistent.

124

PMMA
E-Beam Implant Profile
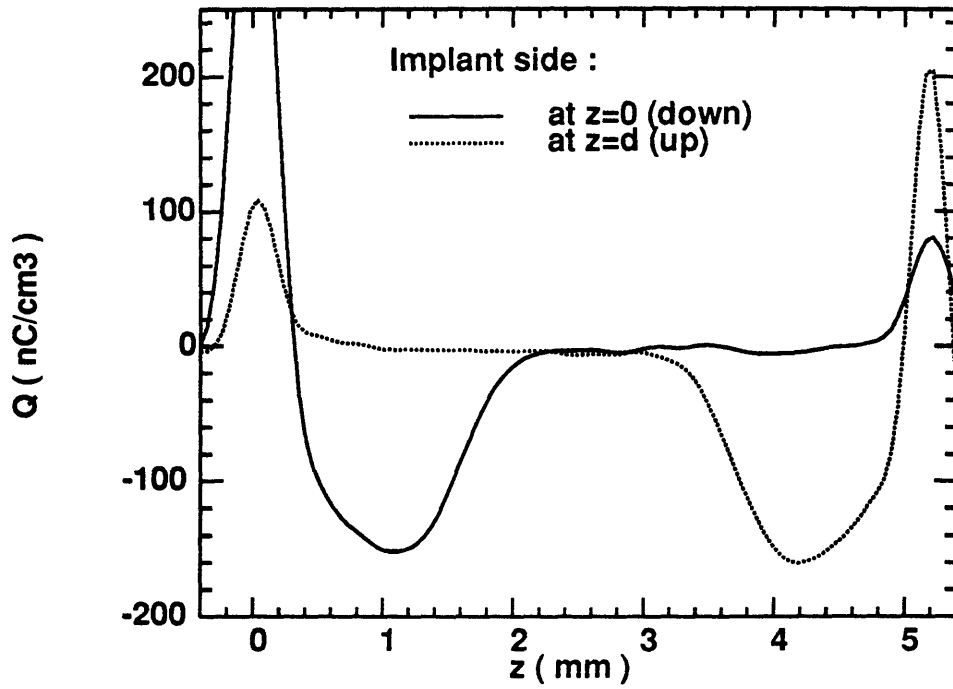
Figure 3.18: Shallow e-beam implant profile with implanted side at $z = 0$ (solid) and $z = d = 5.28mm$ (dotted).

PMMA
Field and Potential
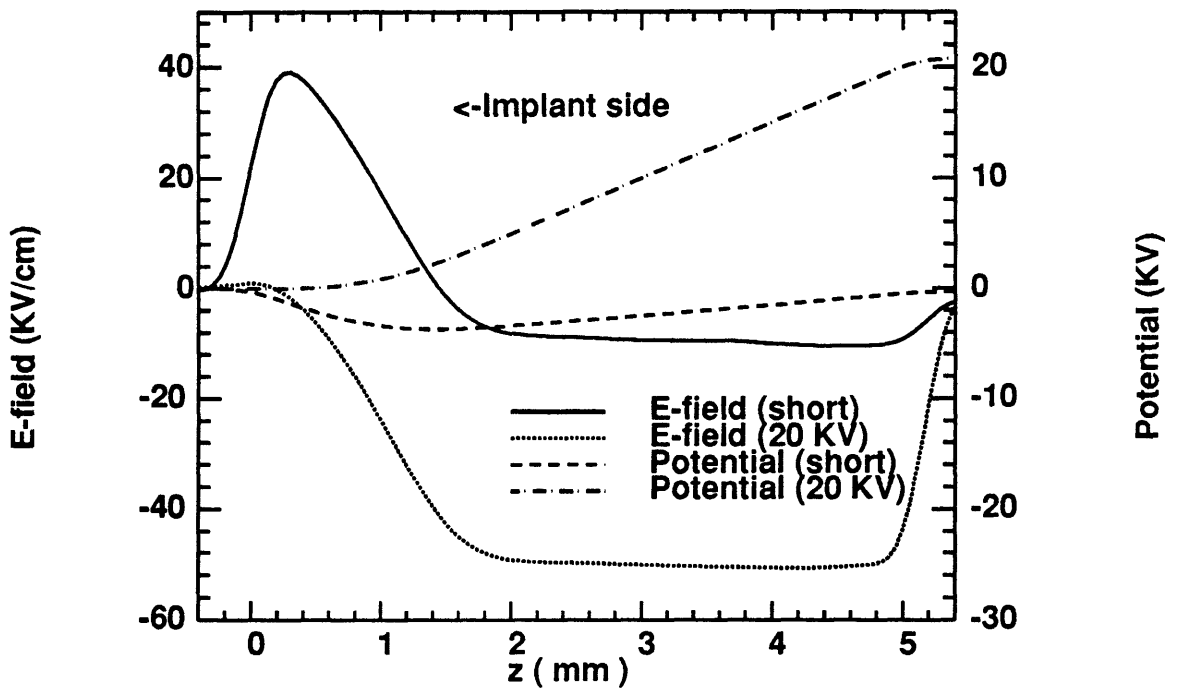
Figure 3.19: E and V associated with the sample of Fig. 3.18 with the irradiation side at $t = 0$ for the shorted sample (solid and dashed) and with 20 KV applied (dotted and double dotted)

The charge centroid, $\bar{z}$, and total implanted dose, Q_t, are determined from knowing the voltage which cancels the front peak as discussed in section 3.1. The implant side peak was canceled with 20 KV, while the opposite side peak was canceled with 7 KV. Both surface charges were positive in sign, so the lower electrode peak was canceled with positive voltages applied at the upper electrode. The centroid position is found from (3.4) substituting the relative canceling voltage for the surface E-field

$$\bar{z} = \frac{7}{20 + 7}d = 1.37 \ mm$$

and the net charge is determined by the negative sum of the two surface sheet charges

$$Q_t = \epsilon E_{int} = -\frac{\epsilon}{d}(27 \ KV) = -16.7\frac{nC}{cm^2}$$

which agrees with the intended implant dose.

The charge profiles of the sample with shallow implanted charge under short circuit and under 20 KV bias are shown in Fig. 3.20. The bulk profiles are not affected by the applied voltage, however,the surface sheet charge at $z = 0$ goes to zero. The closeness of these two curves allows one to conclude that the bulk charge profile is not affected by interference from the surface after deconvolution, resulting in an actual calibrated internal charge density profile.

Now that the resolution has been demonstrated for charge distributions which result from poling and electron-beam implantations, the time resolved effects will be presented in the next chapter. By looking at the evolution of space charge under bias, the mechanisms of charge trapping become more apparent than by observing the conductivity with time. The currents were not measured during the testing periods; therefore, the analysis will rely

PMMA
E-beam Implanted
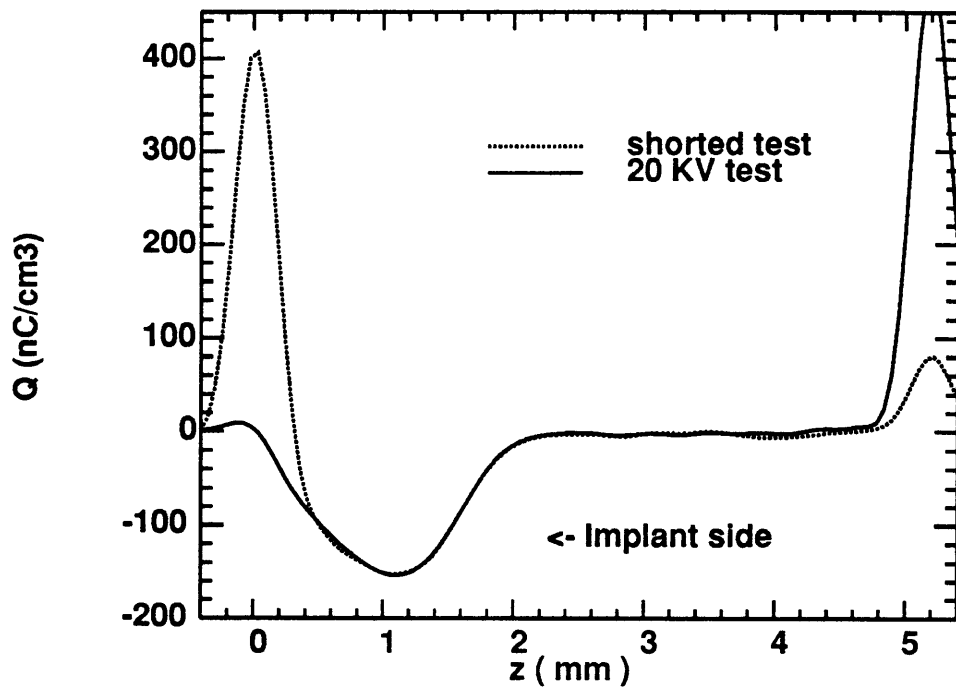
Figure 3.20: Bulk charge profiles under shorted (solid) and with 20 *KV* (dotted) across the sample.

on previously published data for values of the externally measurable time resolved conductivity.

Chapter 4

Dynamic Charge Measurements

Space charge measurements using ESAW tests can be performed repeatedly on the same sample throughout a poling process. Resulting profiles can then be compared with one another to obtain a quantitative dynamically changing space charge profile illustrating the interaction of various charge transport mechanisms.

The previous chapter has demonstrated the reliability of the technique for observing charge profiles as narrow as $\approx 200~\mu m$ in concentrations as low as $\approx 10 \frac{nC}{cm^3}$. Within this resolution, the internal charge dynamics of electrically stressed PMMA and PE can be compared to known models of injection and bulk transport. The resulting profiles from long time exposure to constant voltage suggest a variety of physical mechanisms may occur.

Room temperature experiments have shown that charge dynamics are undetectable on the time frame of several hours, throughout the electric field range tested as seen in section 3.2.2. This allows one to perform the space charge profiling tests at room temperature without accounting for charge redistribution within the material as long as the interruption is shorter than

130

about an hour.

Samples that have been poled at raised temperatures are cooled down to room temperature, profiled, then placed back in the oven for further testing. During the transition times of heating and cooling the sample, the poling voltage is maintained. Dynamic behavior during elevated temperature dominates the charge accumulation process. Therefore, a time interval between tests is approximately the time from when the sample reaches its final poling temperature until it has cooled down significantly, resulting in an error associated with the time between tests as discussed in section 3.2.1.

Once recorded and calibrated for every time throughout the poling process, the data can be compared to approximate $\frac{\partial \rho}{\partial t}(z,t), \frac{\partial \rho}{\partial z}$ and $E(z,t)$. Transient charging currents, J_q, due to the internal dynamics can be found at any point from charge conservation

$$\frac{\partial \rho(z,t)}{\partial t} = -\frac{\partial J_q(z,t)}{\partial z} \qquad (4.1)$$

allowing the approximation of a constitutive law relating J_q and E. The result is not expected to be linear since these materials are not expected to have ohmic behavior.

This chapter will present time resolved charge profiles obtained under the same poling conditions as section 3.2.2. PMMA and PE will be presented to illustrate the differences in bulk charge accumulation. Afterwards, a virtual cathode experiment will be presented to demonstrate the behavior of an imposed space-charge-limited condition.

4.1 Poling Experiments

The bulk charge profiles will be presented for 5.28 mm PMMA samples poled with 5 KV across the sample at ambient temperatures of 40, 50 and

90° C. Then, the profiles of two more samples poled at 50° C will be shown, having been poled at 2 and 15 KV. The charge evolution will be shown on the same set of axes for each series to compare each charge profile of a particular sample.

A similar analysis will be presented for a 3.1 mm thick PE sample having undergone poling at 40° C with 5 KV across it. As seen in the previous chapter, a variety of charge accumulation processes occur simultaneously in PE, making the analysis more complicated than PMMA. Consequently, the analysis will concentrate on characterizing PMMA.

4.1.1 PMMA Data

The most obvious characteristic of PMMA poled under raised temperature is the accumulation of heterocharge near the surfaces. The result of this is a positive polarization producing a short circuit surface charge having the same sign as the applied poling voltage. Details of the charge distribution, however, vary dramatically from samples poled at different temperatures and voltages. All the samples presented here were cut from the same bulk stock of 5.28 mm thick *Rohm&Haas Plexiglas* and the deconvolved and calibrated data will be presented in the same order as in the previous chapter: constant field, followed by constant temperature data.

Constant Field

Three samples were poled with 5 KV at three temperatures; 40, 50, and 90° C until a nearly equilibrium condition became established. This was determined by measuring the surface sheet charges of the anode and the cathode at each time interval until the net charge no longer varied signif-

PMMA
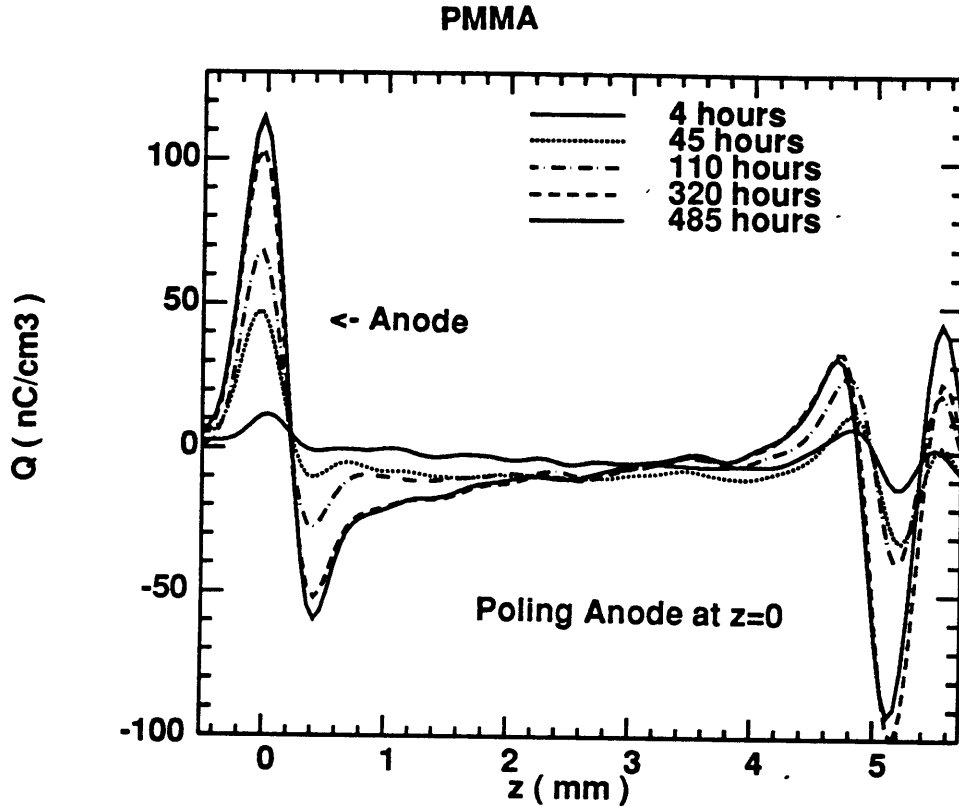
Figure 4.1: 40° C poling at 5 *KV* for several days.

icantly. These three profiles are shown in Figs. 4.1 and 4.2 and 4.3. The total poling times are listed for all three runs as are the calibrated charge density profiles.

These three figures are from samples profiled at room temperature under short circuit conditions with the anode at $z = 0$. What becomes apparent from these curves is the increase of trapped heterocharge build-up at the anode side with increased temperature. In contrast, the positive charge near the cathode becomes smaller at raised temperatures. Thus, the negative charge within the sample builds up at a faster rate with higher temperatures

133

PMMA poled at 50 C with 5 KV
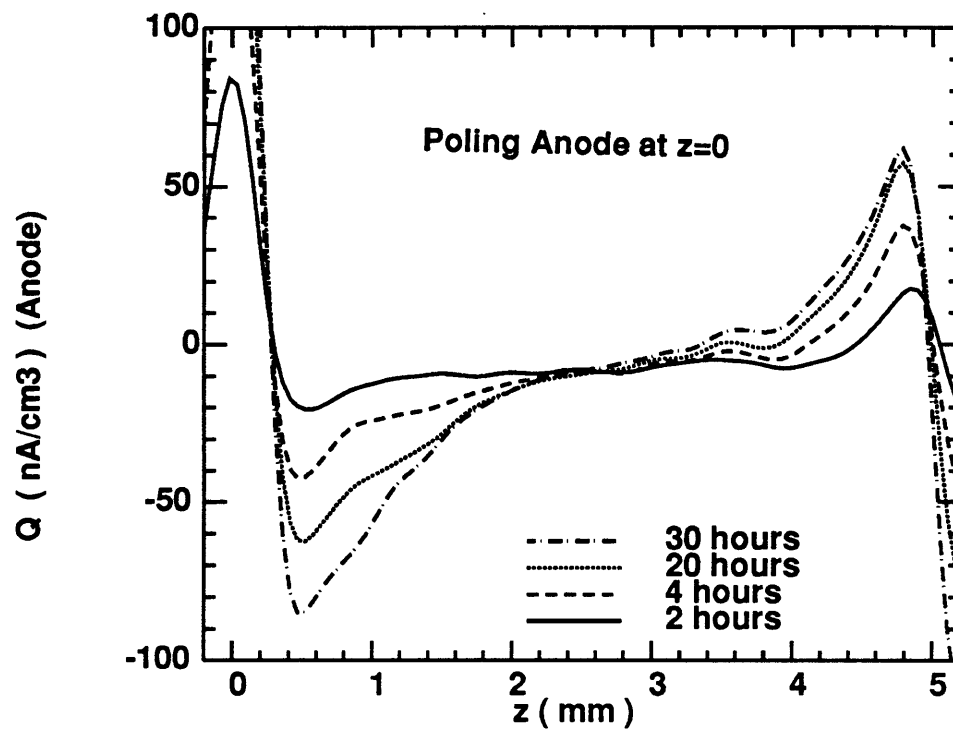
Figure 4.2: 50° C poling at 5 KV for many hours.

PMMA at 90 C with 5 KV
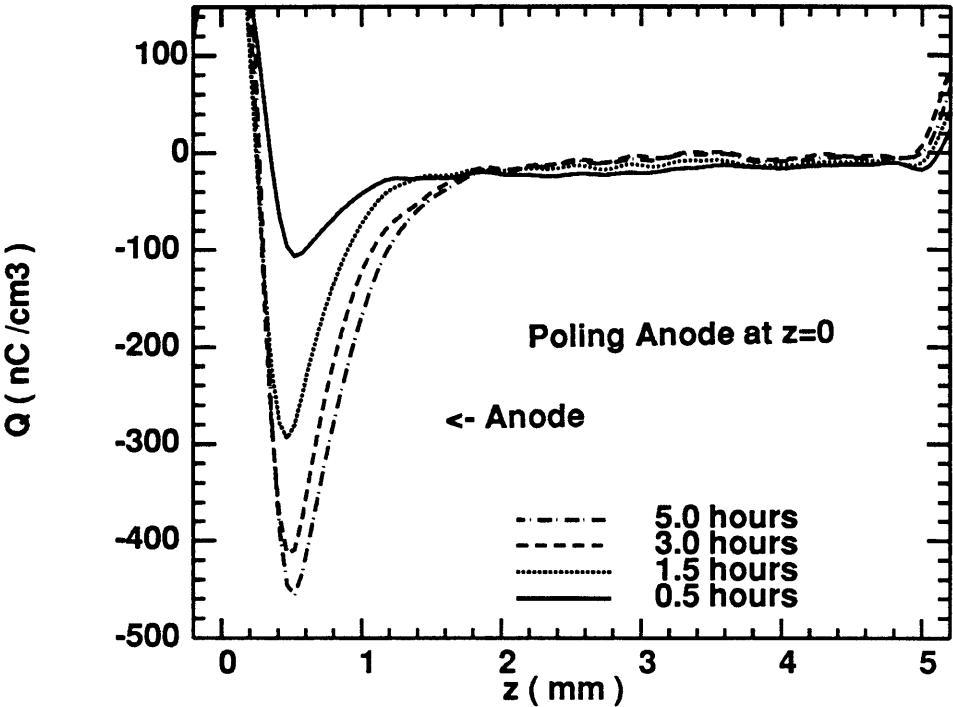
Figure 4.3: 90° C poling at 5 *KV* for several hours.

than with lower temperatures.

The net charge accumulating within the sample gives the externally observable current difference. By application of Gauss' law and charge conservation, the time rate of change in net charge Q_t relates to the difference in current densities

$$\frac{dQ_t}{dt} = J_0 - J_d$$

for

$$Q_t = \int_{z=0}^{d} \rho(z)dz$$

where J_0 and J_d are the current density (per unit area) at the electrodes $z = 0$ and $z = d$ respectively. The total external current has not been measured; however, the net charge was determined by summing the sheet charges at both electrodes at each time during the poling. An approximation for the charging current is the charge change with time. The net charge per unit area has been plotted in Fig. 4.4 with the log of time for the polled PMMA data. The corresponding electrode currents may be approximated from these curves to yield charging currents at different times. As an example, the initial charging current for the sample poled at 50° C with 15 KV has a current density

$$J_{charging} \approx 120\frac{fA}{cm^2}$$

which corresponds to a conductivity of

$$\sigma_{50°} \approx 10^{-17}\frac{\mho}{cm}$$

and is consistent with published values [49].

If the charge injection is assumed to occur within a monolayer of the cathode, the actual polarization can be approximated by the short circuit anode charge shown in Fig. 4.5. The 90° C data has been omitted from

136

Negative Total Charge
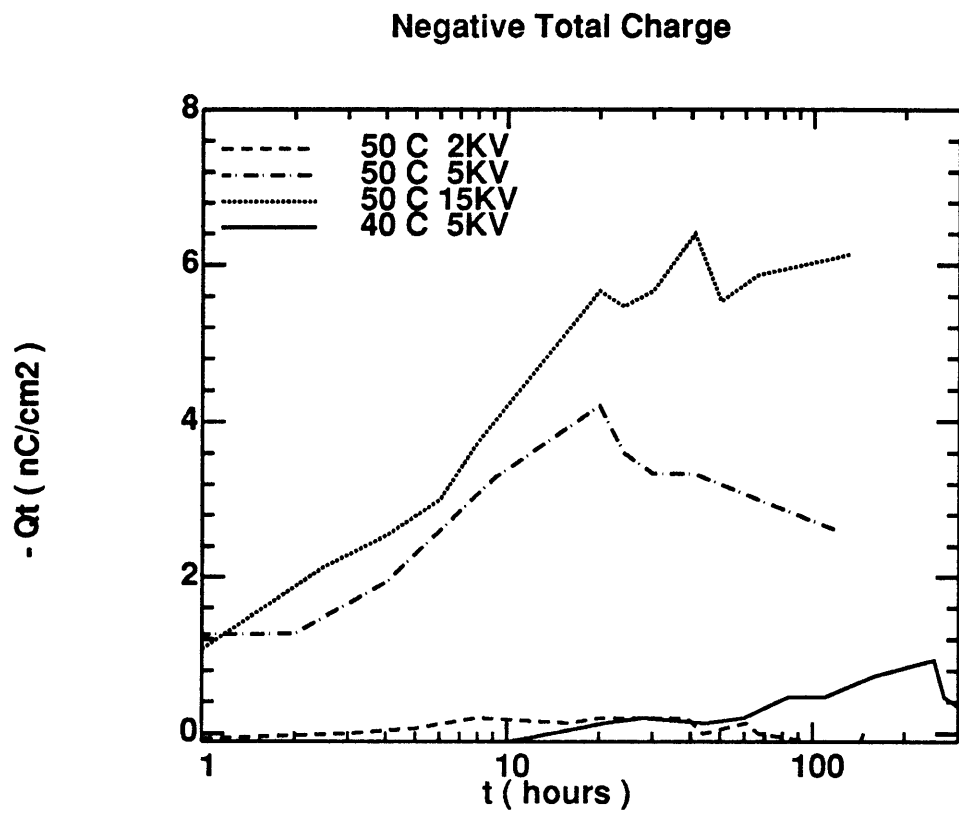
Figure 4.4: Net negative charge in PMMA poled at various fields and temperature

137
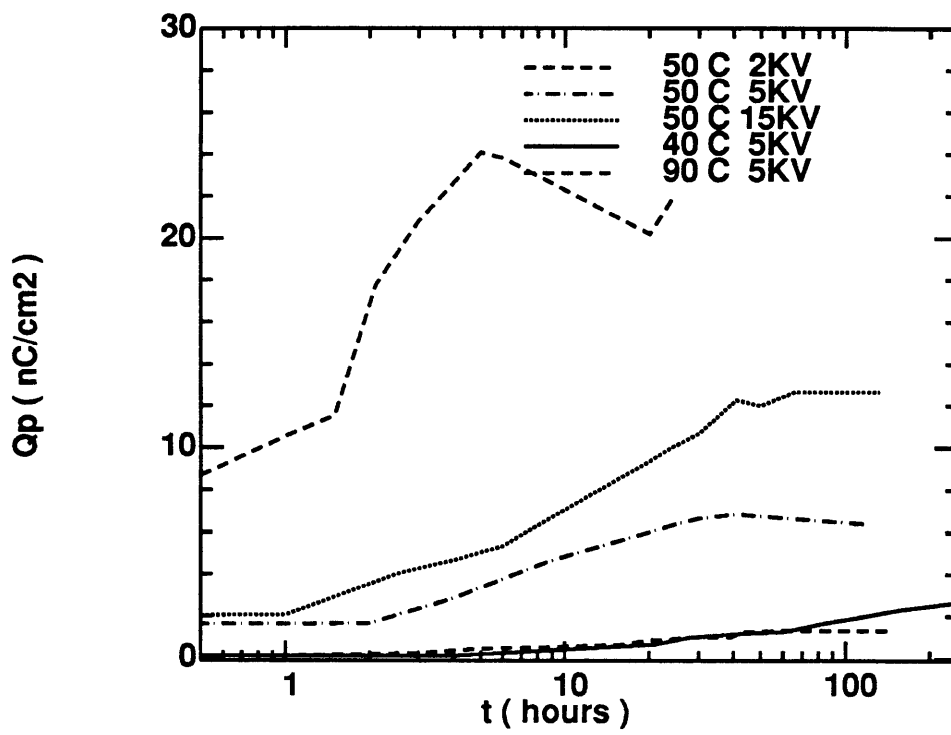
Anode Charge

Figure 4.5: Anode surface charge in PMMA poled at various fields and temperature

138

this plot since the anode charge is not much different than the net charge as seen by the plots of Fig. 4.3. The net charge accumulation in the low voltage (2 KV) 50 o C is negligible compared to the 5 and 15 KV samples, implying a non-linear relation between charge injection and applied voltage.

The two central curves of Fig. 4.4 are from samples poled at 50° C with 5 and 15 KV applied. The solid curve is from the sample poled at 40° C and 5 KV. The upper curve is from the 90°C data. All five curves are plotted on the same set of axes for comparison of the field and temperature dependencies.

Constant Temperature

The same poling experiment was performed at 50° C with 2 and 15 KV across the 5.28 mm thick materials. The accumulation profiles are shown in Figs. 4.7 and 4.6 while the net charge vs time is in Fig. 4.4. These samples were also measured under short circuit conditions with the anode side at $z = 0$.

All the charge profiles observed from 50° C poling appear to saturate after about 100 $hours$ of poling. This is the justification for choosing these curves as the steady state plots in the previous chapter.

An error of approximately $10\frac{nC}{cm^3}$ is still assumed for these plots placing most of the 2 KV data within the noise margin. Although, the presence of bulk bipolar space charge is nearly symmetric about the sample center. The net accumulated charge is below $4\frac{nC}{cm^3}$ although the general shape is similar to the 5 and 15 KV samples. Heterocharge accumulates near the two electrodes while the negative charge in the vicinity of the anode is larger than the positive charge near the cathode.

139
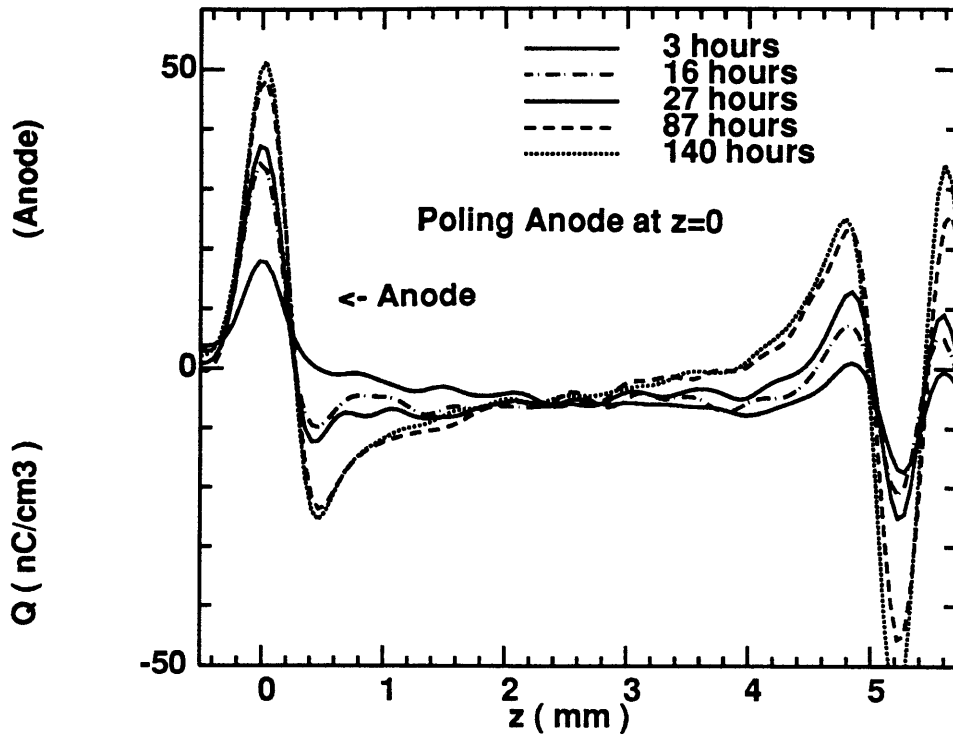
PMMA

Figure 4.6: 50° C poling at 2 *KV* for several days.

PMMA
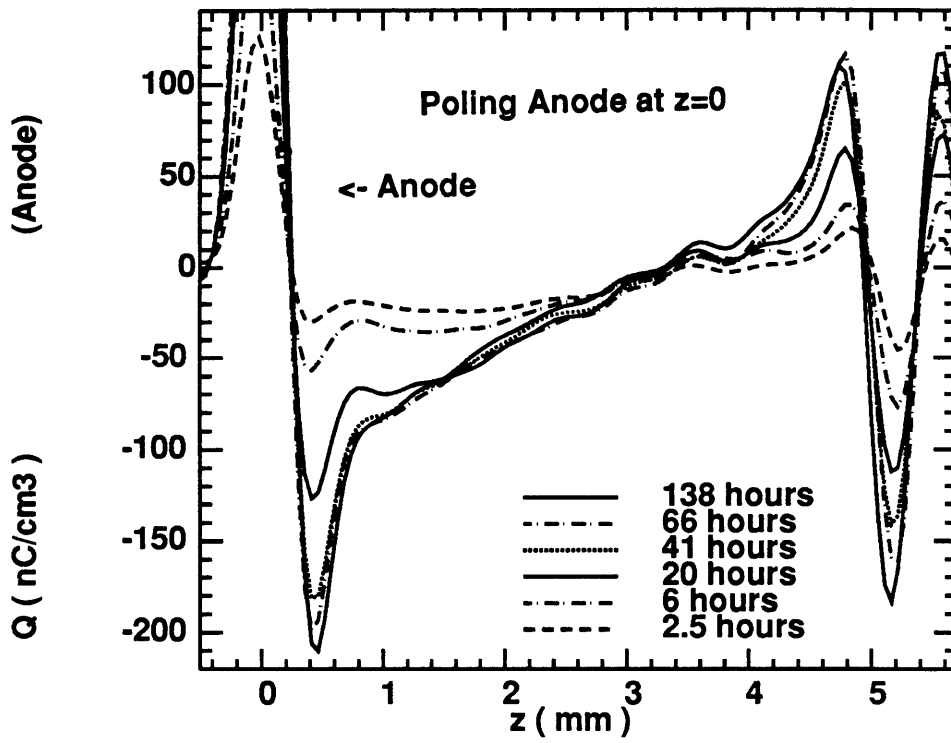
Figure 4.7: 50° C poling at 15 *KV* for several hours.

PMMA at 50 C and 5 KV
with compensating voltage
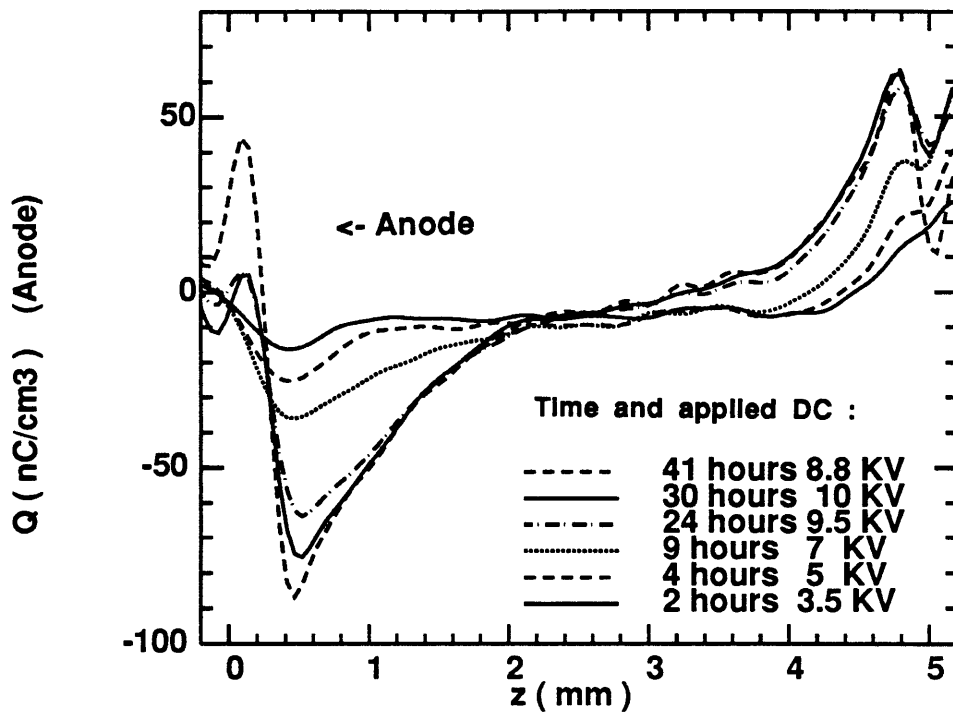
Figure 4.8: 50° C poling at 5 KV for several hours with the anode charge compensated.

PMMA at 50 C and 15 KV
with compensating voltage
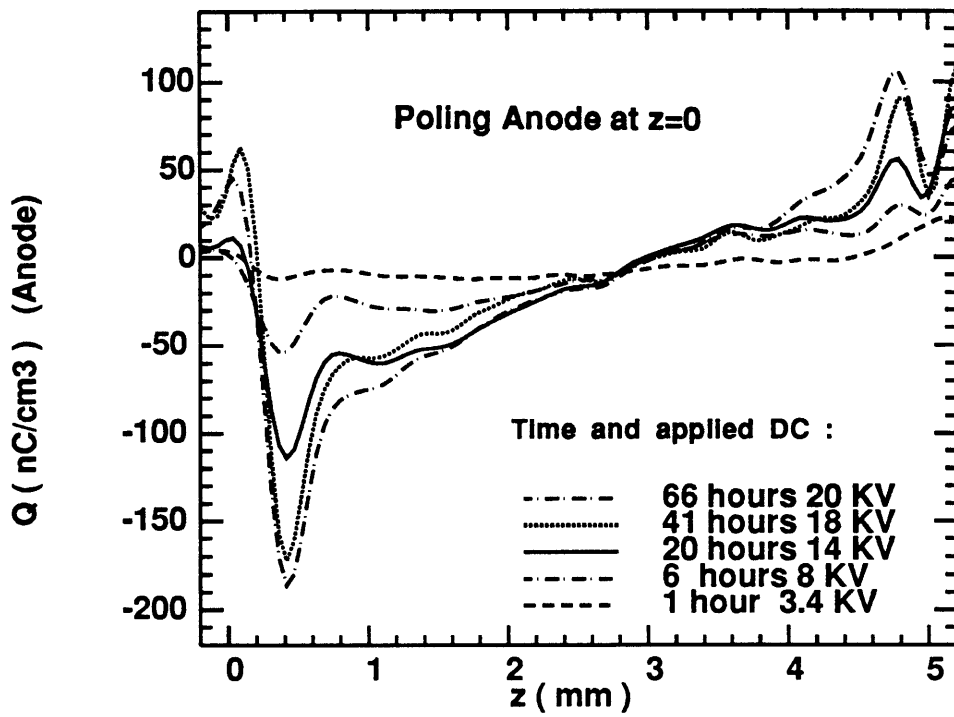
Figure 4.9: 50° C poling at 15 *KV* for several days with the anode charge compensated.

The surface image charge is essentially canceled by applying a DC voltage across the sample while it is being profiled. The voltage applied gives the amount of charge residing at the surface. A dipolar charge layer beneath the electrode will not be compensated if the charge is trapped within a small layer. It is clearly seen in Figs. 4.8 and 4.9 that a narrow homocharge layer appears after the short circuit image charge has been canceled.

The series of profiles shown in Figs. 4.8 and 4.9 are space charge profiles of PMMA poled at 50° C with 5 and 15 KV applied. These two series are measured with the appropriate voltage to cancel the short circuit image charge. Since the charge at the anode is positive, the opposite polarity voltage applied across the sample cancels the charge. Hence, the voltages indicated are positive voltages applied from the bottom electrode ($z = 0$) to the top ($z = d = 5.3\ mm$).

One observation is the appearance of a near-surface dipolar charge after approximately 20 *hours* for both poling voltages. This represents accumulation of a narrow homocharge layer in the vicinity of the electrode, too close to be resolved under short circuit conditions. This charge sheet has the effect of reducing the field at the metal electrode by imaging much of the charge in that layer.

Also apparent is the similarity of bulk charge distribution for the two samples after 41 *hours* as seen in Fig. 4.10. The 5 KV sample is compensated with 8.8 KV, corresponding to $5.5\frac{nC}{cm^2}$ and the 15 KV sample is compensated with 18 KV, or $11.2\frac{nC}{cm^2}$. Once equilibrium has been established, the trapped charge density throughout the bulk appears to be independent of applied field while most of the excess heterocharge is concentrated near the anode for the higher field sample.

144

PMMA after 41 hours at 50 C
with compensating voltage
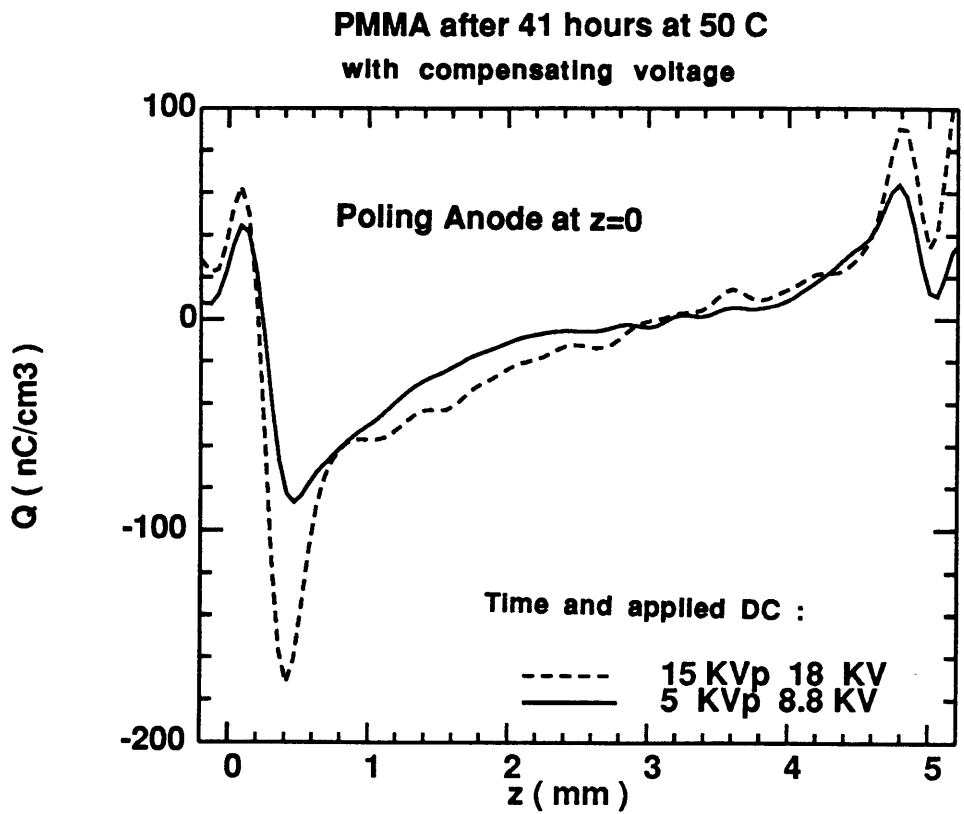
Figure 4.10: 50° C poling at 5 and 15 *KV* for 41 hours with the anode charge compensated.

4.1.2 PE Data

The space charge accumulation profile for a PE sample poled under the same applied voltage and temperature as the $40°$ C, 5 KV PMMA sample will be presented next. The sample thickness is 3.1 mm, as compared to 5.28 mm, so the field in this sample is 1.7 $times$ as large. These PE samples exhibit homocharge near the electrodes resulting in a negative polarization, as described in section 3.1 and expected from the PE data in the previous chapter.

A 3.1 mm sample of PE was poled with 5 KV at a temperature of $40°$ C and periodically profiled using ESAW over several days. The series of short circuit poling tests is shown in Fig. 4.11. The latest two profiles after 13 $days$ (320 $hours$) and 20 $days$ (485 $hours$) follow each other closely enough that the material can be considered in steady state. Under this condition, the current no longer changes with time so the external current would appear constant in time.

The poling cathode is at $z = 0$ in this figure, indicating that the negative charge to the right of the electrode is injected charge, moving across the sample to the anode. The homocharge concentration is most obvious on the cathode side, although, there is a small positive peak on the anode side appearing soon before 100 $hours$. The signal from the anode side is obscured by the acoustic mismatch and the presence of a narrow dipolar layer.

This figure can be compared directly with the PMMA data of Figs. 4.1 and 4.1. The similarity of the shapes is striking with one major difference; the polarities are reversed. The PE data is shown with the poling cathode at the left ($z = 0$) and the PMMA data is shown with the poling anode at the left. The accumulation of polarization charge appears to resemble the

146
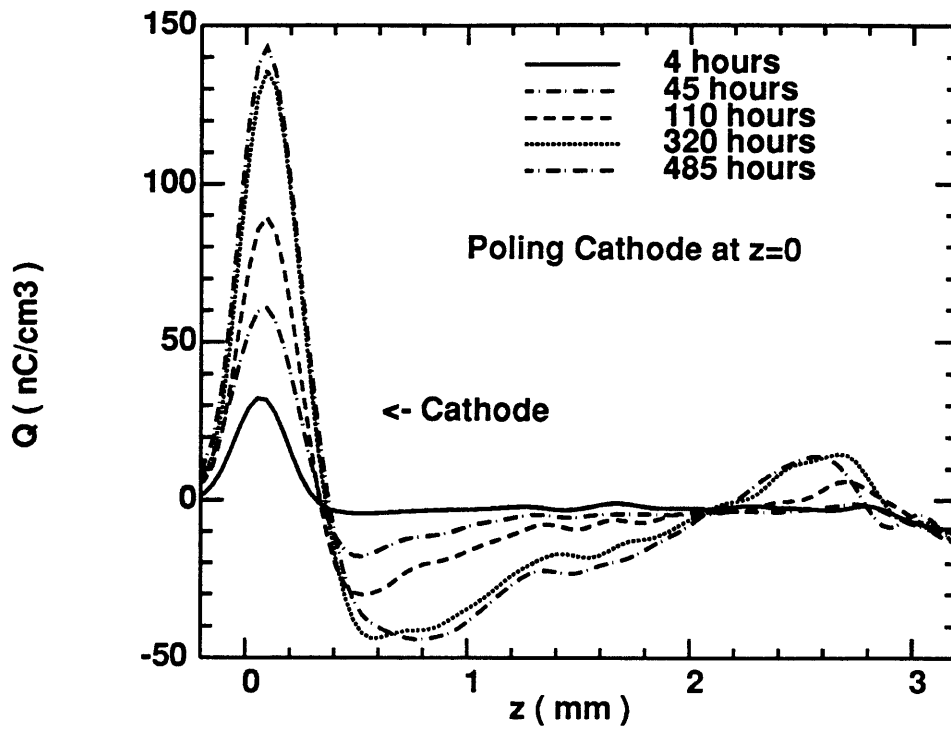
PE at 40 C and 5 KV

Figure 4.11: Polyethylene poled at 40° C and 5 *KV* for 20 *days* with the poling cathode at $z = 0$.

injection of homocharge from the opposite sides.

The DC voltage needed to cancel the front peak is 5 KV in the same direction as the poling field. Since this is also the poling voltage, the space charge current limit is reached since the E-field is zero at the cathode. This result suggests that the PE samples above $40°C$ achieve space charge limited current flow with an essentially ohmic cathode. The injected charge behaves like a virtual cathode [41] and electrons are trapped in the bulk near the electrode.

Using this model, the negative charge distribution should move across the sample towards the anode while the E-field increases on the anode side. Some evidence of this charge migration is apparent for long times (between the last two profiles), seen by the double dotted line being displaced from the dotted line of 165 *hours* earlier.

The PE sample discussed here and the PMMA sample poled at 90° C have a virtual cathode characteristic since the E-field at the real cathode is zero under bias. The next section will discuss a way of imposing a virtual cathode condition in PMMA by implanting the shallow electron profile discussed in section 3.3

4.2   Virtual Cathode

Space charge accumulation from normal poling at raised temperatures results from effects at both electrodes and the bulk. Profiling the charge throughout the poling process can give an indication of where trapped charges lie, although, whether the dominant carrier is positive or negative can not be uniquely determined. Any net internal charge results from an imbalance of injection at the boundaries.

148

To determine bulk material properties, distinct from the electrode, an electron-beam was used to implant excess negative charge within a small layer near a surface. An opposing DC voltage was applied across the sample, bringing the field at the electrode nearest the implanted charge to zero. This condition on the implanted charge makes it a *virtual cathode* and forces the charges to decay with the bulk material properties and the anode. The implanted charge layer is treated as a purely ohmic contact as long as the voltage across the bulk is continuously adjusted to compensate the image at the anode. Assuming the voltage is correctly applied, the net charge decay will be due to transport at the anode.

In order to impose a space charge limited type of condition, the shallow implanted profile described in section 3.3 has been used to form this virtual cathode [41]. The shallow negative charge can be completely imaged on the opposite side by watching the first peak of the ESAW output. When the appropriate DC voltage is applied, that peak disappears making the field zero at the metal cathode surface. This is shown schematically in Fig. 4.12 where the charge layer is completely imaged on the electrode at $z = d$, so the surface charge on the $z = 0$ electrode is zero.

The resulting E-field is then concentrated within the unimplanted region between the implanted virtual cathode and the metal anode. This condition meets the definition of a virtual cathode for standard space charge limited current calculations [41]. The electron concentration is imposed from an external source, but is effectively in ohmic contact with the sample since there is a reservoir of negative charge available for conduction at the cathode.

As long as the external voltage follows the charge motion to continually compensate for charge motion and decay, the virtual cathode condition can

149

Implantation Direction
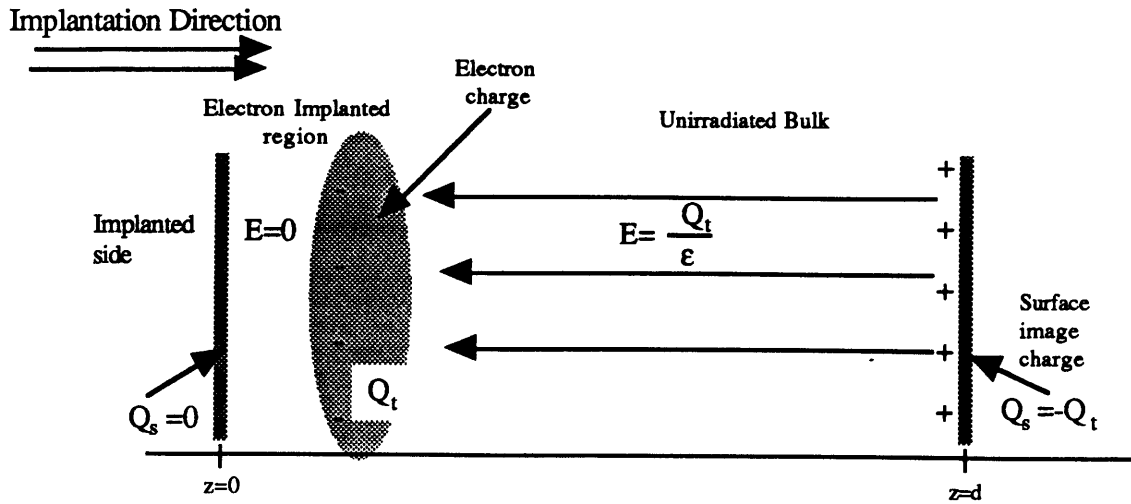
Figure 4.12: Representation of the imposed virtual cathode condition on an implanted charge distribution close to the electrode at $z = 0$.

be maintained. This allows one to trace the charge dynamics under an artificially imposed space charge limit, removing the effects of transport through the cathode.

The net charge in the sample is found by taking the negative sum of the surface image charges as discussed in section 3.1. Following the net charge decay under the virtual cathode condition gives the net injection through the anode since the zero field condition is imposed on the injection-side electrode. Trapped bulk charges within the unirradiated sample can then be compared with a normally poled sample under the same field and temperature conditions to allow a true comparison with a simple poling experiment.

The side from which the electrons enter will have radiation induced conductivity enhancement allowing the charges to redistribute deeper in the bulk under the applied field. An approximate value for the relative conductivities can be found by observing the decay under short circuit conditions. This conductivity is expected to change with time at elevated temperatures

150

where damage caused by the implantation becomes annealed. The short circuit decay of one sample will be presented first, followed by the virtual cathode test performed at 60° C. Afterwards, a room temperature virtual cathode experiment will be presented.

Two samples were irradiated with approximately the same electron energy and dose and tested at 60° C. One sample was placed in the poling oven with the electrodes grounded together, while the other sample was placed under a changing voltage to compensate the unpaired charge. The shorted sample exhibited a decay due to the self-induced field and conductivities within the material.

4.2.1 Short Circuit Data

The decay profile shown in Fig. 4.13 demonstrates how the charges distribute themselves within the material during the decay process. Since the charge centroid $\bar{z}$ is so close to the *bottom* electrode ($z = 0$), the field is much larger in the vicinity of that electrode than in the sample bulk. Since $z = 0$ is also the side from which the electrons entered, one can assume that the conductivity is enhanced as well.

A double peak profile appears during the decay. The central peak remains at nearly the same position throughout the decay, while a second peak appears next to the electrode. In this profile, both electrodes are effectively *anodes*, so the material became *self-poled* under its own field.

After the initial 20 *minutes* decay, the rate appears to slow down as if the conductivity of the material decreases. Using a simple linear conductivity model, the plot on a semilog plot of total charge verses time should be a straight line with a single time constant. Fig. 4.14 shows the log of the net charge verses time for the shorted sample (dashed line) in comparison with

151

Shorted Decay at 60 C

Figure 4.13: Space charge profiles of the decay at 60° C for E-beam implanted charge in PMMA under short circuit conditions.

Charge Decay at 60 C

Figure 4.14: Net negative charge in a short circuited (dashed) and virtual cathode (solid) condition for E-beam implanted PMMA at 60° C.

the virtual cathode sample (solid line) at 60° C.

The slope of the simple decay curve continually increases with time as if the time constant gets longer. This can be explained by the effects of temperature on the material. At this temperature, the implanted material has an initially high conductivity by comparison to later times.

The peak E-field in the irradiated side of the material is found by the voltage required to bring the surface charge to zero. For the sample placed under a short circuit, 18 KV cancels that peak. Hence, the field at that electrode is $3.4\frac{KV}{mm}$ (5.28 mm sample thickness). The charge, found from

Fig. 4.14, changes from 12 to $6\frac{nC}{cm^2}$ in 20 *minutes* (1200 *seconds*) resulting in

$$\frac{dQ_t}{dt} = 5\frac{pA}{cm^2}$$

Ohms law allows the approximation of an upper limit on the conductivity since the field at the electrode is the maximum field. Hence the value for

$$\sigma_{max} \approx \frac{\frac{dQ_t}{dt}}{E} = 1.5 \times 10^{-16}\frac{\mho}{cm}$$

is a good approximation for the conductivity in the irradiated region determined by the short circuit decay, although, this material is not a linear conductor.

The charge peak remaining near the original charge centroid experiences a much smaller field since it is closer to the center and has a larger portion of the charge imaged at the opposite electrode. Also, a large population of trapping sites is likely within the irradiated material forcing the charge density to remain for a long time.

4.2.2   Compensating Voltage Data

Elevated Temperature

Each time the sample is removed from the poling oven, the voltage required to image the charge at the opposite anode $z = d$ is determined. After a test, the sample is replaced with that same voltage while the oven is ramped back up to 60° C. This process has been repeated numerous times, and the charge progression profiles is shown in Fig. 4.15.

The behavior of the charge in this sample is dramatically different than the shorted sample decay sample. During the first 20 minutes, the charge centroid shifted approximately 0.4 *mm*. The net charge, however, remained

154

Virtual Cathode at 60 C

Figure 4.15: Space charge profiles of the decay at 60° C for E-beam implanted charge in PMMA under virtual cathode conditions.

155

nearly constant. There is also an obvious bulk space charge between the charge peak at $z \approx 2$ mm and the electrode at $z = 5.3$ mm. The space charge region builds up to a nearly equilibrium condition after 2 *hours*, although the heterocharge continues to build up in the vicinity of the anode.

As the implanted charge layer becomes on the same order of the space charge layer, the E-field within that region varies across the sample, and the trapped charge begins to dominant the profile. To illustrate this point, the E-field profile has been obtained by integration of the charge profile and is shown in Fig. 4.16 with the compensating poling field applied during the test. The bottom (solid) curve is the profile immediately after irradiation before being placed in the poling oven.

As the space charge builds up within the sample, the slope of the E-field increases. The linearity of the curves in the bulk region suggest that the distribution is nearly uniform. At longer times, the profile begins to have structure as the charges redistribute themselves under the influence of the field gradient. This redistribution is further clarified by comparing the charge profile for times much greater than 2 hours.

Fig. 4.17 is a series of profiles for the same virtual cathode sample at 60° C after 2 hours of charge decay. The profiles indicate the implanted charge has receded to around the background trapped charge level after approximately 12 *hours*, although, there is a large amount of space charge in the unirradiated region. This leads to the question of how those charges developed. To decide whether the charge accumulation in the bulk resulted from the presence of initially unpaired implanted charge or from the presence of a field, a third sample of the same material was poled under identical conditions.

156

Virtual Cathode field distribution
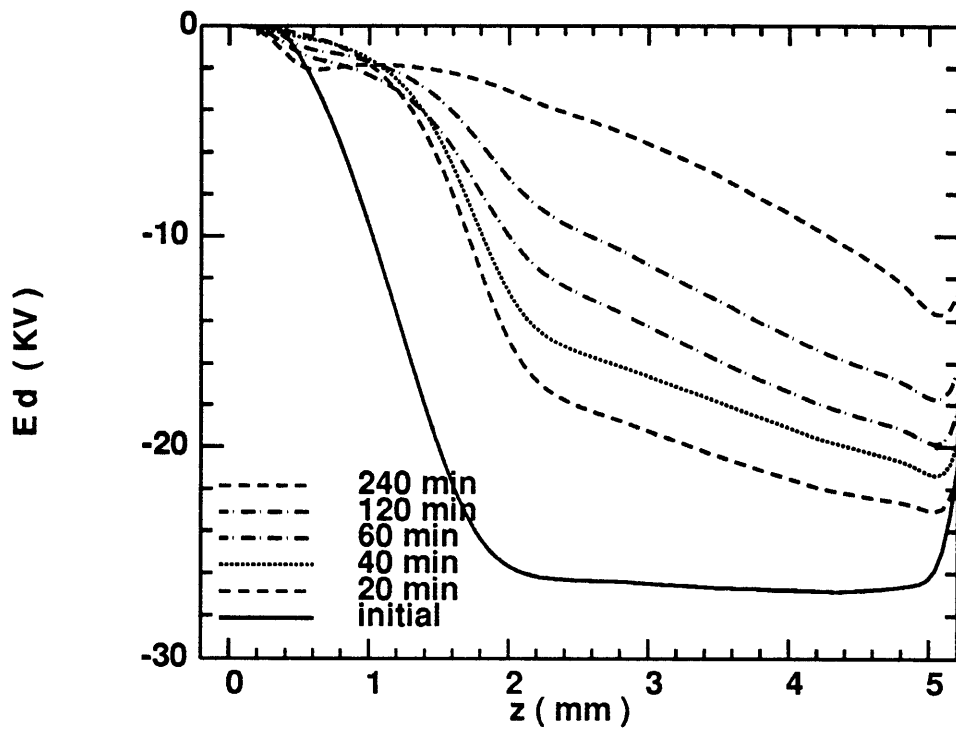
Figure 4.16: E-field profiles of the decay at 60° C for E-beam implanted charge in PMMA with the DC voltage applied forcing the surface charge to zero at $z = 0$.
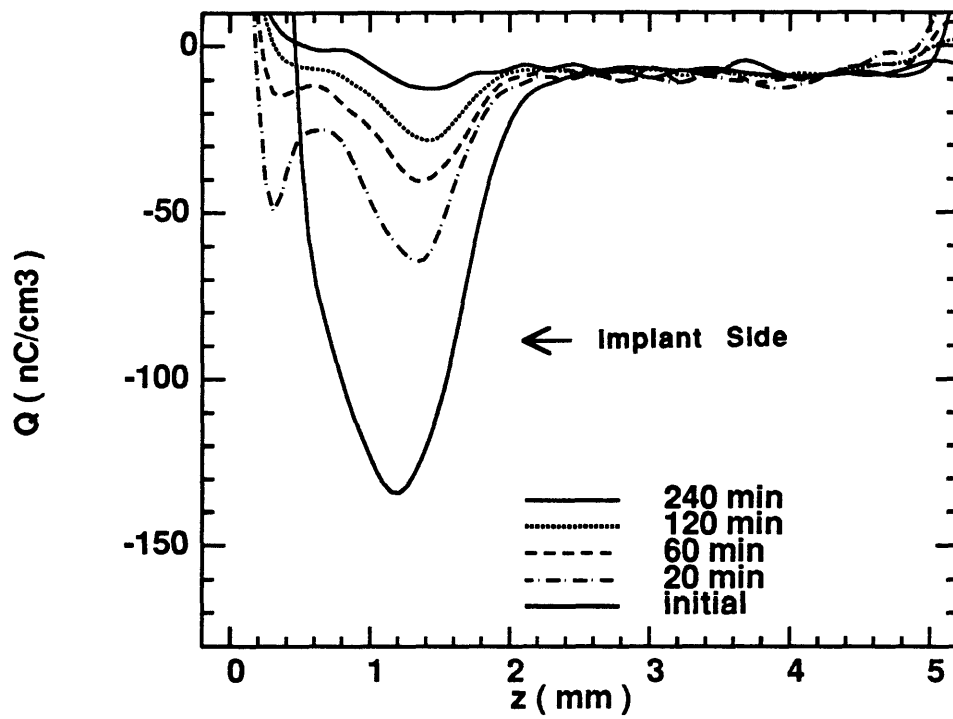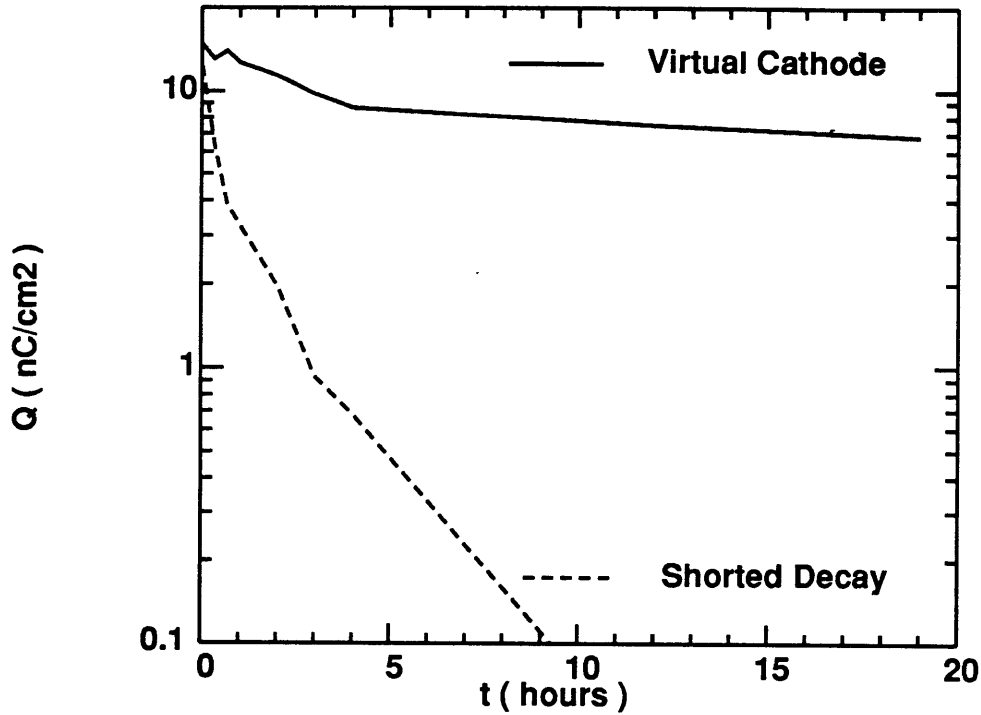
Virtual Cathode at 60 C
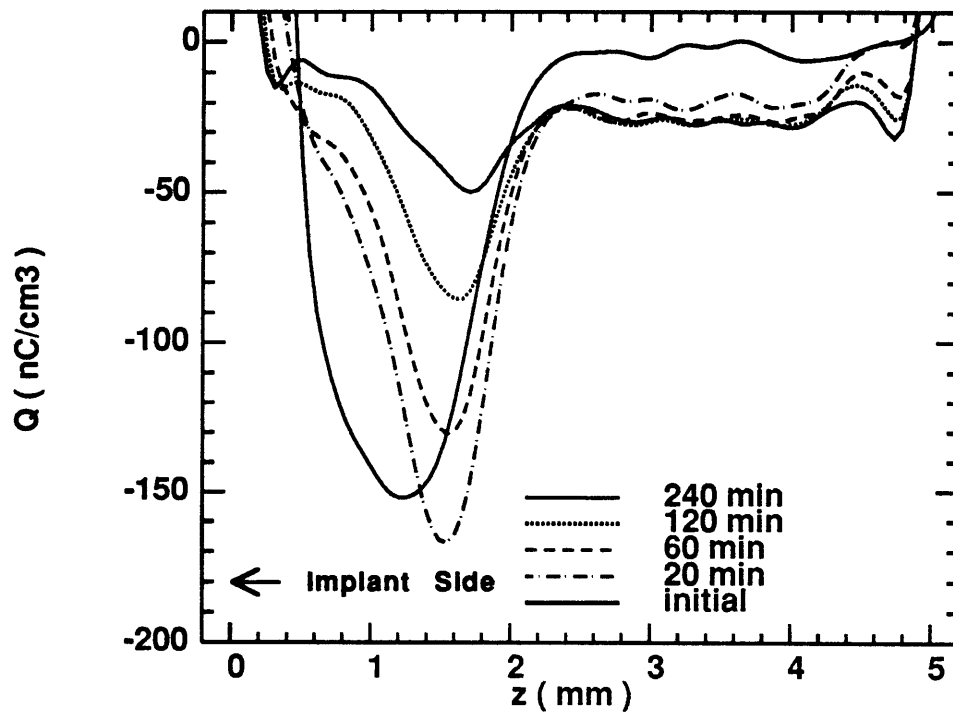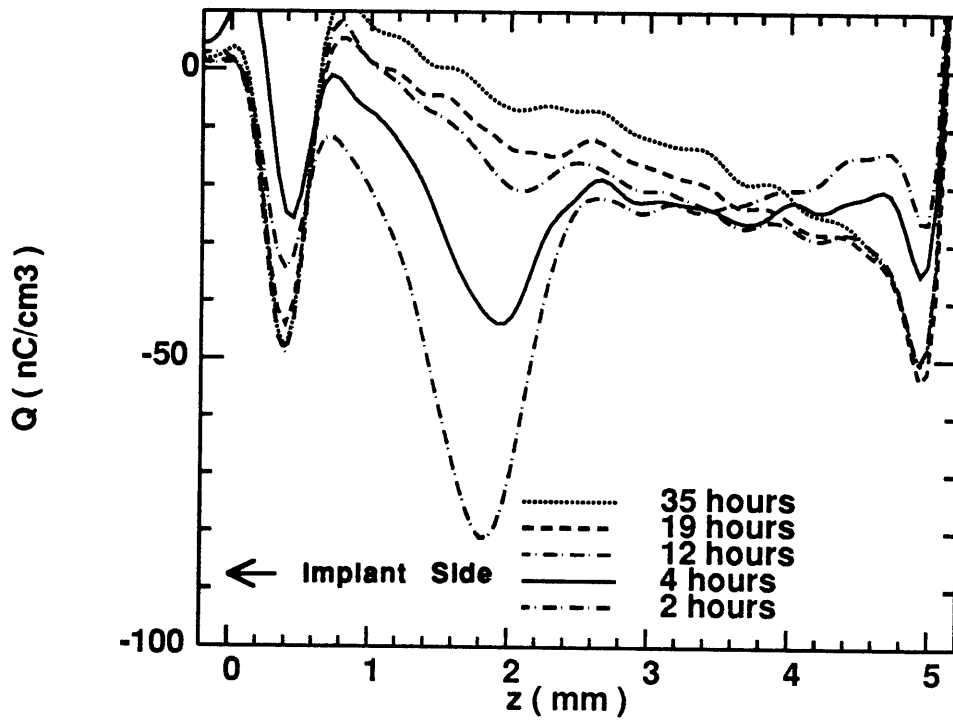

Figure 4.17: Space charge profiles of the decay at 60° C for E-beam implanted charge in PMMA under virtual cathode conditions.

Poled at 60 C
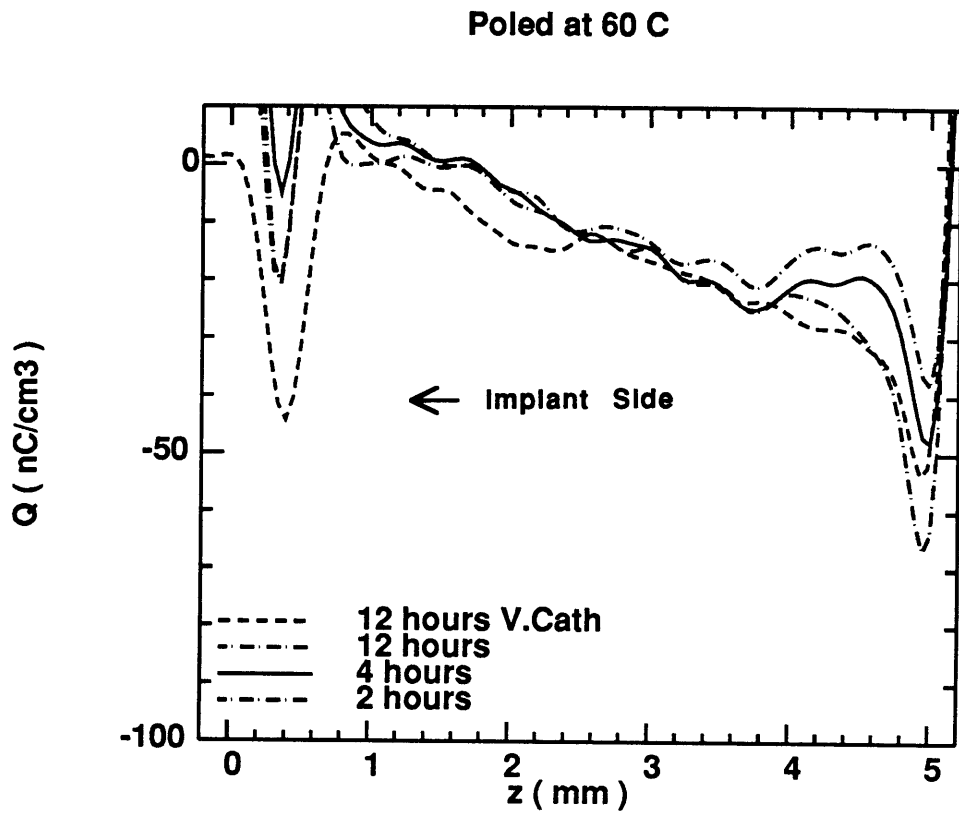
Figure 4.18: Space charge profiles of the initially uncharged PMMA at 60° C having experienced the same voltage as the virtual cathode sample and the 12 hour profile of Fig. 4.17.

159

One can compare the charge profile of the virtual cathode sample to the initially uncharged material having undergone the same electrical history. The field after implantation with 20 KV to cancel the charge at the metal cathode is 28 KV within the sample, shown in the initial profile of Fig. 4.16. The unirradiated sample has only the applied voltage across, hence The field in the secondary sample is approximately $\frac{7}{10}$ the field in the implanted sample.

Considering this difference, the two curves after 12 *hours* shows that space charge profile is affected by the field, as seen in Fig. 4.18. The close similarity illustrates that the accumulation of space charge depends on the field and the temperature rather than on the presence of negative charge. The same figure also shows the development of the space charge at two previous times for comparison to Fig. 4.17.

To test the reliability of the charge and E-field plots, one final integration of the E-field to yield the total potential can be compared to the known applied voltage. Fig. 4.19 demonstrates the accuracy associated with this series of experiments since the potential at the anode $(z = d)$ is very close to the applied voltages for every test performed. The curves are labeled with the poling time and applied voltage in KV.

Room Temperature

The virtual cathode experiment has been performed at room temperature for a 6.0 *mm* thick sample of PMMA from the same manufacturer. This sample was implanted with an equivalent dose as the previous two samples discussed, however it was placed under bias at room temperature for several weeks while the temperature was maintained at 20° C ± 10%. The decay

160

Virtual Cathode with applied voltage
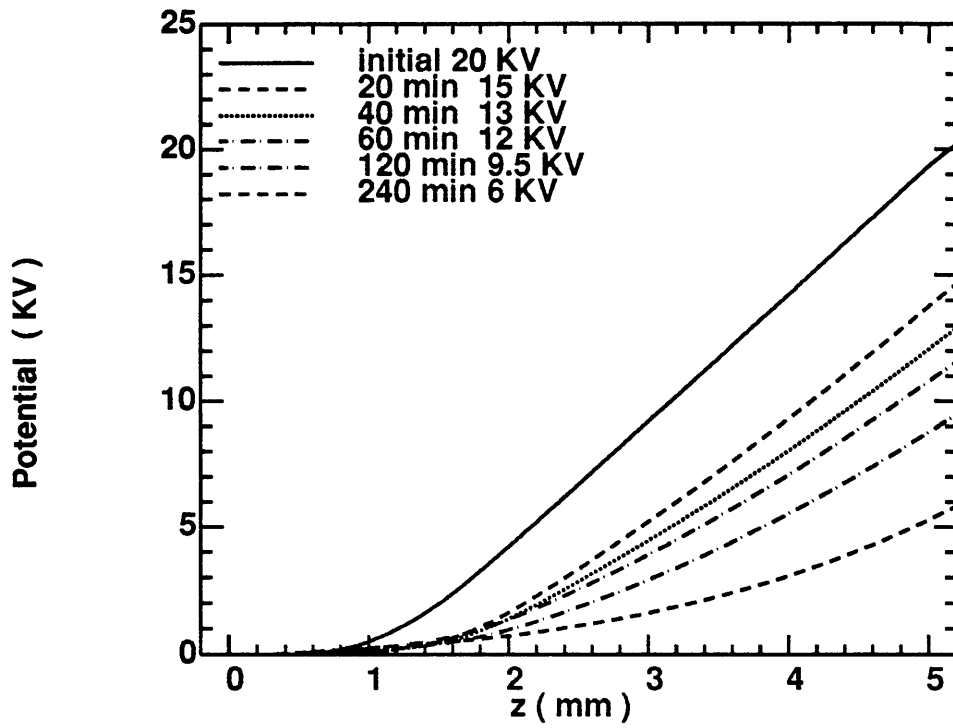
Figure 4.19: Potential profiles found by integration of Fig. 4.16 for comparison to applied voltages.

Room Temperature Virtual Cathode
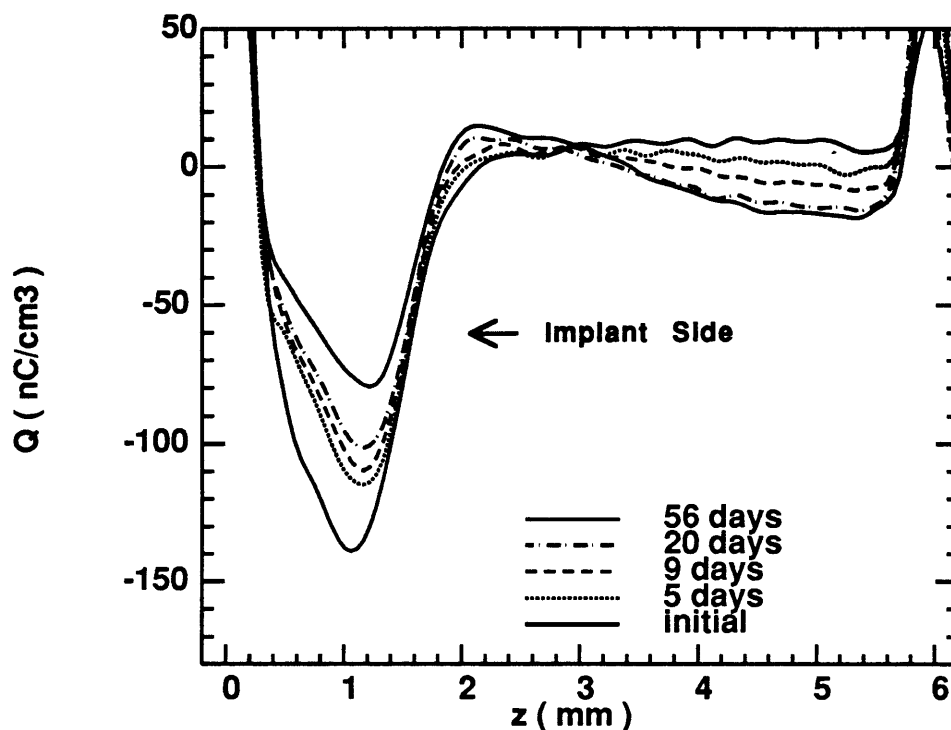
Figure 4.20: Space charge profiles of the decay at 20° C for E-beam implanted charge in PMMA under virtual cathode conditions.

data is shown in Fig. 4.20.

The space charge appears to accumulate near the anode in the same manner as the 60° C sample, however, the space charge characteristics near the implanted charge region are different. The charge concentration does not shift beyond the initial profile, suggesting that the conductivity is not dramatically enhanced at 20° C by the irradiation. The implanted charge profile appears to maintain its shape as is magnitude simply decreases with time.

The net charge decay of all three implanted samples have been plotted

162

Implanted charge decay
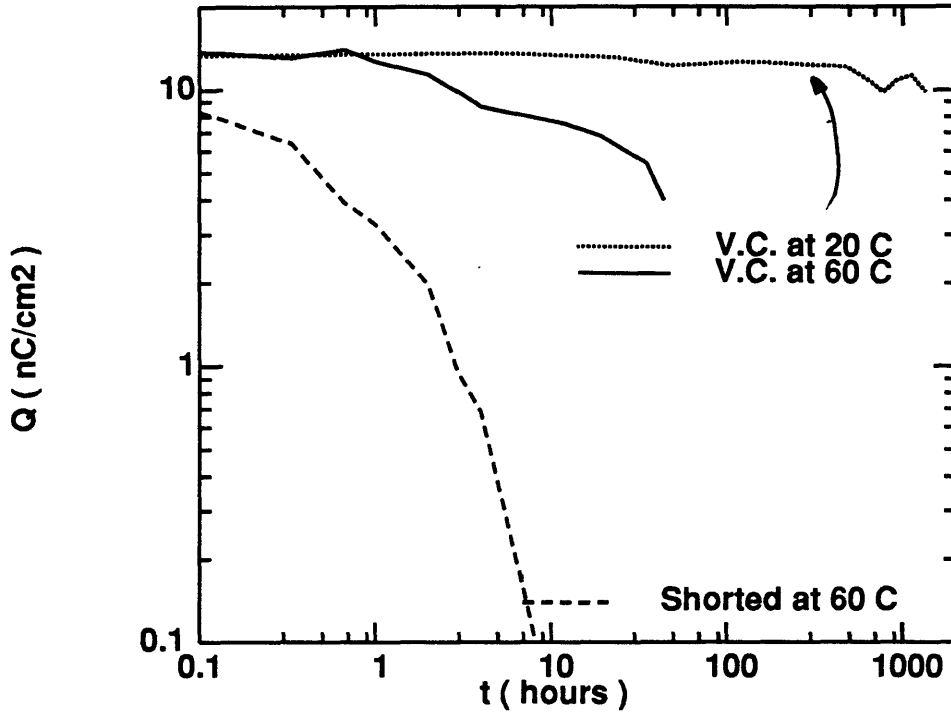
Figure 4.21: Implanted charge decay for the virtual cathode at 20 and 60° C and the shorted sample at 60° C.

in Fig. 4.21. Here, the decay is portrayed in a *Log-Log* plot to allow the full range of times and charge densities to be seen. The fastest decay is observed with the shorted sample, as shown previously, while the 20° C sample under virtual cathode conditions exhibits no significant decay after 56 *days*.

Heterocharge appears in the vicinity of the implanted charge peak with a zero at $z = 3$ *mm*, the center of the sample, throughout the time of the experiment. The net charge has only decreased by about 16%, thus, the space charge accumulation appears to be a consequence of the bulk field. The implanted charge peak appears to decrease as a result of the background

charge being more positive and the charges remaining immobile.

The next chapter will be concerned with analyzing the data presented in this and the previous chapter in order to attempt a coherent explanation of the variety of behavior observed. Trapping and transport will be explained in terms of well established theories of polarization and transport.

Chapter 5

Observations and Analysis

Many authors have addressed charge transport mechanisms in polymers and other amorphous materials [3, 43, 45]. Unfortunately, one can not easily model all the effects of trapped electron charge and mobile ionic carriers from space charge distribution measurements, even in conjunction with current measurements, due to the seemingly endless number of available parameters. Insights from the profiles presented in the previous two chapters can be combined with published data and observations from other investigators in order to help understand the transport physics taking place.

A brief qualitative description of a mechanism which has been generally accepted by many theorists and could lead to the charge distribution profiles seen in PMMA will be presented. This study will not attempt to state definitively the exact physics at work, [1] but will piece together the findings of many other investigators to construct a plausible model of the charge dynamics in PMMA using a formalism developed for amorphous semiconductors [2, 47].

---

[1] To quote T.J. Lewis, "It is little wonder that any attempts to understand how electrons can squeeze their way through submicroscopic balls of molecular thread will be fraught with difficulty and indecisive evidence [43]"

A mobility band model proposed by Cohen, Fritzsche, and Ovshinsky (CFO) [47] has been successfully applied to inorganic [2] as well as organic [48] covalently bonded semiconductors. The density of localized mid-gap states can be large enough for a sufficient wave function overlap to allow communication between states. The energy level at which this occurs has an effective extended state band, behaving like a conduction or a valence band [45, 42], defined by the energy at which electrons or holes can hop freely in space with an effective mobility. The energy gap, between a hole and an electron mobility band, is called the *mobility gap* and is directly analogous to the band gap of a crystalline semiconductor.

If an electron receives enough energy from the lattice to be excited from one localized trap into another, that energy perturbation can be expressed as the interaction with a phonon or a combination of phonon-electron interactions. This is the essence of the most widely accepted conduction mechanism considered for polymers known as the *polaron* theory describing the motion of electrons by phonon assisted hops [2, 4, 47]. The communication between hops may or may not require the presence of a mobility band, depending on the proximity of the traps.

Depending on the manufacturer and the forming process used, a variety of charging conditions have been observed by other authors in polyethylene [38]. The PE samples tested with the ESAW experiments contrast with the results of the PMMA samples since the polarity of the internal charge accumulation is opposite that of the PMMA.

Internal charge near the electrodes of the PE samples is consistently of the same sign as the poling voltage. This indicates homocharge injection, which tends to lower the field at the electrodes. The cathode appears to
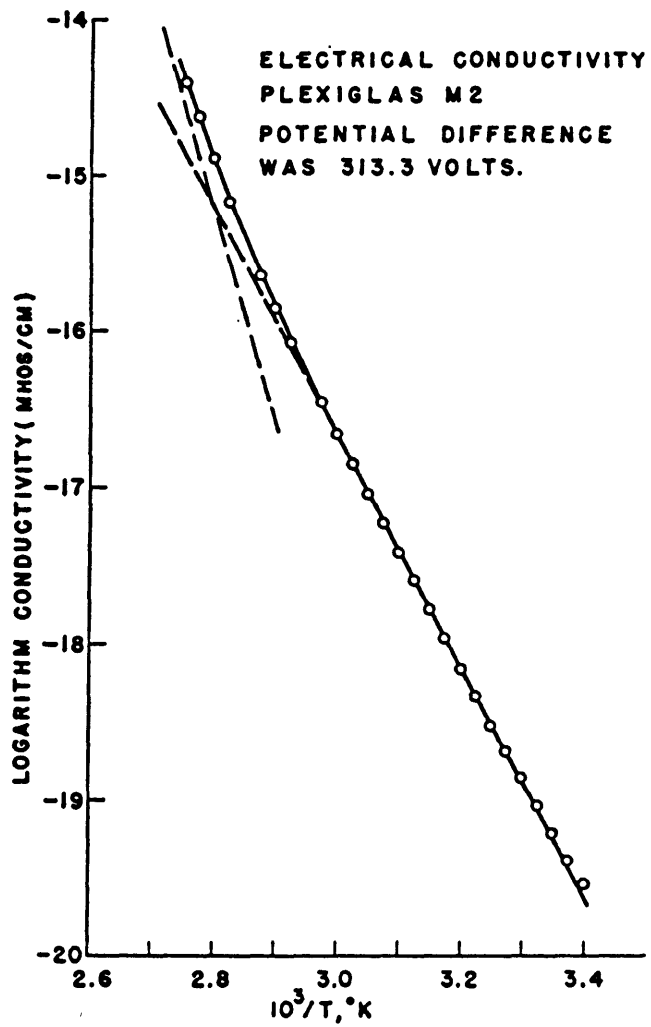
Figure 5.1: Arrhenius plot of electrical conductivity of *Plexiglas* [49]

be more efficient as a charge source than the anode, adding credibility to the assumption that PE is an electron conductor. The charge appears to accumulate within the bulk, suggesting that there is bulk carrier transport in PE, as opposed to PMMA, which shows no noticeable bulk transport. This result will be presented in section 5.2 as evidence for the density of states model of PMMA.

Previous studies of PMMA and PE have concluded that the conduction mechanisms are electronic [48], allowing the simplifications of one carrier species and a single mobility band. It has been determined that the steady state conduction of *Rohm&Haas* PMMA with aluminum electrodes exhibits a single activation energy characteristic, consistent with a polaron theory [2, 48]. This energy was found to be 1.5 eV for temperatures below 70° C, from the Arrhenius plot of Fig. 5.1 [49]. This value will be shown to agree with the PMMA data presented in this work.

As electrons become distributed across the sample, they are trapped in localized states beneath the mobility band edge. The capture probability of a particular trap depends on its relative cross-section. The release probability, on the other hand, is primarily dependent on the depth of the energy beneath the mobility band edge. Thus, one can understand that an electron capture and release are not reversible reactions since both processes require different energies. When trapped electrons are released and recaptured, the distribution of charge and polarization within the sample can be altered. In the absence of charge injection from the contacts, the net charge will be zero, and the space charge can be expressed as polarization gradient.

If only one electrode provides injection, a net charge will result from the imbalance of internal charge. In the situation where polarization and

injection occur simultaneously, the material can accumulate charge until a steady state becomes established. This steady state may be the result of injection from the opposite electrode or by E-field reduction at the surface with the approach of space charge limited conduction. If injection from both electrodes are exactly equal and opposite, the charge will remain zero. This will be distinguished by the sign of the charge profile; whether heterocharge or homocharge are present near the electrodes.

The next section will discuss the polarization mechanisms, illustrating how the charging process may occur by small electron hops. Afterwards, the CFO model will be examined in relation to the defect states in PMMA. This will be used to describe the observed data in terms of band bending, allowing one to model the material as a wide band-gap amorphous organic semiconductor with a distribution of traps.

5.1 Polarization

The polarization under a DC field results in an apparent dielectric response having two components: the instantaneous, uniform, high frequency permittivity ϵ_∞ and persistent, non-uniform polarization distribution which remains after the field has been removed. This is the polarization discussed in section 3.1.1 and can be similarly defined in terms of the residual internal field, E_p, that persists after the poling voltage has been removed

$$P_t = \epsilon_\infty \int_z^d E_p dz = Q_s \tag{5.1}$$

where Q_s is the surface charge imaged at the electrodes under zero bias. The high frequency permittivity is defined as the reversible component of the polarization that does not persist after the field has been terminated.

169

Non-reversible charge distributions, in contrast, may persist long after the poling field has been removed in an insulating material.

5.1.1 Electron Hopping

A general treatment of hopping conduction between localized states has been given by Ieda [45] for electrons in an amorphous insulator. This same approach will be used to describe the materials studied here, which will be considered wide mobility gap amorphous semiconductors containing a distribution of traps. Electrons can be randomly perturbed out of their trapping sites under electrical stress, resulting in a charge distribution. A simplified model presented by Lewis [42] describes the formation of a space charge caused by electron hops between occupied and unoccupied localized sites based on the *Poole-Frenkel* model of thermally activated hops. A Gaussian energy distribution of trapping states is assumed, with filled donor states below and empty acceptor states above the Fermi energy.

The constituent molecules are confined in space by comparison to their associated electrons, which are considered primarily responsible for transport in this model. An amorphous solid, containing a large distribution of acceptor and donor energy levels [2, 42] residing over broadly distributed regions in energy and space, will have a fraction of its localized states thermally ionized. The time dependent perturbation associated with exciting carriers into the mobility band can be attributed to lattice vibrations. These are phonons that can interact with trapped electrons causing hops which are responsible for conduction.

For simplification in applying this model, charge injection at the anode will be ignored and injection at the cathode will be considered to occur only within a narrow layer immediately beneath the electrode as suggested by the

170
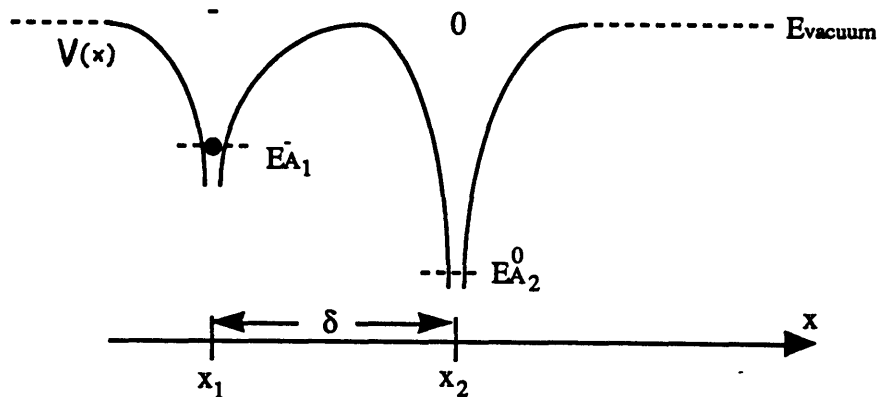
Figure 5.2: Electron hopping pathway through barrier V(x) between a neutral empty acceptor state at energy $E_{A_1}^0$ and a charged filled state at $E_{A_2}^-$ separated by distance δ

figures in Chapter 4. Consequently, the net homocharge will be considered to exist within a monolayer beneath the cathode, canceling the heterocharge in the immediate vicinity.

After the initial poling voltage has been applied, charging currents in PMMA as well as PE are known to decrease over several orders of magnitude with time [45, 51]. Considering the large observed initial charge build-up in PMMA, it can be concluded that the anode contact is consistently more blocking than the cathode. It appears as though the large initial current is dominated by bulk polarization. After the voltage has been applied for some time, the polarization slows down and the external current becomes injection limited. Looking at the PMMA data in chapter 4, the cathode appears to inject negative charge, reducing the heterocharge near the surface while negative charge continues to accumulate near the anode.

Electron current will result from a series of local electron hops between occupied and unoccupied sites. Each event is strongly dependent on the trap occupancy, distance between sites, and the potential distribution. This is illustrated in Fig. 5.2 for an occupied site at x_1 with activation energy $E_{A_1}^0$ near a charged site at x_2, having energy $E_{A_2}^-$, separated by distance δ.

An acceptor state is neutral when empty and negatively charged when filled. In the example of Fig. 5.2, an electron hopping from x_1 to x_2 will produce a current in the opposite direction to the hop. The same event may occur for a pair of donors which are neutral when filled and positively charged when empty. An electron in a neutral trap will decrease its energy by filling a positively charged site. The neutral trap will subsequently become charged as seen in the energy diagram of Fig. 5.2. In this example, the two traps are identical, making the reverse jump equally likely with no applied field.

If the neutral energy of an acceptor at X_1 is higher than the neutral energy of the other at X_2

$$E_{A_1}^0 > E_{A_2}^0$$

then the trap with the higher energy is more likely to be unoccupied (ionized) making the electron thermodynamically stable [2]. A donor impurity having a low concentration in the presence of a large density of donor and acceptor states will be ionized if its charged energy is higher than nearby neutral donor or acceptor levels.

Without an applied electric field, no current will flow since there will be no force on the individual charges to cause drift in one direction in preference to the other. A nearby charged donor state will cause an electric field between the two charges. The distance between sheet charge traps will be considered greater than several molecular spacings, allowing ϵ_∞ to be considered constant and the magnitude of the field between two equal but opposite charges is $\frac{q}{\epsilon_\infty}$, regardless of their separation. This condition is illustrated in Fig. 5.3.

The potential barrier is lowered by $\approx \frac{q\delta}{2\epsilon}$ represented by the field between
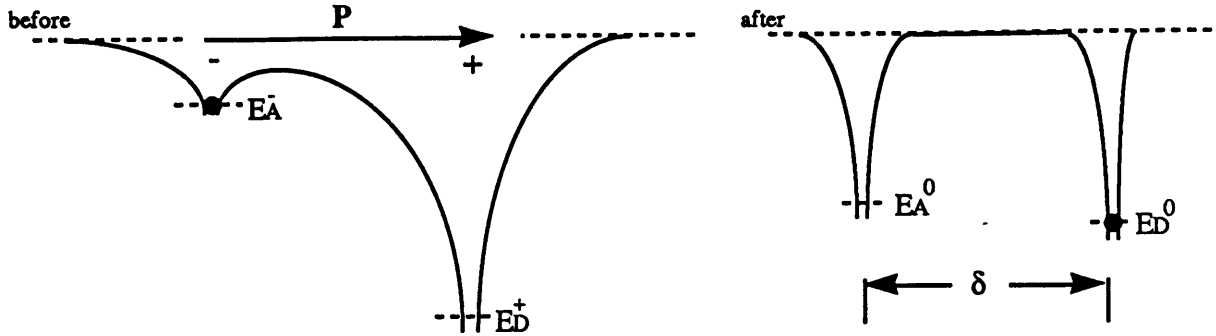
Figure 5.3: A charged donor with energy E_D^+ accepts an electron from a charged acceptor with energy E_A^-.

a charged donor and acceptor states. If the donor gives up its electron to the acceptor, the net result is zero charge and two neutral trapping sites. The capture cross section is also decreased due to the lack of coulomb potential. The donor energy increases and the acceptor energy decreases after the jump establishing two charged energy levels in equilibrium.

The difference in values of the average energy of the neutral and the ionized donor – acceptor pair is called the *correlation energy* [47].

$$U_{corr} = \frac{E_A^- + E_D^+}{2} - \frac{E_A^0 + E_D^0}{2} \tag{5.2}$$

where U_{corr} determines the equilibrium concentrations of charged and uncharged species. If pair of oppositely charged traps are in tunnelling proximity to each other, there is a finite probability that the reverse event will occur. If U_{corr} is positive, the electron will have to increase its energy to return to the charged state. Positive correlated traps are, thus, charge neutral and negatively correlated traps are ionized in equilibrium.[2]

---

[2]This energy is difficult to determine and has been the source of much debate with respect to conduction models in amorphous silicon [2].
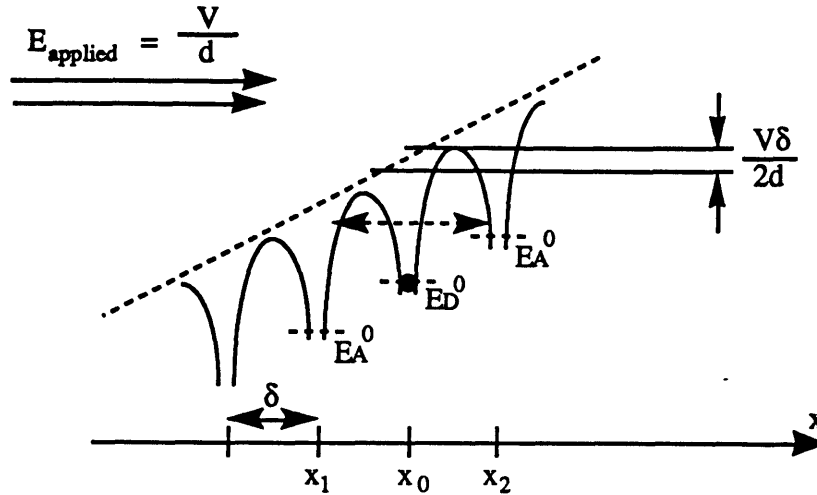
Figure 5.4: A series of neutral donors and acceptors under the influence of a uniform electric field.

A sample that is charge neutral, or has established equilibrium with respect to its charged states, may have dipole moments distributed throughout the bulk due to the presence of negatively correlated traps, even at $0°$ K. Charge neutral material with a distribution of acceptors and donors may, also, have a finite number of ionized traps due to the Fermi distribution of occupied sites within the band gap at finite temperatures. Charged traps have a much larger capture cross section than neutral traps, making them very likely to capture mobile charge carriers. The presence of charged traps has a pronounced effect on the transport of charges in the mobility band.

Electrons residing in traps may receive enough energy from an applied field to hop in the direction opposite the field. Once a hop has occurred and the electron is free, it will become captured again by a nearby trap. If this happens randomly across the sample, a distribution of localized charged will result. This hopping process occurs in the direction which tends to lower the bulk field, increasing the overall bulk polarization in the direction of the applied field. The resulting charge distribution appears in the form of a polarization gradient distributed across the sample; although, the charges

174

are actually trapped in localized sites. Once a single hop has occurred, the reverse event is not as likely after the field is removed since the secondary trap will have a high probability of residing at a different energy.

To demonstrate this phenomenon, a series of initially charge neutral traps is shown in Fig. 5.4. An electron trapped in an acceptor site at x_0 may hop to either of the adjacent neutral neutral donor sites under zero bias with a probability p_0. The applied field lowers the potential barrier for a jump to x_1 and raises the barrier for x_2 by

$$\Delta \Phi_{barrier} = \frac{V\delta}{2d}$$

for an applied voltage, V, across the sample of thickness d. The total barrier height change on either side is approximated by assuming symmetric potentials, equally spaced by δ.

These transitions can be approximated by classical thermionic hopping, whereby, the probability of a transition from x_0 to x_1 increases inversely with the probability for the opposite transition by

$$p^+_{0 \to 1} = p_0 e^{\frac{+q\Delta\Phi}{kT}} \text{ and } p^-_{1 \to 0} = p_0 e^{\frac{-q\Delta\Phi}{kT}}$$

where p_0 is the transition probability, equal to the inverse transition rate. These two relations allow one to approximate the ionization current density as

$$J_q(E) = q\delta\sqrt{N^0_D N^0_A}\, p_0\, sinh\left(\frac{-q\delta E}{2kT}\right) \tag{5.3}$$

where N^0_D and N^0_A are the effective unionized donor and acceptor concentrations. If the dominant mechanism is tunnelling, this current will depend on the complete tunnelling matrix element between these two states [42] and the conduction may be better described by a *Mott* variable range hopping

175

model [2, 47]. If there is a lack of either donors or acceptors, there will be a net effective charge, so the ionization current depends on a set of neutral donors and acceptors ionizing in the presence of other neutral traps.

A distribution of electron hops in space originating from a distribution of sites in energy can produce a charge profile maintaining overall charge neutrality. To address the random nature of this hopping model, a density of trap states distribution has been suggested by Fabish and Duke [50] which is similar to the distribution assumed by Lewis [42] and can lead to a polarization gradient. Both studies assume a Gaussian distribution of neutral trap and donor states within a wide energy gap.

The next section will build an approximate room temperature energy distribution of single electron traps based on the research presented in publications of UV absorption, X-ray spectroscopy, time resolved current, and contact charge exchange experiments. An energy band structure based on the CFO model will then be shown to explain the observed data from the time resolved ESAW experiments.

5.2 Band Model

The physical structure of a polymer is largely determined by the chemistry of its constituent monomer. By comparing the repeated molecules making up polyethylene (PE) and poly(methylmethacrylate) (PMMA) shown in Fig. 5.5, it becomes apparent that differences in their electrical behavior may be attributed to the presence of oxygen bonds. PE tends to form rigid crystallites by aligning their chains to one another. Energy bands of crystalline PE have been determined [1, 4] and applied with limited success to the electrical behavior of fabricated materials [53]. The electrical prop-

176

Polyethylene (PE)

$$\left(\!\!- CH_2 - CH_2 -\!\!\right)$$

$$\begin{array}{c}CH_3\\|\\\left(\!\!- CH_2 - \overset{\displaystyle|}{\underset{\displaystyle|}{C}} -\!\!\right)\\C = O\\|\\O\\|\\CH_3\end{array}$$

Poly(methylmethacrylate) (PMMA)
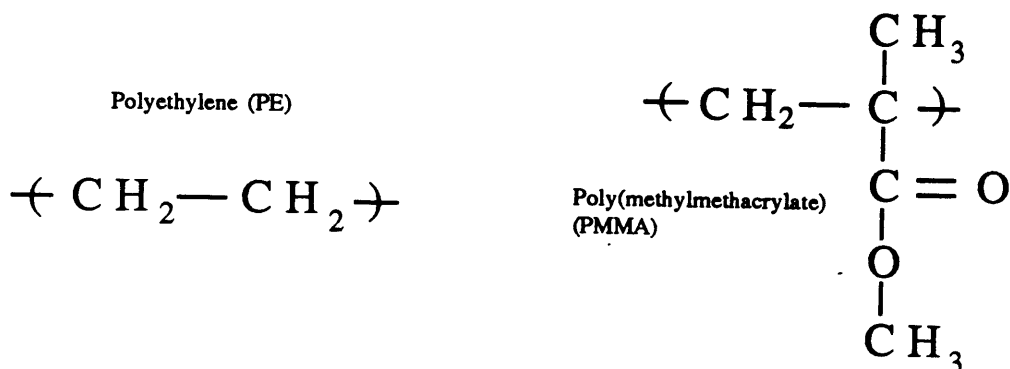
Figure 5.5: Chemical structure of the constituent monomers for polyethylene and poly(methylmethacrylate)

erties are mostly attributed to impurity concentrations introduced during polymerization and extrusion. The deviations of results between different samples are, thus, understandable [38]. Consequently, this analysis will concentrate on the properties of PMMA which is known to produce consistent results from one sample to the next [54].

5.2.1 PMMA Chemistry

The persistence length, λ_p is the average length of a molecular chain as measured by X-ray spectroscopy. Many polymers have been characterized by this length which is a measure of the relative amorphousness. A persistence length that is much larger than an individual molecule has a high tendency to become polycrystalline, while a short λ_p indicates a more random solid.

PMMA has been shown to have a characteristic persistence length

$$\lambda_p = 0.8 \; nm$$

which smaller the molecular size. Such a small persistence length assures that the polymer has a *wormlike* character being completely amorphous [56].

When PMMA is fabricated, the molecular chains automatically form in completely random configurations, assuring a lack of crystallinity. The material is always found to be amorphous and generally homogeneous over any macroscopic dimensions. It has been shown to have consistent chemical properties regardless of the manufacturing conditions or its form; either as a solid or as a powder [54].

Due to the flexible nature of a molecular chain and its subsequently large number of energetic configurations, the natural amorphous state has a number of incomplete bonds and a large variation of bond angles between molecules [2]. The energies associated with these variations result in a distribution in the density of bonding and anti-bonding electronic states associated with the individual carbon-carbon and carbon-oxygen bonds [57]. The result is an equilibrium density of free radicals. Assuming no charges were introduced during processing, the material will be charge neutral, so the concentrations of anions and cations will be equal.

The electron energy absorption spectrum between 5 and 13 eV has been determined to result from the pendant atoms [58]. However, a smaller peak at 4.2 eV exists, in agreement with the energy separation found by Fabish and Duke [50]. This low energy peak is small by comparison to the molecular density, relating it to a concentration of broken and incomplete bonds.

The chemical analysis of PMMA via x-ray and electron beam studies do not give an accurate electronic picture of the valence electrons and the effective energy gap since the energy is too large. Lower energy optical absorption can probe the concentrations of states within the bandgap. The density of states observed by absorption of ultra-violet (UV) and lower energy radiation can give an approximate density of localized states to combine

178
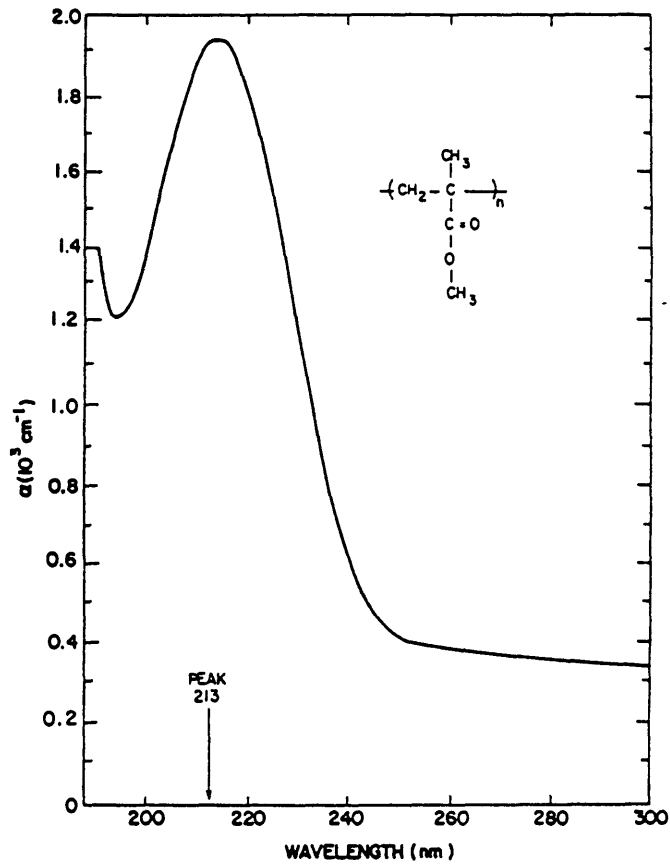
Figure 5.6: UV absorption coefficient of a 10.4 μm film of PMMA [58]

with results from electrical tests.

5.2.2 Optical absorption

PMMA has found applications in microelectronics as a photomasking material because it is sensitive to UV light, motivating a great deal of interest in its photo-absorption properties [55]. Fig. 5.6 from Ritsko et.al. [58], shows an optical absorption spectrum of a 10.4 μm thick sample of PMMA. This spectrum agrees well with other authors [55, 57]. The peak at 213 nm cor-

responds to 5.8 eV. The absorption at energies as low as 4.1 eV is 20% of the peak value, suggesting that there is a large density of localized states distributed across the gap.

By assuming PMMA is a wide gap semiconductor with a distribution of trapping states, the ultra-violet absorption spectrum can be related to the energy distribution of filled and empty states. These states can then be compared to approximate levels of filled and unfilled electronic states [52]. Due to the variety of possible energy levels associated with the bond angles within an amorphous network, the band tails can be as wide as a several eV. The presence of neutral donors and acceptors has been confirmed by Lewis [42]. The occupancy of these states determines the position of the equilibrium Fermi level (E_{f0}) at the point which maintains charge neutrality.

The random nature of the polymer allows one to consider bulk defects as being continuous to the surface. This allows the determination of mid-gap states by measuring the concentrations of available carriers near the surface [4]. Using a variety of metal probes made of different work functions on various thicknesses of PMMA, Fabish and Duke [50] have experimentally determined values for the mid-gap density of donor and acceptor states. Their result is shown in Fig. 5.7 where it is clear that a reasonably large concentration of electronic traps appear throughout the energy band.

The *squared off* region is the experimental data determined by the charge remaining on the material surface after reaching equilibrium with the electrode. Gaussian curves are fit to the profile resulting in an energy separation between peak anion (acceptor) and cation (donor) levels of 4.1 eV. The centroid is at -4.1 eV below the vacuum level indicated by the zero of energy. This result may be combined with the UV absorption spectrum to estimate
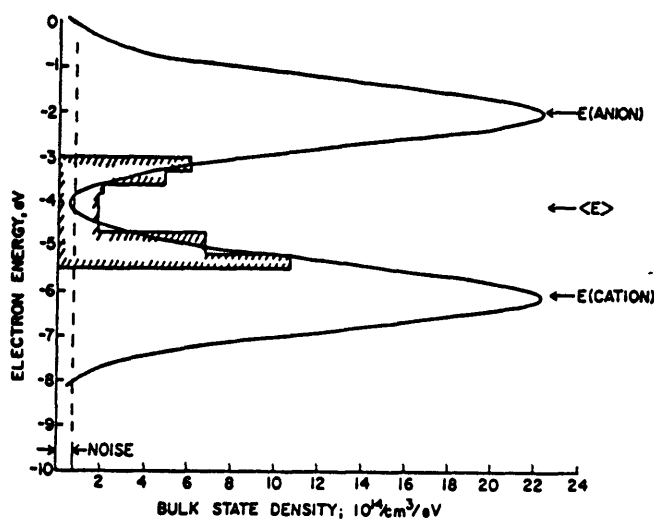
Figure 5.7: Gaussian representation of the solid-state anion and cation state distribution for PMMA [50].

the quantitative density of states shown in Fig. 5.8, for PMMA at room temperature. This picture is likely to be temperature dependent as the glass transition temperature is approached.

The demarcation energies, $E_{\mu n}$ and $E_{\mu p}$, are defined as the energies at which the critical density of states, g_μ, is achieved for electrons and holes allowing band conduction to occur. At these energies, the density of localized states is large enough for communication across the whole sample in the form of an extended state [47]. Neutral donors near a mobility energy, $E_{\mu n}$, can have their electrons excited into an extended state, with little activation energy. Carriers trapped in levels whose energies are farther from a mobility edge require more energy to be excited into the extended states, causing them to remain trapped for longer times. The occupation of electrons in deep states are determined by Fermi statistics; therefore, the largest concentration of charged carriers will exist near the Fermi energy as depicted in Fig. 5.8.

181
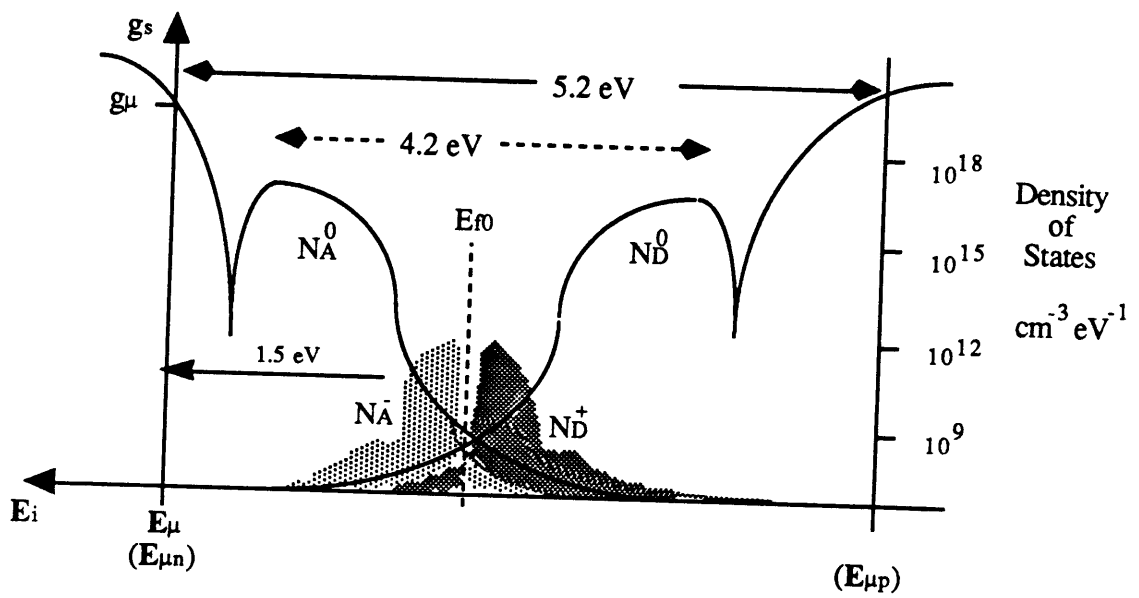
Figure 5.8: Density of states showing energies with respect to the electron and hole mobility edges, $E_{\mu n}$ and $E_{\mu p}$.

5.2.3 Mobility Model

The relative position of the Fermi level to one of the band edges determines dominance of either electrons or holes. Hole conduction has been observed in many polymers [45]; however, only electron conduction has been observed in both PE and PMMA [45, 48]. For the remainder of this discussion, only the electron mobility edge will be considered and the n subscript of the mobility band edge will be assumed.

The density of states diagram shown in Fig. 5.8 shows the approximate demarcation energy level E_μ in relation to the assumed density of states diagram. The equilibrium Fermi level, E_{f0}, is at approximately 2 eV below the mobility edge, allowing an approximation for the density of ionized acceptors to be made. One can assume that the molecular density is the density of available sites ($10^{20} cm^{-3}$) giving the number of ionized acceptors at the mobility edge

$$N_A^- \approx N_{mol} e^{-\frac{(E_\mu - E_{f0})}{kT}} = 10^{-14} \approx 0 \ cm^{-3}$$

or, that no carriers are available for conduction at any instant in time.

Excess electrons are not stable in this mobility band. An electron-phonon pair may have enough energy to reside at the mobile energy long enough to communicate with surrounding traps. The electron will not be in thermal equilibrium at that energy, thus, it can only survive in that state for a very short time. The electron will then be trapped by a local site, bringing it to a lower energy. One can describe the hopping process as occurring with the excitation of an electron to the mobility band. Each time an electron is excited into the band, the actual time spent in motion is negligible. Therefore, the effective mobility is described as a polaron mobility for short range

183

electron hops between local sites.

Once an electron is excited into the mobility band, either by a single phonon or a sequence of phonon excitations, it will be captured almost instantaneously. The capture probability is proportional to the cross section and the density of available states. Even though the positive charges remain at much lower energies, they are available to capture mobile electrons with a larger capture cross section than uncharged traps. If the contacts are blocking to electron injection, an applied field will diminish the electron concentration near the cathode while other electrons tie up charged donors near the anode. This process is shown schematically in Fig. 5.9.

The availability of carriers which can participate in conduction is exponentially increasing towards the electron quasi-Fermi level, F_n, which is equal to the equilibrium Fermi level, E_{f0}, in unpoled material. The occupancy of the mid gap states is determined by their proximity to F_n, producing the distribution of charged states shown in Fig. 5.8. The electron concentration decreases exponentially for energies approaching the mobility edge, where no electron concentration is thermally stable at room temperature.

Deeper traps within the gap, below the mobility energy, have exponentially longer time constants associated with their emission probabilities. Consequently, the small but finite concentration of charged acceptors above some energy level W will be quickly excited into extended states while traps with lower energies will only respond after longer times. This is the effective activation energy for a steady state conduction and will be shown to be ≈ 1.5 eV, as seen in Fig. 5.9(a) with a voltage initially applied.

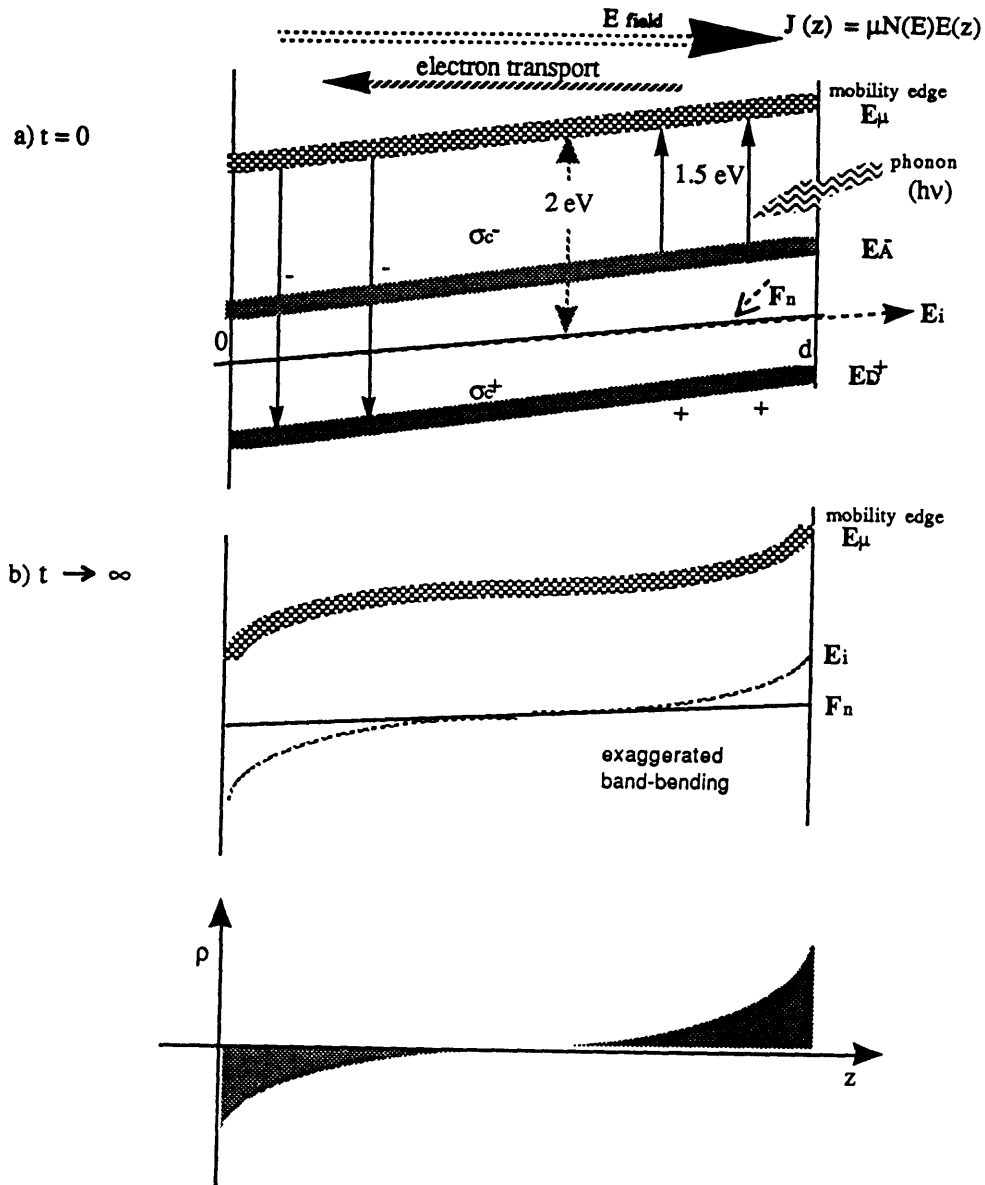A single electron Fermi level, F_n, describes the extended state occupancy

184

Figure 5.9: Band diagram showing electron emission near the anode and capture near the cathode resulting in a net polarization under conditions of a) no accumulated internal charge and b) steady state conditions with its corresponding charge density.

in non-equilibrium conditions and a distribution of quasi-Fermi levels correspond to the distribution of trapped electrons below that energy. This becomes the driving force to separate charge under bias. After the voltage has been applied to the sample, all the bands shift under constant field. The internal charge density is zero at first and conduction results from electron drift from states closest to the mobility band.

Shallow traps will first be excited into the mobility band forcing the Fermi level to shift up. However, deep traps cannot respond fast enough to follow the shift in F_n, generating an inherently unstable condition on the electron energies. Electrons tie up local positively charged traps. A charge distribution will develop as the bands bend to compensate the tendency for the electron quasi-Fermi level to *flatten out* as a result of the decrease in current density.

A space charge distribution will initially develop quickly in time, as the shallow electrons respond. The change will slow down as the bands bend due to the modified electric field

$$\frac{\partial E}{\partial z} = \frac{\rho_q(z)}{\epsilon}$$

This spatially varying charge density appears as if it were due to a polarization gradient across the sample which persists after the field is removed. The steady state energy diagram is shown in Fig. 5.9 b) above its resulting charge density distribution. This profile agrees with the form of the time resolved charge profiles in chapter 4, describing the observed profiles.

The resulting charge density profile is related to the difference between equilibrium Fermi energy E_{f0} and the electron quasi-Fermi level F_n by the trap concentration. A displacement between these two levels is reflected in the ionized donor and acceptor concentrations. This is represented in

186
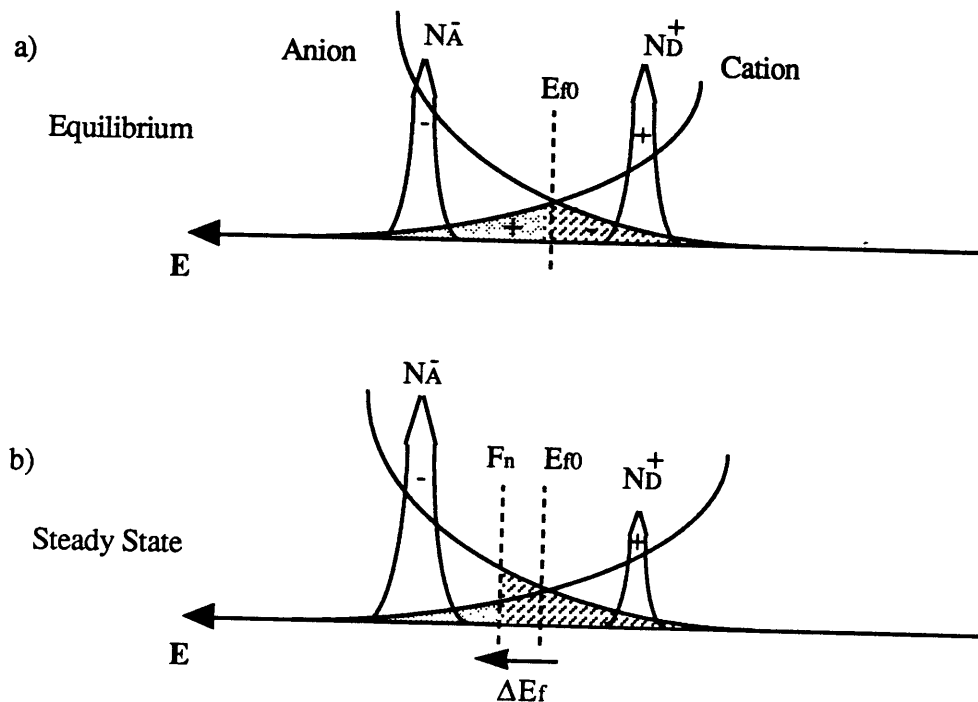
Figure 5.10: The effect of the electron Fermi level on charged donor and acceptor concentrations under a) equilibrium conditions where the sample is charge neutral and b) steady state where the shifted quasi-Fermi level produces a negative charge.

Fig. 5.10 where the steady state quasi-Fermi level in (a) is raised in energy from equilibrium, as seen in (b). The result is an increased population of negatively charged acceptors and a decreased population of positively charged donors.

This agrees with the band bending principle of crystalline semiconductors where the negative charge increases as the bands are bent toward the Fermi level. In this example, the charges are not located in the band tails, but are deep within the energy gap. The excess charges can only participate

187

in conduction after interacting with sufficiently energetic phonons, incrementally polarizing the material across the sample.

The energy of the charged carriers can be approximated by assuming the available charge density has the form

$$\rho_\mu(z) = \rho_0(z)e^{-\frac{W}{kT}}$$

allowing the current to be related to the field (ignoring diffusion) with the relation

$$J(z) = \mu_{band}e^{-\frac{W}{kT}}\rho_0(z)E(z) \tag{5.4}$$

where E is the electric field. In this model, the mobility is assumed constant while the density of available carriers increases with temperature. The exponential term from the carrier concentration with activation energy, W, can be combined with the band mobility, to give an apparent thermally activated mobility. An activation energy can be measured through an Arrhenius plot, as observed by Munick in Fig. 5.1 [49].

The time rate of change of the charge density at any point z can be found through charge conservation

$$\frac{\partial\rho(z)}{\partial t} = -\mu e^{-\frac{W}{kT}}\frac{\partial}{\partial z}\left[\rho(z)E(z)\right] \tag{5.5}$$

and is observable from the charge density profiles, resolved in time and space. This is solved numerically by producing two plots of each set of data: a time resolved charge profile and a plot of ρE for every point in z.

PMMA has a well established glass transition temperature of 105° C [54]. At temperatures approaching T_g, the energy diagram my be modified due to the increased disorder. The phonon density will be substantially increased which would have the effect of providing a larger conductivity. Either or

both of these changes may be the cause of the higher activation energy slope as seen in Fig. 5.1.

Munick [49] has observed an increase in the bulk conductivity at temperatures higher than 70° C above the extrapolated straight line on an Arrhenius plot giving an activation energy of 1.5 eV. His data can be compared with the 90° C space charge profiles in chapter 4 suggesting the dominant conduction mechanism is injection limited at lower temperatures, changing to space charge limited current near the glass transition temperature. Observing the space charge density also allows one to see the effects of traps being excited and retrapped under the influence of an applied field.

5.3   Analysis

To estimate the effective band mobility, μ, from the time resolved data, two extra plots must be provided in addition to the charge profile; $\frac{\partial \rho}{\partial t}$ and $\frac{\partial}{\partial z}[\rho E]$ for every point in z. Then the value for

$$\mu = \mu_{band} e^{-\frac{W}{kT}} = \frac{\frac{\partial \rho}{\partial t}}{\frac{\partial}{\partial z}[\rho(z)E(z)]}$$

where μ is the effective temperature dependent band mobility which can be determined for every temperature. This result is the same as for the activation energy polaron model described earlier.

A derivative of the $[\rho E]$ plots in the straightest region within the sample is used to find the average bulk mobility μ. The errors associated with this measurement must also be considered due to the system noise. The total error is determined by assuming

$$\mu \approx -\frac{a = \frac{\partial Q}{\partial t}}{b = \frac{\partial QE}{\partial z}}$$

189

PMMA poled at 50 C
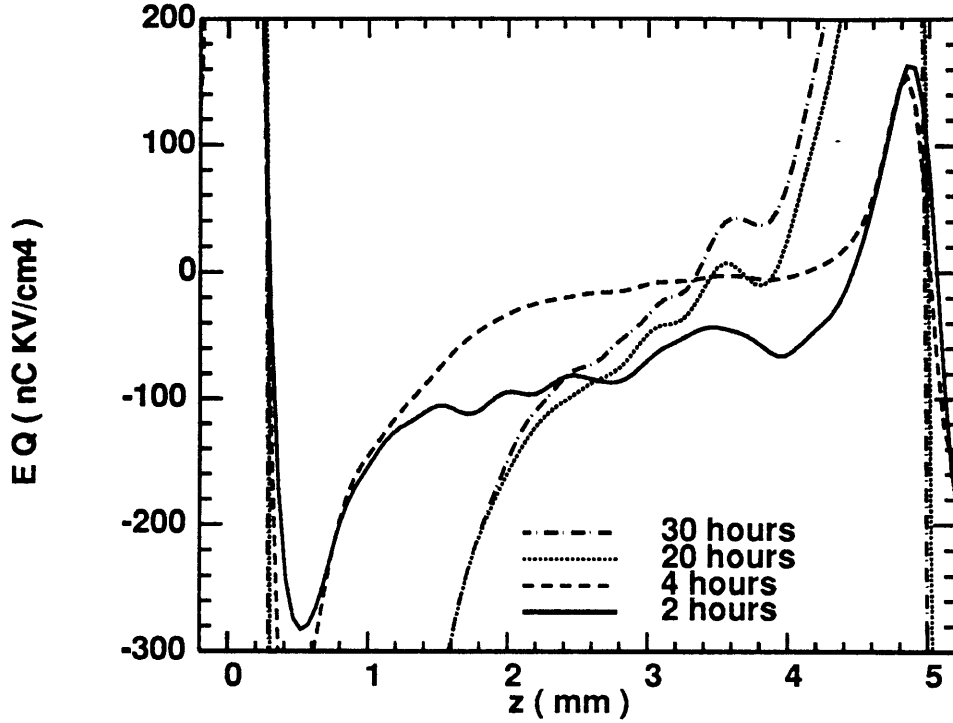
Figure 5.11: QE product of sample in Fig. 4.2.

where the errors in a and b give the error in μ by the relation

$$\Delta\mu = \frac{\partial\mu}{\partial a}\Delta a + \frac{\partial\mu}{\partial b}\Delta b = \sqrt{\left(\frac{\Delta a}{b}\right)^2 + \left(\frac{a\Delta b}{b^2}\right)^2}$$

Samples poled at temperatures below $90°$ C show blocking behavior at the cathode, leading to a bulk polarization with very little external current in the steady state. This can be demonstrated for the sample poled at $5KV$, shown in Fig. 4.2. The QE and $\frac{\partial Q}{\partial t}$ plots are shown in Figs. 5.11 and 5.12.

The time rate of change of the bulk charge becomes too close to zero for times greater than 2 *hours*. But, a value for all three parameters can be found from these two curves and from Fig. 4.2 at $z = 2$ *mm* within the

PMMA poled at 50 C
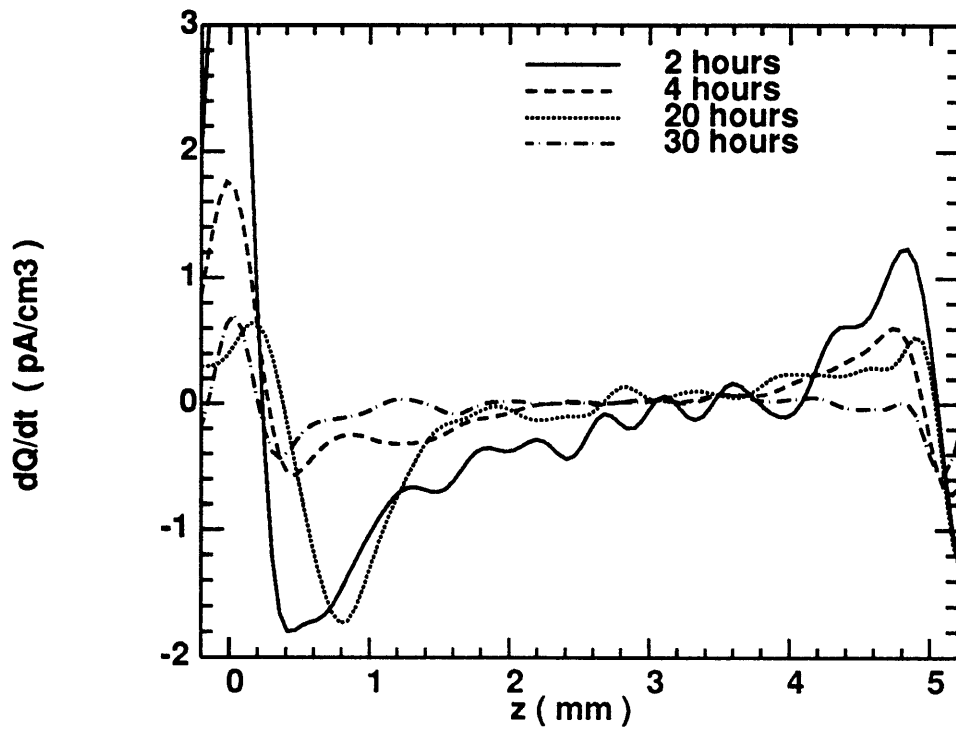
Figure 5.12: $\frac{\partial Q}{\partial t}$ of sample in Fig. 4.2.

sample after 2 hours.

$$\frac{\partial Q}{\partial t} = 0.3 \pm 0.1 \ \frac{pA}{cm^3}$$

$$\frac{\partial}{\partial z}[QE] = 270 \pm 30 \ \frac{KVnC}{cm^5}$$

and

$$\frac{\partial^2 Q}{\partial z^2} \approx 0$$

resulting in a mobility at 50° C

$$\mu_{50°} = +1.1 \pm 0.4 \times 10^{-9} \ \frac{cm^2}{Vsec}$$

for early times, where the second derivative is too small to detect.

At later times when the second derivative is much larger in the bulk, $\frac{\partial Q}{\partial t}$ is too small. Hence, there seems to be a limit to the accuracy one can determine D and μ simultaneously. The resolution of this data is not sufficient to measure the Einstein relation directly, since the thermal potential is on the order of $30mV$ and the potential across the sample is $5KV$, 5 orders of magnitude larger.

The mobilities were determined for the other two fields at $50°C$ poling for comparison, and found to be within a factor of 2 of the value obtained at $5KV$. Similarly, the mobility at 40° C was found

$$\mu_{40°} \approx 1 \times 10^{-10} \frac{cm^2}{Vsec}$$

These numbers are even more approximate than the 50° C data obtained earlier, but the temperature dependence is consistent with a thermionic hopping model.

5.3.1 Virtual Cathode Analysis

The virtual cathode experiments can be used to determine limits within which electrons can be considered to contribute to the conduction process. The same method for determining the mobility will be used; however, this mobility will be compared to the motion of the implanted electrons.

The excess electron concentration resides in trap states, some of which can be attributed to the radiation energy. Once the mobility has been determined using the slope of QE,[3] and the field has been established, the velocity can be approximated from the average field and mobility

$$v_{electron} \approx \mu \bar{E}$$

across the sample. This velocity can then be compared with the velocity of the embedded electron concentration.

Looking at the charge profiles in section 4.2, the charge layers don't appear to move as much as the bulk charge distribution, giving an upper bound on the velocity of these implanted electrons. After the first 20 minutes in the $60°$ C virtual cathode test shown in Fig. 4.13, the peak remains at $1.5mm$, to within about $0.1mm$. This would limit the velocity to

$$v_{e60°} \leq \frac{0.1mm}{100min} = 1.6 \times 10^{-6} \frac{cm}{sec}$$

from 20 to 120 *minutes* while the average E-field is approximately $23\frac{KV}{cm}$ resulting in a maximum mobility at $60°$ C

$$\mu_{e\ 60°} \leq 7 \times 10^{-11} \frac{cm^2}{Vsec}$$

for electrons trapped in the PMMA sample.

---

[3] ρ and Q are used interchangeably since the plotting program is unable to draw greek letters.

Virtual Cathode at 60 C
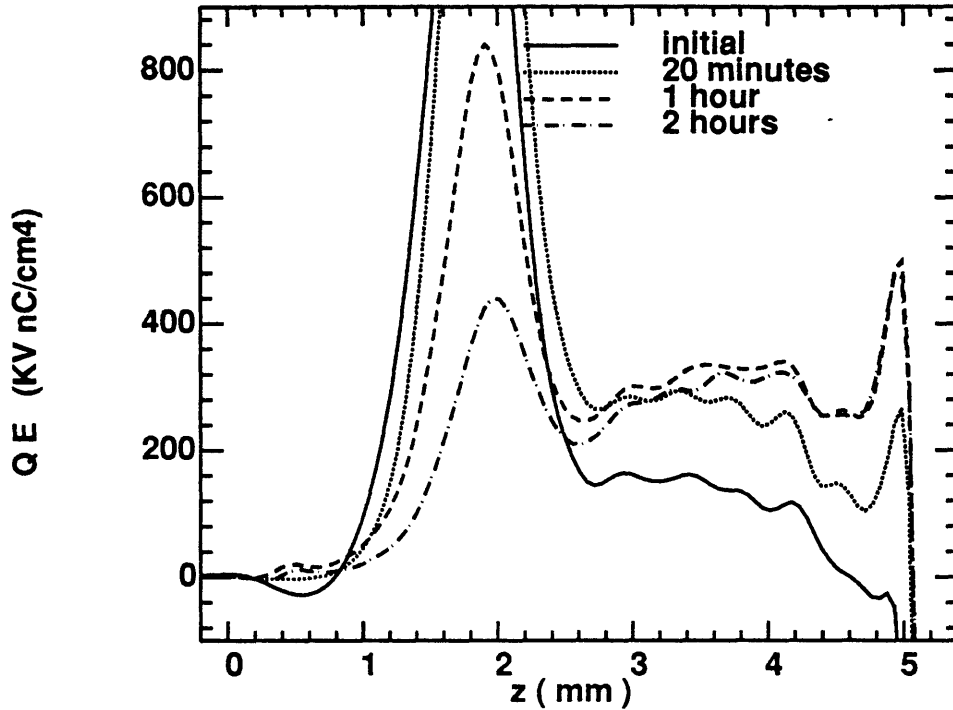
Figure 5.13: $-QE$ product of sample in Fig. 4.13

The same limit can be found for the $20°$ C sample. The profile did not drift any detectable amount between 5 and 20 *days*. The bulk E-field remained constant at about $3\frac{KV}{mm}$ limiting the mobility at room temperature

$$\mu_{e\ 20°} \leq 3 \times 10^{-13}\frac{cm^2}{Vsec}$$

for implanted electrons residing in bulk traps. These mobility values are limits of electron drift. Neither concentration seems to shift in position; hence, most of the implanted electrons reside in deep traps with long residence times.

By assuming the virtual cathode is the actual cathode, the bulk carrier

Virtual Cathode at 60 C
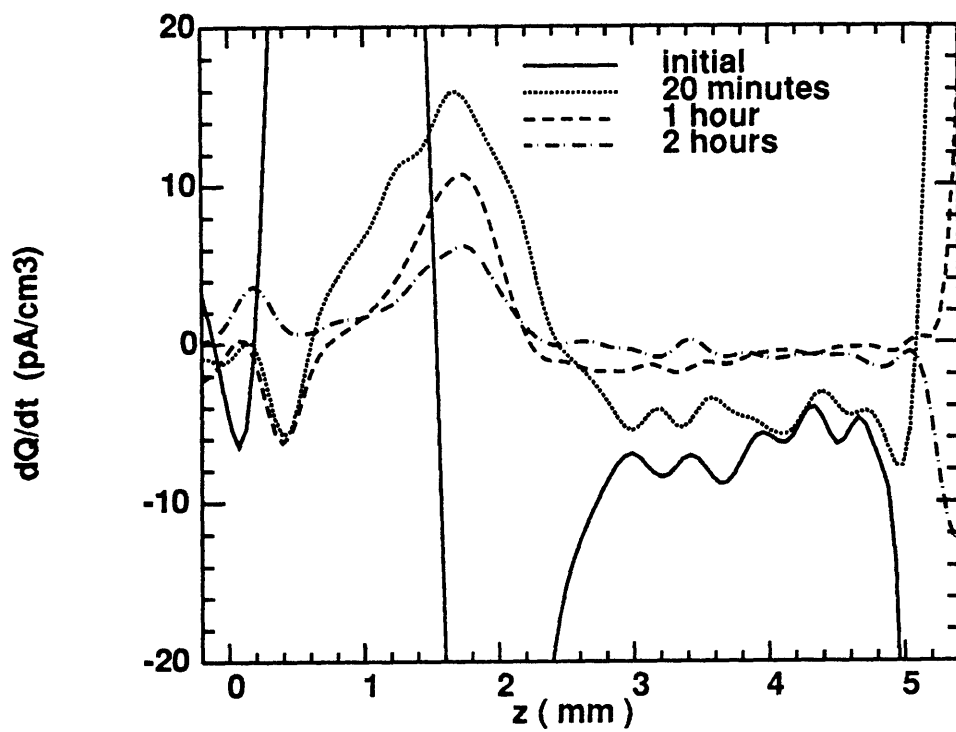
Figure 5.14: $\frac{\partial Q}{\partial t}$ of sample in Fig. 4.2.

mobility can be approximated by the same method as the poled samples. This has been done by plotting QE and $\frac{\partial Q}{\partial t}$ verses z as shown in Figs. 5.13 and 5.14 for the 60° C virtual cathode experiment.

Taking the slope at $z = 3.8mm$ for both the initial and 20 *minutes* profiles gives $-890 \pm 60 \frac{KVnC}{cm^5}$ while $-\frac{\partial Q}{\partial t} = 5 \pm 2 \frac{pA}{cm^3}$ for a bulk mobility

$$\mu_{60°} = 6 \pm 2 \times 10^{-9} \frac{cm^2}{Vsec}$$

in the 60° C virtual cathode sample. Similarly, the room temperature sample has been found to have a bulk mobility of

$$\mu_{20°} = 2 \pm 1 \times 10^{-11} \frac{cm^2}{Vsec}$$

Both of these mobility values are two orders of magnitude larger than their respective maximum trapped electron mobility. This supports the previous assumption that the bulk conductivity is limited by the availability of charge carriers, not the mobility of free electrons. This is equivalent to a model which accounts for electrons residing in traps, spending a negligible time in transport between localized sites.

Activation Energy

Fig. 5.15 is an Arrhenius plot of the measured mobilities, at 60° C and below, versus the inverse absolute temperature. The slope of this curve results in an activation energy for the carrier hopping process

$$E_{act} \approx 1.5 \pm .3eV$$

and agrees with Munick [49] for the steady state activation energy. The result of this agreement is that in steady state, the conduction process is

196

Arrhenius mobility plot
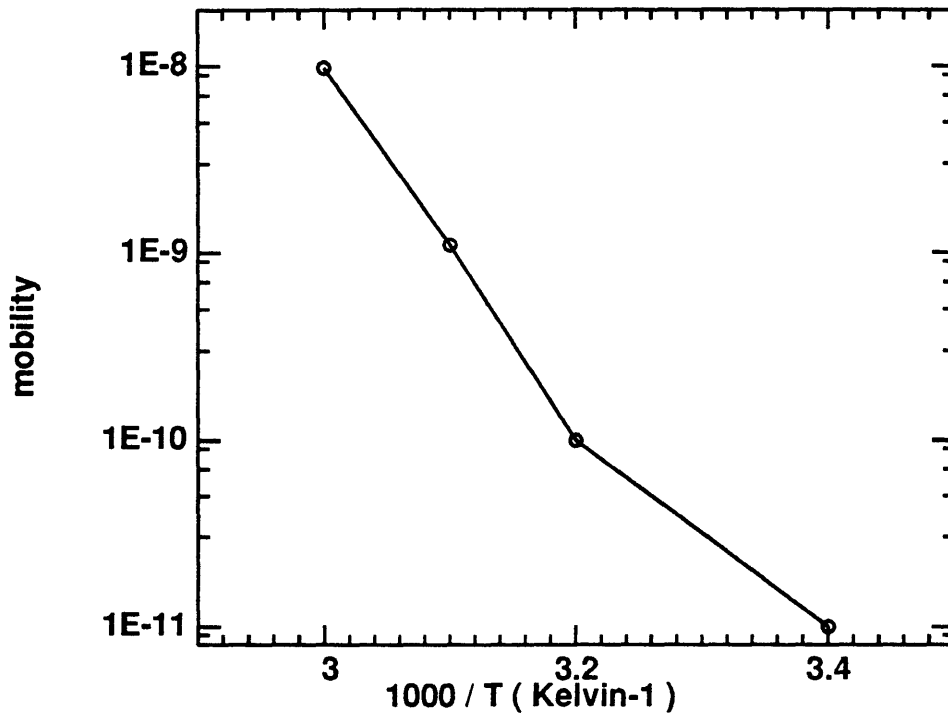
Figure 5.15: Arrhenius plot of mobility and sample temperature.

limited by the activation of locally trapped electrons into an effective conduction band, supporting the polaron band model.

The nearly steady state charge distribution is probably due to the activation of trapped electrons into the mobility band where they will be immediately recaptured by other local traps. The carrier density can be approximated from the rate of change of the charge decay with the mobile charge density n_μ, by assuming

$$J_{drift} = q\mu n_\mu \bar{E} \tag{5.6}$$

where q is the elementary electronic charge. The drift current leading to a net $\frac{dQ_s}{dt}$ is the bulk drift current J_{drift} where Q_s is the total sheet charge at the virtual cathode.

At 60° C, the initial net charge decay is approximated by the slope of the net charge decay curve of Fig. 4.14

$$\frac{dQ_s}{dt} \approx 0.46 \frac{pA}{cm^2}$$

with an average E-field

$$\bar{E} \approx 40 \frac{KV}{cm}$$

resulting in an approximation for the bulk conductivity

$$\sigma_{bulk} = q\mu_b N_b \approx 1.2 \times 10^{-17} \frac{\mho}{cm}$$

This can be compared with the radiation enhanced conductivity found in section 4.2 for the 60° C virtual cathode experiment $\sigma \approx 1.5 \times 10^{-16} \frac{\mho}{cm}$, a factor of approximately 10 higher. The results agree well with previously published data for the bulk conductivities in PMMA [49, 59].

The approximate contributions of the mobility and the carrier concentration to the conductivity will be determined next. The 60° C virtual cathode

198

experiment gives an approximation for the carrier mobility by noticing how far the peak charge moves. The measured maximum mobility

$$\mu \approx 7 \times 10^{-11} \frac{cm^2}{Vsec}$$

is compared to the *effective* 60° C mobility, measured to be $6 \times 10^{-9} \frac{cm^2}{Vsec}$. The exponential term, as a separate quantity from the carrier concentration and mobility, with $W = 1.5\ eV$

$$e^{-\frac{W}{kT}} \approx 2.2 \times 10^{-23}$$

resulting in the pre-exponential term for the temperature dependent conductivity at 60° C

$$n_0\mu_{band} = \sigma_{60°}e^{\frac{W}{kT}} \approx 5 \times 10^5 \frac{\mho}{cm}$$

This yields a lower bound on the bulk carrier concentration in equilibrium

$$n_0 > 5 \times 10^{15}cm^{-3}$$

demonstrating that the bulk carrier concentration overwhelms the implanted charge concentration, making the profile essentially frozen in the time frame of the experiment.

5.3.2 Equilibrium Charge Density

The charge densities in the bulk of the virtual cathode experiments at both 20° C and at 60° C indicate that a quasi-equilibrium concentration of $\approx -30\frac{nC}{cm^3}$ develops for short times. The build up appears nearly uniform across the unirradiated region and settles out in the first two hours of the 60° C experiment before falling off like the other poled samples.

PMMA at 90 C with 5 KV
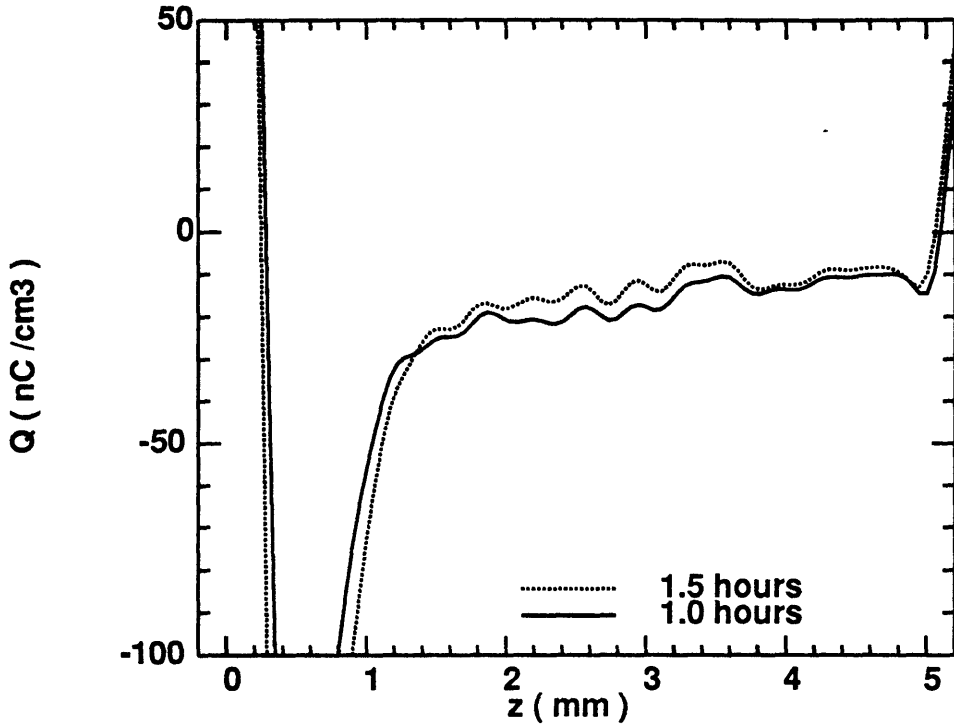
Figure 5.16: Expanded view of two traces from Fig. 4.3 to show the small bulk charge concentration.

This is easily explained by the small concentration of ionized electronic charge at energies less than 1.5 eV below E_μ. This concentration depends on the presence of negatively correlated traps and the ionized acceptors from the tails of the Fermi level. The charge density nearest the mobility edge will be excited with a very small energy and recombine with positively charged sites. The total number of carriers is measured to be

$$n \approx \frac{30\frac{nC}{cm^3}}{1.6 \times 10^{-10}nC} \approx 2 \times 10^{10} cm^{-3}$$

This number can be compared with the data observed at 90° C in

200

Fig. 4.3, which has been expanded in Fig. 5.16 to show the detail in the center. After 1 and 1.5 *hours*, the charge concentration is just under $30\frac{nC}{cm^3}$, consistent with the virtual cathode data. Therefore, within a factor of about 2 or better, the equilibrium density of shallow traps has been determined.

5.3.3 Injection

The barrier to electron emission at the anode increases with temperature and field, while the barrier to injection at the cathode decreases. This phenomenon is consistent with *anodization* of the metal contact. The samples were placed under bias in air, where oxidation can occur at the anode.[4] Similarly, reduction may be taking place at the cathode, tending to remove any oxide layer. This would be consistent with the simple chemistry of two electrodes under bias in the presence of oxygen. In order to tell for sure what is taking place at these interfaces, a careful chemical analysis would have to be performed and is beyond the scope of this investigation.

Excess oxygen will build up an Alumina barrier, separating the metal from tunnelling sites within the insulator. Other effects which can not be measured using ESAW profiling may be taking place. Cathode reduction should have the opposite effect by allowing a reduction of the barrier to conduction through deep states, leading to the asymmetric profiles of samples poled at temperatures greater than 50° C.

The barrier to conduction reduces the steady state current, forcing the electron quasi-Fermi level to become nearly flat across the sample. Since a large equilibrium charge exists within the sample, the bands bend around the nearly flat equilibrium level as seen in Fig. 5.9b. A small slope will be

---

[4]The anode is defined as the electrode where oxidation takes place and the cathode is where reduction takes place [35].

constrained by the steady state electron current, limited by the anode.

Space Charge Limited Current

In the 90° C sample, the field at the cathode goes to zero in the steady state, as with the 40° C PE sample. This indicates space charge limited current in both these examples. At a high temperature (near glass transition), a small heterocharge distribution is observed, as with the lower temperature samples. negative charge builds up near the anode, reducing the field in the bulk. Injection of negative charge at the cathode further reduces the field at that electrode, until the field at the cathode goes nearly to zero. Further transport is limited by the motion of the internal charge, maintaining a low field at the negative electrode interface. This is described as the *space charge limit* of conduction. and is distinguished from the *contact limit* by the E-field at either electrode.

5.4 Polyethylene

The polyethylene samples tested did not exhibit a dominant heterocharge distribution as observed in PMMA. In fact, there appears to be a dominant homocharge component in all the samples tested. This is probably the result of there being no oxygen bonds which would generate a large mid-gap state density [1] as with PMMA. In the samples analyzed in this work, negative charge builds up near the cathode and the carriers tend to migrate across the sample. PE appears to eventually accumulate charge until a space charge limited current is reached [41].

A large part of the difficulty in analyzing PE is the variety of microscopic configurations in which the polymer is found. The density, amount

of cross-linking, and process used to form the material all contribute to the observed properties [45]. There is usually a large concentration of mobile ionic compounds within the material matrix due to the processing, as well as anti-oxidants to prolong the life of the material. Consequently, it is difficult to compile a consistent set of data from other authors [38] to analyze PE in the way that PMMA was analyzed.

5.4.1 Analysis of PE

The mobility at 40° C can be determined by the charge motion in Fig. 4.11. The injected charge moved in with an approximate mobility

$$\mu_{PE} \approx 1 \times 10^{-11} \frac{cm^2}{V sec}$$

filling up to a maximum concentration of less than 3×10^8 cm^{-3}. This charge concentration can be related to the density of deep traps, which is apparently much smaller than the concentration observed in PMMA. This result is also consistent with the idea that conduction in PE is dominated by band conduction and is not trap limited at higher temperatures.

5.5 Conclusions

Electrically stimulated acoustic wave measurements were used to probe the accumulated space charge in PMMA and PE. Significant concentrations of charge were found to accumulate in these materials The data was compared to the results of other researchers to provide a quantitative model of the electronic structure of PMMA. The localized motion of trapped electrons under the influence of an external electric field is observed throughout a range of temperatures from 20° C to 90° C, below the glass transition temperature.

203

A complete analysis of any polymer would have to include the effects of different metal electrodes to characterize more accurately the interface effects during oxidation and reduction under an applied field. Also, a greater range of fields should be studied to obtain a more accurate picture of the trap density across the mobility-gap.

Within the range of fields, from approximately 4 to 40 $\frac{KV}{cm}$, the conduction in PMMA may be described by a phonon assisted, thermally activated electron hopping process. This is otherwise called *polaron* conduction. The experimental results lead to a characteristic activation energy for steady state conduction of

$$W \approx 1.5 \pm 0.3 \text{ eV}$$

which is consistent with the conductivity activation energy of 1.5 eV determined by Munick [49]. From the virtual cathode measurements, an equilibrium concentration of charged traps has been estimated to be

$$2 \times 10^{10} cm^{-3}$$

This agrees with the equilibrium charge density determined from the thermally activated model proposed in section 5.2.

The maximum charge density measured occurred in the sample poled at 90° C. It aquired a peak charge concentration of approximately $\rho_{max} = 450 \frac{nC}{cm^3}$. Since the density of states near the Fermi level is approximately $10^{14} \frac{cm^{-3}}{eV}$, the shift is found

$$\Delta E_f = \frac{\rho_{max}}{qg(E_{f0})} \approx 0.025 \ eV$$

At the temperature this experiment was performed, the Fermi level shift is about 1 kT away from equilibrium. It can be concluded that the electro-

chemical potential of the material does not shift substantially from equilibrium under the moderate fields and the range of temperatures studied. Therefore, the space charge profiles result from a minor perturbation from equilibrium.

The possibility of mobile ionic carriers leading to some of the observed transport characteristics has not been considered in this study because of the evidence supporting the electron hopping model. It would be instructive to perform an impurity assay in order to determine what the concentration of mobile impurities to either refute or support the early assumption that it is negligible.

The virtual cathode experiments have demonstrated that the implanted electrons affect the composition of the polymer by altering the electronic properties. In order to study the effects of the bulk material, it is necessary to image the charge on the opposite electrode; otherwise, any decay analysis will examine the radiation modified region. It was found that the conductivity is increased by approximately 10 times in the region closest to the electron beam. This experiment also gave strong evidence that the bulk charge carrier concentration is large, and the dominant contributor to temperature dependent conductivity.

Overall, the ESAW method for analyzing insulators has been shown to be a reliable way of profiling the accumulated space charge under a variety of thermal and electrical conditions. The principle can be applied to any size scale with sufficiently designed equipment. This technique can be applied to inorganic as well as organic materials with a dielectric relaxation time that is short in comparison to the applied external voltage pulse. Under these conditions, the charge distribution can be examined and compared

with current verses time, field and temperature, optical absorption spectra and any other available data to determine a great deal about the electronic structure of an insulating material.

.

Bibliography

[1] M. Ieda, "In Pursuit of Better Electrical Insulating Solid Polymers: Present Status and Future Trends"; IEEE Transactions on Electrical Insulation, Vol. EI-21, No. 5, October 1986 pg.793

[2] D. Adler "Chemistry and Physics of Covalent Amorphous Semiconductors"; *Physical Properties of Amorphous Materials* Edited by D. Adler, B.B. Schwartz, and M.C. Steele, Plenum Publishing 1985

[3] J.J. O'dwyer *The Theory of Electrical Conduction and Breakdown in Solid Dielectrics*, Clarendon Press, Oxford 1973

[4] J. Mort and G. Pfister *Electronic Properties of Polymers*, Wiley Inter-science 1982

[5] S.B. Lang and D.K. Das-Gupta "Laser-Intensity Modulation Method: A technique for determination of spatial distributions of polarization and space charge in polymer electrets"; J. Appl. Phys., Vol. 59, No. 6, 15 March 1986 pg.2151

[6] H.J. Neuhaus and S.D. Senturia "Conduction Transients in Polyimide"; American Chemical Society Symposium Series 407: *Polymeric Materials for Electronics Packaging and Interconnection*, J.H. Lupinski and R.S. Moore, ACS Washington DC 1989 pg.176

[7] J. Lewiner "Evolution of Experimintal Techniques for the Study of the Electrical Properties of Insulating Materials"; IEEE Transactions on Electrical Insulation Vol. EI-21, No. 3, June 1986 pg.351

[8] G.M. Sessler, J.E. West, and D.A. Berkley "Determination of Spatial Distribution of Charges in Thin Dielectrics"; Physical Review Letters Vol. 38 No. 7, 14 February 1977 pg.368

[9] M. Falk, G. Dreyfus, and J. Lewiner "Vapor-induced Depolarization Currents"; Physical Review B, Vol. 25 No. 8, 15 April 1982 pg.5509

[10] R.E. Collins "Analysis of Spatial Distributions of Charges and Dipoles in Electrets by a Transient Heating Technique"; Journal of Applied Physics, Vol. 47 No. 11, November 1976 pg.4804

[11] K.P. Homewood "An Experimental Investigation of the Depth of Penetration of Charge into Insulators Contacted by a Metal"; J. Physics D: Applied Physics, Vol. 17, 1984 pg.1255

[12] P.G. Lederer, T.J. Lewis, and R. Toomer "Transport Processes in Polymeric Solids - the role of the surface and the electrodes"; Conference on Electrical Insulation and Dielectric Phenomena 1981 pg.58

[13] M.Zahn "Transient Charge Conduction in High Field Stressed Dielectrics"; Proceedings of the IEEE International Symposium on Electrical Insulation, Cambridge MA, June 1988

[14] T. Maeno, T. Takada, and Y. Nonaka "Dependence of an Applied DC Voltage on Electric Field Distribution in Insulating Oil using the Kerr-Effect Technique"; Proceedings of IEEJ Symposium on Electric Insulation Materials, Tokyo Japan, September 1988

[15] C.M. Cooke, K.A. Wright "Pulsed Electro-Acoustic Determination of Self Relaxation of MeV Energy Electron Implanted Charge in PMMA"; Proceedings of the Second International Conference on Conduction and Breakdown in Solid Dielectrics 1986 pg. 318

[16] M. Hikita, M. Zahn, K.A. Wright, C.M. Cooke, and J. Brennan "Kerr Electro-optic Field Mapping Measurements in Electron-beam Irradiated Polymethylmethacryate"; IEEE Transactions on Electrical Insulation, Vol. 23 No. 5, October 1988 pg.861

[17] C. Alquie, G. Dreyfus, and J. Lewiner "Stress-Wave Probing of Electric Field Distributions in Dielectrics"; Physical Review Letters Vol. 47, No. 20, 16 November 1981 pg.1483

[18] G.M. Sessler, J.E. West, and G. Gerhard "High-Resolution Laser-Pulse Method for Measuring Charge Distributions in Dielectrics"; Physical Review Letters Vol. 48, No. 8, 22 February 1982 pg.563

[19] R. Gerhard-Multhaupt "Analysis of Pressure-Wave Methods for the Nondestructive Determination of Spatial Charge or Field Distributions in Dielectrics"; Physical Review B, Vol. 27, No. 4, 15 February 1983 pg.2494

[20] G.M. Sessler and R. Gerhard-Multhaupt "Charge and Polarization Profiles in Polymer Electrest"; Proceedings of the fifth International Symposium on Electrets, Heidelberg 1985 pg.565

[21] T. Ditchi, C. Alquie, J. Lewiner, E. Favrie, and R. Jocteur "Electrical Properties of electrode / polyethylene / electrode structures"; IEEE Transactions on Electrical Insulation, Vol. 24 No. 3, June 1989 pg. 403

[22] F. Chapeau, C. Alquie, and J. Lewiner "The Pressure Wave Propagation Method for the Analysis of Insulating Materials: Application to LDPE Used in HV Cables"; IEEE Transactions on Electrical Insulation, Vol. EI-21 No. 3, June 1986 pg.405

[23] K. Holdik and W. Eisenmenger "Charge and Polarization Dynamics in Polymer Films"; Proceedings of the Fifth International Symposium on Electrets, Heidelberg 1985 pg.553

[24] T. Takada, T. Maeno, and H. Kushibe "An Electric Stress Pulse Technique for the Measurement of Charges in a Plastic Plate Irradiated by an Electron Beam"; Proceedings of the Fifth International Symposium on Electrets, Heidelberg 1985 pg.451

[25] T. Maeno, T. Futami, H. Kushibe, T. Takada, and C.M. Cooke "Measurement of Spatial Charge Distribution in Thick Dielectrics Using the Pulsed Electroacoustic Method"; IEEE Transactions on Electrical Insulation, Vol. 23 No. 3, June 1988 pg.433

[26] S. Pelissour, H. St-Onge, and M.R. Wertheimer "Electrical Conduction of Polyethylene Below and Above its Melting Point"; IEEE Transactions on Electrical Insulation, Vol. 23 No. 3, June 1988 pg.325

[27] G.S Kino, *Acoustic Waves: Devices, Imaging, and Analog Signal Processing*; Prentice Hall inc, NJ 1987

[28] J.H. Shapiro, Class notes for *Optical Detection and Communication - 6.453*; copyright MIT Cambridge MA 1988

[29] E. Dieulesaint and D. Royer, *Elastic Waves in Solids*; John Wiley and Sons, Paris 1980

[30] R. Barakat, "The Calculation of Integrals" from Topics in Applied Physics Vol. 41 *The Computer in Optical Research*; B.R Frieden editor, Springer-Verlag 1980

[31] H. J. Neuhaus, "Electrical Conduction in Polyimide"; Ph. D. Thesis, MIT, February 1989

[32] J.R. Melcher *Continuum Electromechanics*; MIT Press, Cambridge MA 1981

[33] H.J. Pain *The Physics of Vibrations and Waves*; J. Wiley and sons LTD, London 1983 (3rd edition)

[34] H.A. Haus and J.R. Melcher *Electromagnetic Fields and Energy*; Prentice Hall, New Jersey 1989

[35] CRC *Handbook of Chemistry and Physics* R.C. Weast editor, 58th edition 1977

[36] K. Nakamura and Y. Wada, "Piezoelectricity, Pyroelectricity, and the Electrostriction Constant of Poly(vinylidene Floride)"; Journal of Polymer Science: part A-2, vol.9 1971 pg. 161

[37] M. Oshiki and E. Fukada, "Inverse Piezoelectric Effect and Electrostrictive Effect in Polarized poly(vinylidene Floride) films"; Journal of Material Science Vol. 10 1975 pg. 1

[38] T. Ditchi, C. Alquie, J. Lewiner, E. Favrie and R. Jocteur, "Electrical Properites of Electrode/ Polyethylene/ Electrode Structures"; IEEE Transactions on Electrical Insulation Vol. 24 No. 3, June 1989 pg. 403

[39] C.M. Cooke; private consultation.

[40] C.M. Cooke, K.A. Wright, N. Takasu, J.B. Bernstein and E. Gollin, "Calibration of Volume Charge Measurements by use of Electron Beam Implantation"; Proceecings of IEEE Conference on Electrical Insulation and Dielectric Phenomena 1989 pg.435

[41] M.A. Lampert, P. Mark, *Curring Injection in Solids*, Academic Press NY, 1970

[42] T.J. Lewis, "Electrical Effects at Interfaces and Surfaces"; IEEE Transactions on Electrical Insulation Vol. 21 No. 3, June 1986 pg. 289

[43] T.J. Lewis, "Charge Transport in Polymers"; IEEE proceedings of the Conference on Electrical Insulation and Dielectric Phenomena 1976 pg. 533

[44] V. Adamec "Electrical Conductivity if Polymer Insulating Materials"; Z. angew. Physik, Bd. 29 Heft. 5 1970 pg. 291

[45] M. Ieda "Electrical Conduction and Carrier Traps in Polymeric Materials"; IEEE Transactions on Electrical Insulation Vol. EI-19 No. 3, June 1984 pg. 162

[46] V. Adamec, J.H. Calderwood, "Electrode Polarization in Polymeric Dielectrics"; IEEE Transactions on Electrical Insulation Vol. 24 No. 2, April 1989 pg. 205

[47] M.H. Cohen, H. Fritzsche, and S.R. Ovshinsky, "Simple Band Model for Amorphous Semiconducting Alloys"; Physical Review Letters Vol. 22 No. 20, 19 May 1969 pg. 1065

[48] Hans Meier, *Organic Semiconductors*; Verlag Chemie, GmbH, D-694 Weinheim 1974

[49] R.J. Munick, "Electrical Conductivity of Plexiglass"; Journal of Applied Physics Vol. 28 No. 11, November 1957 pg. 1302

[50] T.J. Fabish and C.B. Duke, "Molecular Charge States and Contact Charge Exchange in Polymers"; Journal of Applied Physics Vol. 48 No. 10, October 1977 pg. 4256

[51] R.J. Munick, "Transient Electric Currents from Plastic Insulators"; Journal of Applied Physics Vol. 27 No. 10, October 1956 pg. 1114

[52] G.A.N. Connell, "Optical Properties of Amorphous Semiconductors"; in Amorphous Semiconductors Vol. 2, M.H. Brodsky editor, Springer-Verlag NY 1985

[53] D.K. Davies, "Carrier Transport in Polythene"; Journal of Physics D, Vol. 5, 1972 pg. 162

[54] D.T. Clark and H.R. Thomas, "Applications of ESCA to Polymer Chemistry. XI. Core and Valence Energy Levels of a Series of Poly-methacrylates"; Journal of Polymer Science, Polymer Chemistry Edition, Vol. 14, 1976 pg. 1701

[55] S. Kuper and M. Stuke, "UV-Excimer-Laser Ablation of Polymethyl-methacrylate at 248 nm: Characterization of Incubation Sites with Fourier Transform IR- and UV- Spectroscopy"; Applied Physics A, Vol. A 49, 1989 pg. 211

[56] J.H. Wendorff, "Studies on the Nature of Order in Amorphous Poly-mers" from Order in the Amorphous "State" of Polymers; S.E. Keinath, R.L. Miller, and J.K. Reike editors, Plenum Press, NY 1985

[57] A. Gupta, R. Liang, F.D. Tsay and J. Moacanin, "Characterization of a Dissociative Excited State in the Solid State: Photochemistry of Poly(methyl methacrylate). Photochemical Processes in Polymeric Systems"; Macromolecules, Vol. 13, 1980 pg. 1696

[58] J.J. Ritsko, L.J. Brillson, R.W. Bigelow and T.J. Fabish, "Electron Energy Loss Spectroscopy and the Optical Properties of Polymethyl-methacrylate from 1 to 300 eV"; Journal of Chemical Physics, Vol. 69, 1 November 1978 pg. 3931

[59] V. Adamec and E. Mateova, "Electrical Conductivity of PMMA at Linearly Increasing Temperatures"; Polymers, Vol. 16, March 1975 pg. 166